TAMPEREEN TEKNILLINEN YLIOPISTO
TAMPERE UNIVERSITY OF TECHNOLOGY

Minna Sikiö

Textural Features in Medical Magnetic Resonance Image Analysis of the Brain and Thigh Muscles

Julkaisu 1418 • Publication 1418

Tampere 2016

Tampereen teknillinen yliopisto. Julkaisu 1418
Tampere University of Technology. Publication 1418

Minna Sikiö

Textural Features in Medical Magnetic Resonance Image Analysis of the Brain and Thigh Muscles

Thesis for the degree of Doctor of Science in Technology to be presented with due permission for public examination and criticism in Tietotalo Building, Auditorium TB109, at Tampere University of Technology, on the 21st of October 2016, at 12 noon.

Tampereen teknillinen yliopisto - Tampere University of Technology
Tampere 2016

ISBN 978-952-15-3816-2 (printed)
ISBN 978-952-15-3823-0 (PDF)
ISSN 1459-2045

To Janne

Minä en luota kompassiin, koska se
vain sotkee luontaisen suuntavaistoni
- Nuuskamuikkunen -

Abstract

Magnetic resonance imaging (MRI) provides high-quality images with excellent contrast detail of soft tissues and anatomic structures. MR images contain a large amount of detailed information – some of which is invisible to the human eye. Detailed information can be analysed with computer-assisted texture analysis (TA), which is based on features describing the grey level relationships between image pixels.

The aim of this thesis was to assess the information content of textural features based on the image histogram, grey level co-occurrence matrix, and grey level run-length matrix. The strengths and limitations of the various textural features in medical MR image analysis were evaluated. The study was conducted by analysing different clinical data with TA in the clinical environment, and the results of the learning process were then gathered in this thesis.

Our results indicated that all textural features have limitations in terms of their discrimination capacity in medical MR images and their dependence on the size of the region of interest and MR imaging parameters. By considering these limitations, TA may help in various MR imaging applications by revealing textural information of the images of various human organs.

Preface

"By drifting" I would answer to question of how I ended up writing this thesis. Just drifting. First, I drifted to Tampere University of Technology just because Tampere sounded a nice place to live – which later on turned out to be more than true. Second, I fell into studying Biomedical Engineering by accident because a few friends liked it, too. Third, I drifted into writing my master's thesis in Tampere University Hospital and soon I realized I was becoming a researcher in the Tissue characterisation group. Finally, I found myself doing the most interesting co-operation with other researchers, clinicians, and physicists in the field of magnetic resonance image analysis. This journey has been a memorable learning process and I have had the best opportunity to meet dozens of wonderful people during this trip. I wish to thank them all for making the road less bumpy.

The research work presented in this thesis was carried out at the Department of Radiology, Medical Imaging Center and Hospital Pharmacy, Tampere University Hospital during the years 2010-2016. The study was supported by the Pirkanmaa Regional Fund of the Finnish Cultural Science Foundation, the Finnish Foundation for Technology Promotion, the Ella and Georg Ehrnrooth Foundation, the Research Fund of the City of Tampere, the Paulo Foundation, the Finnish Parkinson Foundation, and the Competitive Research Funding of the Tampere University Hospital. I wish to thank all these organizations for enabling my research work.

There are numerous people who have made this dissertation possible. First of all, I would like to thank my thesis supervisors Professor Hannu Eskola and Docent Prasun Dastidar for their endless patience and encouragement during this process. Thank you for offering me the opportunity to work in the inspiring multi-professional environment at the hospital campus and guiding my work from the first hesitant clauses of my master's thesis to the end of this doctoral thesis process. And thank you for always finding and arranging suitable facilities for Komentokeskus girls.

I thank all co-authors of the original articles for professional help and guidance. Especially, I wish to express my sincerest thanks to hospital physicist PhLic Pertti Ryymin for all the help from the basic things such as the parameter values of the imaging sequences to throughout analyses of the manuscripts. I wish to thank Professor Jari Viik for statistical guidance and extremely helpful conversations during this study. I thank PhD Päivi Laarne for the encouragement in this process and Marjut Keskivinkka and Kirsti Mätäsniemi for the priceless help with all the practical issues. I'm also grateful to all the patients and volunteers who participated in the studies. I wish to express my gratitude to the official reviewers, Professor Riitta Parkkola and Associate Professor Simo Saarakkala, for their encouraging words and excellent commentary on this thesis.

During the work in Tampere University Hospital I have had the best opportunity to acquaint myself to the most wonderful people. Most of all, I owe my thankfulness to my dear friend and colleague PhD Kirsi Holli-Helenius for all the help, guidance, cooperation and every breakfast, lunch, snack, and ride she has offered me. This dissertation would never have happened without the other half. I wish to thank PhD Lara Harrison for her help and friendship during this process and for sharing the delight of eating bébé pastries in goretex. Also, I owe my gratitude to all colleagues at Komentokeskus, the Department of Radiology, and the Department of Oncology for sharing their time and wisdom with me.

The best counterbalance to everything thesis-related has been friends and sports, and most of all, sports with friends. I wish to thank from the bottom of my heart my soul mate Sanni Hakala, my right hand Suvi Helin, my sunshine Maria Tuominen, and all other team mates at beach volley and volleyball courts, swimming pool, and Pispala stairs for keeping me of sound mind during this process. I also owe my gratitude to family Lehtinen for all the shared moments and to my lovely godchildren Senni, Jaakko, Veeti, and Anniina for making my life so much richer. And of course Maiju, Reetta, Lapa, Sape, Katri, Reima, Suvi and all of you friends out there: I know you know how much you mean to me! Love you guys!

I also wish to thank two people without whom I would probably be somewhere very else than writing the acknowledgements of my thesis. My scientific interest was woken at secondary school by my inspiring mathematics teacher Tuula Hemilä and strengthened by Pentti Toppari at high school. Thank you for your kind motivation and all the extra assignments you made me to do.

Finally, I owe my deepest gratitude to my family. I wish to thank my mom and dad who always, always, always have believed in me and encouraged me whatever I have decided to do. I cannot thank enough my beloved husband Janne and our son, the smiling and lively Akseli, whose unwavering love and positive attitudes still amaze me every day. This thesis would never have been written without you two. Janne, thank you for being everything between technical support and personal psychologist each and every day. And Akseli, thank you for the speed and energy you bring to our lives and for every moment we laugh ourselves silly. Thank you for being you!

Tampere, August 8th

minna sikiö

Contents

Abbreviations

ACC	Average correlation coefficient
ADC	Apparent diffusion coefficient
AR	Autoregressive
COST	European cooperation in science and technology
CT	Computed tomography
DICOM	Digital imaging and communications in medicine
DTI	Diffusion tensor imaging
DWI	Diffusion-weighted imaging
EPI	Echo planar imaging
FA	Fractional anisotropy
FLAIR	Fluid-attenuated inversion recovery
FSE	Fast spin echo
GLCM	Grey level co-occurrence matrix
GLRLM	Grey level run-length matrix
GRE	Gradient echo
IR	Inversion recovery
LBP	Local binary pattern
MD	Mean diffusivity
MEDIC	Multi echo data image combination
MPRAGE	Magnetic preparation rapid gradient echo
MR	Magnetic resonance
MRF	Markov random fields
MRI	Magnetic resonance imaging
NMR	Nuclear magnetic resonance
NN	Nearest neighbour
PD	Parkinson's disease
POE	Lowest probability of error
RF	Radio frequency
ROI	Region of interest
SE	Spin echo
STIR	Short inversion recovery
SWI	Susceptibility-weighted imaging
TA	Texture analysis
TE	Echo time
TI	Inversion time
TR	Repetition time
T1	Longitudinal relaxation time
T2	Transverse relaxation time
T2*	T2* relaxation time

VOI	Volume of interest
WD	Wallerian degeneration
2D	Two-dimensional
3D	Three-dimensional

List of Original Publications

I **Sikiö, M.**, Holli-Helenius, K. K., Harrison, L., Ryymin, P., Dastidar, P., and Eskola, H., "The effect of region of interest size on textural parameters," in *IEEE Proceedings of Image and Signal Processing and Analysis*, September 7- 9, 2015, Zagreb, Croatia, 2015, pp. 149-153.

II **Sikiö, M.**, Holli, K. K., Harrison, L. C., Ruottinen, H., Rossi, M., Helminen, M. T., Ryymin, P., Paalavuo, R., Soimakallio, S., Eskola, H. J., Elovaara, I., and Dastidar, P., "Parkinson's disease: interhemispheric textural differences in MR images," *Academic Radiology*, vol. 18, no. 10, pp. 1217-1224, 2011.

III **Sikiö, M.**, Holli-Helenius, K. K., Harrison, L. C. V., Ryymin, P., Ruottinen, H., Saunamäki, T., Eskola, H.J., Elovaara, I., and Dastidar, P., "MR image texture in Parkinson's disease: a longitudinal study," *Acta Radiologica*, vol. 56, no. 1, pp. 97-104, 2015.

IV **Sikiö, M.**, Harrison, L. C., Nikander, R., Ryymin, P., Dastidar, P., Eskola, H. J., and Sievänen, H., "Influence of exercise loading on magnetic resonance image texture of thigh soft tissues," *Clinical Physiology and Functional Imaging*, vol. 34, no. 5, pp. 370-376, 2014.

V **Sikiö, M.**, Kölhi, P., Ryymin, P., Eskola, H., and Dastidar, P., "MRI texture analysis and diffusion tensor imaging in chronic right hemisphere ischemic stroke," *Journal of Neuroimaging*, vol. 25, no. 4, pp. 614-619, 2015.

The author's contribution

The author participated in study design, performed the texture analysis procedure and data analysis, and wrote all studies. Study I was conducted in co-operation with Kirsi Holli-Helenius, and Study IV was conducted in co-operation with Lara Harrison, with equal contributions from each of the authors. While writing the publications, the author received valuable comments from all co-authors.

This thesis also contains some unpublished data.

1 Introduction

Modern medical imaging has undergone major advancements. The ability to obtain information about the human body is used in diagnostics, treatment planning and follow-up. Various medical imaging images have been developed, each with its own advantages and disadvantages. Conventional X-ray, computed tomography (CT), and molecular imaging methods use ionizing radiation, whereas magnetic resonance imaging (MRI) and ultrasound imaging do not.

MRI is increasingly favoured, not only due to its advantage in avoiding the use of ionizing radiation but also due to its excellent soft tissue contrast and constantly improving imaging techniques. MRI is a sophisticated volumetric imaging method that uses a powerful magnetic field and radiofrequency pulses to produce detailed images at any imaging plane. MRI provides high-quality images with excellent contrast detail of soft tissue and anatomic structures such as grey and white matter in the brain.

Ideally, radiologists can tell the difference between healthy and diseased tissue by inspecting a clinical image. However, this is not always possible because clinical images currently contain high levels of detailed information. The human eye has a limited ability to observe these complex patterns and is occasionally unable to define them. Therefore, quantitative methods to analyse these patterns are needed. One solution is to use computer-assessed texture analysis (TA), which is based on features that describe the relationships between image pixels.

TA is already used for automatic defect detection and quality control (for example, in the food, paper, metal, textile, and plastic industries) and for automatic pattern recognition (for example, in remote sensing and mining). In studies of medical images, TA has been applied to the classification of pathological tissues based on MR images of the brain (de Oliveira et al., 2011; Fetit et al., 2015; Freeborough and Fox, 1998; Holli et al., 2010; Kassner et al., 2009; Kjaer et al., 1995; Kovalev et al., 2003; Suoranta et al., 2013), liver (Bahl et al., 2012; Yu et al., 2001; Zhang et al., 2015), breast (Ko et al., 2016; Pickles et al., 2016; Teruel et al., 2014), and lungs (Yoon et al., 2016). In addition, TA has proven able to reveal subtle changes based on MR images of bone (Harrison et al., 2011; Langenberger et al., 2003; Nikander et al., 2009) and muscle (Herlidou et al., 1999; Nakai et al., 2008; Nketiah et al., 2015). When quantified, these changes, which are invisible to the human eye, can be used in the diagnosis, treatment planning and follow-up of diseases. However, the final step that is needed to apply the TA method in everyday clinical use has not yet been taken. The TA methods used in other fields should be adapted to meet the requirements of the medical environment.

In this thesis, we evaluate the technical requirements concerning the TA of medical MR images from the brain and thigh muscles. For example, the TA parameters that are employed in industrial applications may not be the most practical for application to

medical images. The study was conducted by analysing MRI data of using TA in the clinical environment and then gathering the results of this learning process in this thesis.

The ultimate goal of TA in the clinical environment is to yield quantitative results while providing an explanation for the obtained numbers. This thesis considers the technical issues, such as size-dependence of textural features, of clinical TA with the aim of moving towards this objective.

2 Literature Review

2.1 Magnetic resonance imaging

MRI is a non-invasive tomographic imaging technique based on nuclear magnetic resonance (NMR) signals. The magnetic resonance phenomenon was discovered by Felix Bloch and Edward Purcell (Bloch, 1946; Purcell et al., 1946) in 1946. In 1975, Richard Ernst proposed techniques on which current MRI techniques are based: phase and frequency encoding, and the Fourier Transform (Kumar et al., 1975). These techniques allowed the first imaging of the human body in 1980.

MRI is based on the excitation and relaxation of spin systems, usually those in hydrogen nuclei. In the presence of an external static magnetic field, hydrogen nuclei precess around an axis in the direction of the external magnetic field and cause longitudinal magnetisation of these nuclei within the tissue. When the spins are excited to a higher energy level by the application of radio frequency (RF) pulses, the phase coherence of the spins causes transverse magnetisation to occur within the tissue. After the RF pulse is switched off, the spin system recovers to a lower energy level; i.e., it relaxes.

Already in 1971, Damadian (1971) showed that the nuclear magnetic relaxation times of tissues and tumours differed. MR image contrast is based on the fact that different tissues have different magnetic relaxation times because of their different chemical compositions and physical states. The relaxation time constant T1, termed spin-lattice relaxation, describes the recovery of the longitudinal magnetisation; the time constant T2 describes the recovery of magnetisation that is flipped into the transverse plane. Due to static magnetic field inhomogeneities, the loss of phase coherence is more rapid than T2. Therefore, this decay is described by the effective transverse relaxation time T2*. MR images are constructed by measuring these tissue-dependent NMR signals that are produced by the decay of transverse magnetisation. The signal intensity on the MR image is determined by proton density and relaxation times. The localisation of the NMR signals is selected using slice selection, phase- and frequency-encoding gradients, and spatially altered magnetic fields.

2.2 Spin echoes and gradient echoes

The timing and amplitude of RF pulses, gradient fields, and signal recording comprise an imaging sequence. One of the most conventional imaging sequences is spin echo (SE) (Farrar, 1970). Here a RF pulse, for example a pulse with flip angle of 90°, first excites the spin system and causes transversal magnetization. The transverse magnetization begins to diphase until a refocusing pulse of 180° inverts the phase of the spins producing spin echo signal at echo time (TE). The whole sequence is repeated after repetition time

(TR). The imaging parameters TE and TR may be altered to obtain the desired image contrast. In clinical practice, SE is used to acquire T1-, T2-, and proton density-weighted images. However, it is often performed as a fast spin echo (FSE) sequence where multiple echoes are recorded during one TR. The image contrast can also be modified by adding an inversion pulse of 180° prior to the initial excitation pulse. These inversion recovery (IR) pulse sequences can be used to produce images with suppression of liquid or fat. Fluid-attenuated inversion recovery (FLAIR) sequence is used to generate heavily T2-weighted images with suppression of cerebrospinal fluid whereas short inversion recovery (STIR) sequence is used heavily T1-weighted images with fat-suppression.

The echo signal can also be produced by gradient fields with different polarities. Instead of a 180° pulse, a negative gradient that destroys the phase coherence of spins is applied. The gradient is then reversed and the spins rephrase to form an echo. Gradient echo (GRE) sequences are fast because only one RF pulse with low flip angle is needed. Usually, GRE images are T2*-weighted, but modifications like magnetization preparation rapid gradient echo (MPRAGE) have been developed. The speed of the GRE sequences can be further improved with echo planar imaging (EPI) sequence which enables multislice imaging. Multi echo data image combination (MEDIC) is a heavily T2*-weighted spoiled gradient echo sequence with high signal-to-noise ratio. The sequence is based on multiple echoes that are combined into an image for less artefacts; the early echoes increase the signal-to-noise level, while later echoes boost the contrast. A fully flow compensated GRE is used to detect the susceptibility differences between tissues in susceptibility weighted imaging (SWI). SWI image contrast is highly sensitive to venous blood, haemorrhages and iron storage and is therefore often used in traumatic brain injuries and for high resolution brain venographies.

2.3 Diffusion weighted imaging

Diffusion-weighted imaging (DWI) (Merboldt et al., 1985; Taylor and Bushell, 1985) is an advanced MRI methodology that enables mapping of the diffusion of molecules in tissues. The diffusion of molecules (mainly water) is driven by thermal agitation and is highly dependent on the cellular environment; the hypothesis behind medical DWI is that changes in diffusion may indicate pathologic changes, for example an infarct inside otherwise normal appearing white matter. The image intensity in a diffusion-weighted image estimates the rate of water diffusion at that location. Quantitative DW images can be obtained using the apparent diffusion coefficient (ADC). DWI is mostly applied to the study and treatment of neurological disorders because it can reveal abnormalities in the fibre structure of white matter.

Diffusion tensor imaging (DTI) (Filler et al., 1992) is useful when the tissue has an oriented internal structure, such as the tracts in white matter. Water diffuses more rapidly in the direction aligned with the tracts and moves more slowly in the perpendicular direction. The properties of a DTI image voxel are calculated based on vector or tensor calculations, which are usually based on six or more different diffusion-weighted acquisitions, each of which is obtained with a different orientation of the diffusion-sensitising gradients. From the diffusion tensor, diffusion anisotropy measures, such as the fractional anisotropy (FA), can be computed.

2.4 Texture analysis

Textures are patterns that are present everywhere and can describe a wide variety of surface characteristics, such as those of terrains, plants, minerals, fur and human tissue. Qualitatively, texture can be described by various adjectives, such as fine, coarse, smooth, rough, regular, or irregular. Nevertheless, texture has no precise definition. TA is a computer-assessed method for the quantitative analysis of image textures. As an extension of traditional quantitative image analysis based on pixel intensity, TA addresses intensity patterns. From the TA standpoint, textures are complex visual patterns comprising spatially organised entities or sub-patterns. Image texture describes the spatial arrangement of the visual patterns in an image, i.e., the relationship between image grey levels. Thus, texture can be considered as similarity grouping in an image (Hajek et al., 2006). The aim of TA is to calculate texture features as mathematical parameters that characterise the texture type and thus the underlying structure of the objects in the image. In other words, one objective of TA can be understood as finding a way to distinguish two textures. First, this chapter covers a literature review of the used TA methods. Second, the methodology is reviewed according to the medical applications, image pre-processing steps, ROI definition, feature calculation and data analysis. A summary of TA methodology based on reviewed publications in presented in Table 2.1.

2.4.1 Methods

Several methods for TA have been proposed in the literature: structural, statistical, model-based, and transform methods (Haralick, 1979; Materka and Strzelecki, 1998; Tuceryan and Jain, 1998). According to Haralick (1979), structural models are based on the assumption that textures are constructed of primitive elements, which have geometrical properties (Allen and Mills, 2004); to describe the texture, both the primitives and the placement rules must be defined. These methods provide a good symbolic description of the image; however, this feature is more useful for texture synthesis than analysis tasks.

In contrast to structural methods, statistical approaches do not attempt to define the explicit hierarchical structure of a texture. Instead, they describe texture using properties concerning the distribution and relationships of grey level values in the image (Haralick, 1979). Local features are computed at each point of the image, and a set of statistics is derived from the distributions of the features. Statistical methods include features derived from the histogram, gradient, autocorrelation function, grey level run-length matrix (GLRLM), and grey level co-occurrence matrix (GLCM). The GLRLM was presented by Galloway (1975), and the GLCM was described by Haralick (1979). Depending on the number of pixels defining the local feature, statistical methods can be divided into first, second, and higher-order statistics. In first-order statistics, image properties depend solely on individual pixel values, whereas second-order statistics are properties of pixel pairs (Tuceryan and Jain, 1998). Methods based on second-order statistics tend to obtain higher discrimination indexes than structural or image transform methods do (Avril et al., 2001).

A combination of structural and statistical methods, local binary pattern (LBP) was introduced in the 1990's (Ojala et al., 1996; Wang and He, 1990). The LBP method has properties from both the structural (texture primitives and placement rules) and the statistical (distributions) analysis methods. The LBP method is based on the LBP feature vector that can be processed using machine learning algorithms to classify images and textures.

In model-based methods, the aim is to represent image texture using mathematical models. Model parameters are estimated and used for image analysis. For example, fractal features, Markov random field (MRF) and autoregressive (AR) models can be used. Fractals are shapes or objects that are constructed of smaller copies of themselves. It has been shown that the fractal model is useful for modelling some natural textures (Chen et al., 1989). The MRF model assumes that pixel intensity depends only on the intensities of neighbouring pixels. AR models assume that pixel intensity is a weighted sum of neighbouring pixel intensities. Texture parameters based on MRF and AR models are mostly used for image segmentation.

Transform methods derive the texture description parameters from transformations used in signal processing; for example, Fourier (Bracewell, 1999), Gabor (Qian and Chen, 1993) and wavelet (Russ, 2002) transforms. The Fourier transform is a well-known frequency transform, and the Gabor function is performed by windowing a Fourier transform. Wavelet methods are based on presenting the image as a set of independent frequency channels. Methods based on the Fourier transform function poorly in practice due to their lack of spatial localisation. The use of Gabor filters provides better spatial accuracy. However, the usefulness of these filters is limited in practice because a single filter resolution at which one can localise a spatial structure does not usually exist in natural textures. Compared to the Gabor transform, the wavelet transform has several advantages. For example, varying the spatial resolution enables texture presentation at the most suitable scale. In addition, a wide range of choices for the wavelet function is available; therefore, one is able to choose wavelets that are best suited for TA in a specific application.

The numerical analysis of image texture has been studied since the 1950s (Haralick et al., 1973). Initial applications covered the quantification of aerial images (Kaizer, 1995), but the methodology was soon extended to the medical environment. MR images contain a large amount of information not only about the external shape of large organs but also about details of the internal tissues; thus, TA is a feasible method for quantitative MR image analysis (Hajek et al., 2006; Szczypinski et al., 2007). The reason for using TA is that by examining the values of texture features, one can draw conclusions about a pathology or disease process. It is assumed that such processes cause changes in tissue structure that can be measured from the image texture (Bahl et al., 2012).

2.4.2 Examples of medical applications

TA has been used in combination with computed tomography (CT), X-ray imaging and ultrasonic tissue characterisation for the classification of various tissue types. The first publications of MR image TA in the 1990s concerned brain tumours (Kjaer et al., 1995; Lerski et al., 1993). Since then, TA has been applied in several MRI studies. For instance, structural brain asymmetry has been studied with TA by Kovalev et al. (2003) who showed male brains more asymmetric than female and asymmetry increases and decreases with age depending on the brain region. In early studies, the value of MR image texture was assessed in Alzheimer's disease (Freeborough and Fox, 1998); furthermore, using TA, it is possible to detect lesions and abnormalities involving hippocampal sclerosis (Yu et al., 2001). TA can also provide information that is useful for the diagnosis of skeletal muscle dystrophy (Herlidou et al., 1999). Currently, research regarding the TA of medical MR images is ongoing. The application methods and practices vary in terms of, for example, the pre-processing of MR images before the analyses, the study population, the ROI setting, the number of TA features calculated, and the data processing and analyses.

2.4.3 Examples of image preprocessing

Materka et al. (2000) demonstrated that some popular texture descriptors depend not only on texture but also on other properties inside the region of interest (ROI); in particular, mean intensity and variance. Thus, normalisation within the ROI is one of the recommended pre-processing steps, prior to TA feature calculation. Materka and Strzelecki (2013); Strzelecki and Materka (2014) also commented on the sensitivity of TA parameters to MR image nonuniformity and local image intensity and contrast variations. It has been shown that presence of those artefacts might result in misleading results in medical MRI TA. Therefore, nonuniformity correction has been recommended, followed by ROI normalisation, prior to texture analysis. MRI acquisition parameters have also been shown to affect texture parameter values (Mayerhoefer et al., 2009). Lerski et al. (1999) scanned reticulated foam test objects in six European centres and showed that that texture measures are not easily comparable between centres. A recent multicentre study by Fruehwald-Pallamar et al. (2016) confirmed this imaging parameter dependence while analysing benign and malignant head and neck masses. The authors concluded that TA could be used for texture discrimination when performed on one scanner using the same protocol, but no multicentre studies were recommended when using clinical data.

Variation concerning the pre-processing of medical MR images is as wide as the field of research, and conventional practices are lacking. A considerable number of studies (Fetit et al., 2015; Liu et al., 2016) apply the normalisation method described by Collewet et al. (2004), in which the image intensities are normalised in the range $[\mu \pm 3\ \sigma]$, where μ refers to the mean and σ refers to the standard deviation of the grey levels. The results of this study demonstrated the influence of the normalisation method on the effectiveness of the classification and also on the parameters selected for classification. The suggested method enhanced the differences between the two classes with the used feature selection and classifier methods (the lowest probability of error and average correlation coefficient (POE+ACC) and 1-nearest neighbour (1-NN)). However, some TA studies did not report any pre-processing of MR images and tens of studies described using multiple advanced pre-processing methods in addition to normalisation, such as motion correction (Teruel et al., 2014), intensity nonuniformity correction (Yang et al., 2015), and rescaling (Fox et al., 2016). No method has proved superior to others.

2.4.4 Examples of region of interest definition

The definition of the ROI size, shape, and localisation is an essential part of the TA process. ROIs may be drawn freehand or ROIs of standard size and shape can be applied. In addition, the localisation process can be performed manually, semi-automatically, or automatically. Overall, the ROI should represent the tissue or structure of interest with minimal overlap and distortion of other tissues or structures.

The two following ROI settings were compared by Li et al. (2015) in a study concerning the differentiation of brain metastases originating from different types of lung cancers: the standard ROI, which contained the cancer tissue and was automatically contoured on each image set using commercially available software (MIMvista, Cleveland, OH, USA) and the irregular ROI, which was manually contoured by the radiologists. In total, 126 TA features based on GLCM, gradient GLCM, Gabor transform, and intensity-size-zone were calculated. Few features were sensitive to differences in the contouring, and TA was shown to relate to the pathological type of the primary lung tumour for brain metastases. However, no texture feature was able to differentiate among the four types of lung cancer.

The limitation of ROI-based TA methods is that they require segmentation. The ROI should represent the tissue of interest without a partial volume effect, and the most accurate segmentation may be achieved when performed manually by an experienced specialist; for example, a radiologist. However, this can easily be time consuming, as in the work of de Oliveira et al. (2011), in which the corpus callosum and thalamus were studied in MR images of patients with Alzheimer's disease. A semi-automated routine for ROI segmentation was used by Teruel et al. (2014) in a study of the pre-treatment prediction of the clinical (longest tumour diameter) and pathological response (histopathological analysis of rejected tumour mass) to neoadjuvant chemotherapy in patients with locally advanced breast cancer. First, a ROI covering all areas of tissue with visible contrast enhancement that were recognised as tumour was manually drawn. Second, a relative enhancement ratio threshold was applied to exclude any voxel that did not satisfy the set requirements. Finally, an opening morphological algorithm was applied to the binary ROI to avoid the inclusion of enhanced vessels or possible spuriously enhanced voxels. The study found that various texture features significantly predicted both the clinical and pathological response. Zhang et al. (2015) used standard-size square ROIs when comparing the TA of CT and MR images for the staging of liver fibrosis. The MR images proved more accurate for staging compared to the CT images, and MRI at 3 T showed better results at classifying liver fibrosis than did MRI at 1.5 T. The issue of differently sized freehand ROIs was overcome by de Oliveira et al. (2011) by using the ROI size as the weight for all calculated TA parameters.

Maani et al. (2015) introduced a novel method that obviates the need for segmentation, as it performs the analysis on a voxel-by-voxel basis over the whole brain during the study of neurological disorders in vivo. In the proposed method, the GLCM is computed in a sphere around each voxel instead of the whole ROI. The output of the method is a statistical map that is comparable to that of voxel-based morphometry, showing differences in texture. The method was tested successfully to evaluate artificial lesions and to demonstrate cerebral changes in an MRI database relating to Alzheimer's disease.

2.4.5 Histogram-based features

Histogram features originate from the grey scale historgam of an image. The mathematical formulas and details for the presented histogram features are shown in Appendix I Hajek et al. (2006); Tuceryan and Jain (1998).

Mean measures the mean of grey level intensities in an image, and *variance* measures the wideness of the grey level distribution, i.e., the histogram of an image. *Skewness* and *kurtosis* are measures of the shape of a histogram. Skewness measures the asymmetry of the histogram, and *kurtosis* is a measure of whether the data are heavy-tailed or light-tailed relative to the normal distribution.

2.4.6 Grey level co-occurrence matrix-based features

The GLCM is a second order histogram of an image. It relates to pixel pairs, whereas first order histogram relates to single pixels. The element of the GLCM is the count of the pairs whose pixels have particular grey level values in given direction (θ) with given pixel distance (d). When divided by the total number of the pairs in the image, this histogram becomes the estimate of the joint probability of two pixels. The basics of GLCM matrix is presented in Figure 2.1. The mathematical formulas for the presented GLCM features are shown in Appendix I (Hajek et al., 2006; Tuceryan and Jain, 1998).

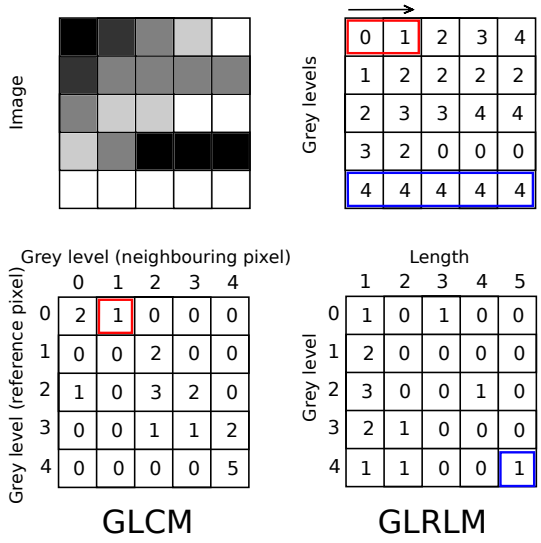

Figure 2.1: GLCM and GLRLM of an image in horizontal direction ($\theta = 0°$) with pixel distance of one pixel ($d = 1$). GLCM calculates the number of how many times a reference grey level value is followed by a specific neighbouring grey level value in the given direction. GLRLM indicates how many runs of given length the specific grey level produces.

Angular second moment, also known as uniformity or energy, is calculated as the sum of squared elements in the GLCM. *Angular second moment* is a measure of image uniformity and takes values from 0 to 1. The parameter obtains its maximum value when a grey level distribution has either a constant or a periodic form. A homogeneous image contains very few dominant grey tone transitions; therefore, the GLCM for this image type will have fewer entries of larger magnitude resulting in a large value for this feature. In contrast, the value is close to zero in a random texture.

Inverse difference moment measures the closeness of the distribution of GLCM elements to the GLCM diagonal (where the elements represent pixels that are entirely similar to their neighbours), i.e., the homogeneity of the image. This moment is maximal in a uniform image with no variation of grey levels.

Entropy measures the randomness of the elements of the GLCM and achieves its largest value when all elements in the GLCM are equal, i.e., when the image texture is complex. When the image is not texturally uniform, many GLCM elements have small values, which implies that *entropy* is large, and vice versa.

Contrast is a difference moment of the GLCM and measures the amount of local variations in an image. *Contrast* is calculated by squaring the subtraction of the examined pixel values and takes values between 0 and (maximum grey scale value - 1)^2. Thus, the minimum *contrast* value of zero is obtained when the pixels have the same grey level value, and, the maximum value is achieved when squaring the subtraction of white and black pixels.

Correlation is a measure of how correlated a pixel is with its neighbour over the whole image. This parameter measures the dependencies between the pixels in the image and takes values from -1 to 1. *Correlation* is ± 1 for perfectly positively or negatively correlated images and is close to zero for a random pattern.

Sum of squares is the variance of the GLCM. The values are not equal to but are similar to the values of the histogram variance. High values are obtained with sudden variation between neighbouring pixels.

Sum features are calculated based on the sum distribution of the GLCM. *Sum average* is calculated by summing two pixel values and averaging the result for the whole image. The pixel pairs used are those used to calculate the GLCM. Low values are obtained in low intensity regions, whereas high values are measured in high intensity grey scales. The average sum is not dependent on the direction or on the pixel distance used in the calculation. *Sum variance* is calculated based on the *sum average*, and the minimum value is achieved with a uniform image and high values with suddenly varying pixel intensities. *Sum entropy* measures the randomness of the sum distribution and also achieves its minimum value of zero in a uniform image with high values in complex patterns.

Difference variance and *difference entropy* are calculated based on the difference distribution of the GLCM. The features are zero for a uniform image and for an image with a symmetrical difference distribution around the mean value. *Difference variance* takes high values in an image with highly different neighbouring pixel intensities. *Difference entropy* takes high values in randomly distributed patterns.

2.4.7 Grey level run-length matrix-based features

The GLRLM of an image is defined as the number of runs with pixels of particalr grey level and run length. The basics of GLRLM matrix is presented in Figure 2.1. The mathematical formulas for the presented GLRLM features are shown in Appendix I (Hajek et al., 2006; Tuceryan and Jain, 1998).

Run-length nonuniformity measures the absence of equal-length grey level runs in the texture. The feature takes its lowest values in a texture with equal run-lengths; i.e., the texture is somehow repeating. More randomly distributed textures provide higher values. *Grey level nonuniformity* yields low values if grey levels are equiprobable and high values where there are no pixels of same grey level value in the direction in which the feature is calculated.

Long-run emphasis moment achieves high values for images that contain several pixels of the same grey level in a row. The maximum value is obtained in a uniform image. Small values are obtained in images with no neighbouring pixels of the same intensity. *Short-run emphasis inverse moment* achieves its maximum value of 1 when every consecutive pixel has a differing grey level value. Uniform textures return low parameter values. *Fraction* describes the percentage of image pixels that are part of the runs that are considered for the matrix calculation. If the runs are of length 1 pixel, then the percentage is 100%, and the parameter value is 1. Values close to one can be obtained in complex patterns. Small values are achieved for uniform images.

2.4.8 Examples of data analysis

The number of calculated TA features is usually affected by the post processing of the TA data. The practice varies between analyses of single feature values to multivariate analyses of hundreds of TA features or combinations of TA and other measures.

Ko et al. (2016) investigated the potential correlation between the heterogeneity obtained from TA of MR images and the heterogeneity observed from histopathological findings in invasive breast cancer. The MRI TA parameters of homogeneity and entropy were

correlated with pathological tumour heterogeneity. Based on a multivariate analysis of several texture features, Liu et al. (2016) showed that texture parameters derived from T1-, T2-, and diffusion-weighted MR images combined with supervised machine-learning algorithms could act as imaging biomarkers for the therapeutic response of nasopharyngeal carcinoma to chemo-radiotherapy. Pickles et al. (2016) associated pre-treatment MR image texture features, among other MRI-based metrics (vascular kinetics and shape and size features), to the survival intervals of breast cancer patients. Promising TA results have been obtained with several data analysis methods and textural information can be utilized also among other measures. More studies are needed to find the best data processing solution for different applications.

2.4.9 Phantom studies

Phantoms are principally used in the quality control of MRI devices. They can also be utilised for quantitatively comparing MR imaging instruments. Various MR imagers have been compared based on anatomic tissue and phantoms (Lerski et al., 1999; Mayerhoefer et al., 2005). As in many other branches of MR imaging, phantoms are used to evaluate the possibilities of using TA on MR images. As several hundred texture features are available, it would be important to find the functional features for specific applications and to understand how they can be used to classify texture.

Tissue-equivalent MRI phantoms have been developed using carrageenan (Yoshimura et al., 2003), agarose (Kraft et al., 1987; Mitchell et al., 1986), agar (Bucciolini et al., 1989; Vre et al., 1985), polyvinyl alcohol (Mano et al., 1986), and gelatin (Blechinger et al., 1988; Madsen and Fullerton, 1982). These gel phantoms usually contain additives such as paramagnetic ions to control T1 relaxation times, whereas the T2 relaxation times are primarily a function of the gelling agent concentration. Textural objects have been added to homogeneous phantoms using reticulated foams embedded in doped agarose gels (Lerski and Schad, 1998) and solutions of polystyrene spheres and agar gel (Mayerhoefer et al., 2009). Despite of several phantom studies, there is no conventional solution for TA feature standardisation, yet.

2.5 Clinical background

2.5.1 Parkinson's disease

Parkinson's disease (PD) is a progressive disorder of the central nervous system. Signs of PD include rest tremor, bradykinesia, rigidity and the loss of postural reflexes (Lees et al., 2009). Pathophysiologically, PD is characterised by a loss of dopaminergic neurons in the basal ganglia; the most seriously affected brain area is the substantia nigra (SN) pars compacta (Davie, 2008; Hornykiewicz, 1973, 1998; Obeso et al., 2008). This structure participates in controlling voluntary movements, and when information transfer is disturbed by the loss of the neurotransmitter dopamine, the consequence can be seen as symptoms of PD (Lees et al., 2009). Positron emission tomography (PET) is a nuclear imaging technique, which allows in vivo estimations of important physiological parameters such as, glucose metabolism and neuroreceptor binding enabling greater understanding of the pathophysiology of PD. However, PET imaging is not available at every clinic and utilizes ionizing radiation.

Several studies (Antonini et al., 1993; Brar et al., 2009; Dexter et al., 1991; Graham et al., 2000; Griffiths et al., 1999; Martin et al., 2008; Ryvlin et al., 1995; Vymazal et al., 1999;

Table 2.1: Summary of TA methodology and the main results from reviewed studies.

Publication	Medical application	MRI	Study population	ROI/VOI setting	Number of TA features	Image pre-processing	Data analyses	Main results
KO 2016	Breast cancer	1.5 T, T1, T2	75	2D freehand (visible tumour)	2 (GLCM)	Filtration and resampling	Statistical analyses	Disease increased uniformity and decreased entropy
LIU 2016	Nasopharyngeal carcinoma	3.0 T, T1, T2, DW	53	2D freehand (lesion)	126 (GLCM, gradient CM, Gabor transform, ISZM)	Normalisation ($\mu\pm3\sigma$), quantisation	Feature selection, classification, machine learning	Parameters from T1 showed better classification than those from T2 and DW
FETIT 2015	Childhood brain tumours	1.5 T, T1, T2	48	2D/3D semi-automatic irregular (segmented tumour), visual check	33 (histogram, gradient, GLCM, GLRLM)	Normalisation ($\mu\pm3\sigma$), quantisation	Feature selection, machine learning	Better classification results with 3D than 2D features
LI 2015	Brain metastases and lung cancers	3.0 T, T1	126	2D automatic vs. freehand	126 (GLCM, gradient CM, Gabor transform ISZM)	Grey level intensity clustering and normalisation	Feature selection, classification	TA features differentiated brain metastases originated from different type lung cancers
YANG 2015	Glioblastoma multiforme	T1, T2	82	2D manual square	976 (fractal, histogram gradient, GLRLM, LBP, GLCM)	Normalisation, rescaling	Feature selection, machine learning	Classical subtype best predicted by GLCM, neural subtype best predicted by GLRLM
PICKLES 2016	Breast cancer	3.0 T, T1	112	3D iterative semi-automatic irregular (segmented tumour)	4 (GLCM)	Histogram equalisation	Multivariate analysis	GLCM features associated with survival
FOX 2015	Breast cancer	3.0 T, T1	100	2D semi-automatic irregular (lesion)	3 (Minkowski functionals)	Local thresholding with normalisation, rescaling	Polynomial terms	Differences between triple negative breast cancer and other subtypes
WIBMER 2015	Prostate cancer	3.0 T, T1, T2, DW	147	2D freehand (lesion)	5 (GLCM)	Details not reported	Statistical analyses	GLCM features showed differences between non-cancerous and malignant prostate tissue
MAANI 2015	Alzheimer's disease, method	1.5 T, T1	30/30 + MRI dataset	3D whole brain (not ROI-based method)	8 (3D GLCM)	Normalisation, nonuniformity correction, and intensity standardisation	Statistical analyses	New method
TERUEL 2014	Breast cancer	3.0 T, T1	58	2D semi-automatic irregular (lesion)	16 (GLCM)	Motion correction	Statistical analyses	GLCM features showed prediction of both the clinical and pathological response
DE OLIVEIRA 2011	Alzheimer's disease	2.0 T, T1, T2	33/16	2D freehand irregular (thalamus and corpus callosum)	44 (averaged and weighted GLCM)	Not reported	Statistical analyses	GLCM features showed differences among the groups for corpus callosum and thalamus

ZHANG 2015	Hepatic fibrosis	1.5 T, 3.0 T, CT	218 MRI, 149 CT	2D manually placed standard square	15 (histogram, GLCM)	Pre-processing with and without Sober filter	Feature selection, multivariate analyses, classification	MRI better than CT, 3.0 T better than 1.5 T, mean grey value and entropy are the most useful features to classify liver fibrosis
FRUEHWALD-PALLAMAR 2015	Head and neck tumours, multicentre	1.5 T, 3.0 T	100	2D/3D free-hand (lesion)	(GLCM, GLRLM, gradient, ARM, WAV)	Not reported	Feature extraction, classification	TA not recommended for multicentre studies with clinical data
LERSKI 1999	Reticulated foam objects, multicentre	1.0 T, 1.5 T 6 hospitals	4 phantoms	2D manually placed circle	16 (histogram, GLCM)	Not reported	Multivariate analysis	Texture measures are not easily comparable between centres
KOVALEV 2002	Schizophrenia	1.0 T, T2, PD	21/19	3D irregular (brain parenchyma)	3 (anisotropy, curvature)	Not reported	Classification	TA is able to detect changes in sulcal tissue structure
FREE-BOROUGH 1998	Alzheimer's disease	1.5 T, T2, PD	40/24	3D semi-automatic irregular (segmented brain)	260 (GLCM)	Rescaling	Feature selection, classification	TA can classify patients and controls (91%)
YU 2001	Temporal lobe epilepsy	0.28 T, T2, PD	23/9	2D freehand (hippocampus)	200 (histogram, gradient, GLCM, GLRLM)	Not reported	Classification	TA can detect structural abnormalities on apparently normal hippocampi
HERLIDOU 1999	Skeletal muscle dystrophy	0.5 T, T1	17/14	2D freehand	59 (histogram, GLCM, gradient, GLRLM, morphology)	Not reported	Feature selection	TA discrimination was more exact than visual inspection

Wallis et al., 2008; Youdim and Riederer, 1993; Zhang et al., 2010) have shown significant iron accumulation in the SN, and according to Antonini et al. (1993), increased iron levels may also be present in the caudate nucleus. Studies concerning the iron deposition in the putamen and globus pallidus have shown conflicting results, with increased (Antonini et al., 1993; Drayer et al., 1986; Griffiths et al., 1999; Martin et al., 1998), decreased (Kosta et al., 2006; Ryvlin et al., 1995), and unchanged (Martin et al., 2008; Zhang et al., 2010) iron levels. Few changes are visible in MR images except for narrowed SN pars compacta (Graham et al., 2000; Menke et al., 2009). Lee et al. (1995) and Piccini and Brooks (2006) have proposed diffusion-weighted and heavily T2-weighted MRI experiments to reveal the brain structure changes. Quantitative analyses of MR images have shown progressive ventricular enlargement (Camicioli et al., 2011; Huang et al., 2007; Lewis et al., 2009) and shape changes in the thalami (McKeown et al., 2008). In a longitudinal MRI study by Ramirez-Ruiz et al. (2005), voxel-based morphometry analysis revealed a significant loss in grey matter volume during two years of follow-up. The usefulness of SWI in characterizing iron deposition has been evaluated and demonstrated in several studies (Rossi et al., 2010; Wu et al., 2014; Zhang et al., 2010, 2009). However, to the best of our knowledge, our studies (Sikio et al., 2011, 2015) were the first to evaluate the value of TA in MR images of PD patients.

2.5.2 Cerebral infarction

In the Western world, cerebral infarction (stroke) is a major cause of death and long-term disability. The signs and symptoms of a stroke include the inability to move or feel on one side of the body, problems understanding or speaking, feeling like the world is spinning, or a loss of vision on one side (Donnan et al., 2008). There are two main types of stroke: ischemic, due to lack of blood flow, and haemorrhagic, due to bleeding. CT imaging is widely used to diagnose stroke because CT scans are sensitive in detecting mass lesions and acute haemorrhage. CT is also the first examination in Finnish hospitals because haemorrhage can be excluded and thrombolytic therapy can be started based on it.

In hemispheric infarction, degenerative changes often occur in the corticospinal tracts and are deciphered as Wallerian degeneration (WD) (Waller, 1850). According to Waller (1850) and Kuhn et al. (1989), WD is characterised by the anterograde degeneration of axons due to injury of the proximal portion of the axon or its cell body. WD can be detected using conventional MRI within 1 month after the infarction; however, Thomalla et al. (2004) showed that DTI can reveal WD within the first two weeks after the infarction. ADC has been shown to decrease at the lesion site in acute ischemic stroke. This decline is followed by pseudo normalisation and, at the chronic stage, the values increase above normal levels (Ahlhelm et al., 2002).

Kovalev et al. (2001) and Herlidou-Meme et al. (2003) showed that cerebral tissues can be classified using TA. In addition, Kassner et al. (2009) studied acute ischemic stroke and concluded that TA is able to detect significant differences between infarcts that are vulnerable to haemorrhagic transformation and those that are not.

2.5.3 Tissue adaptation to exercise

Adaptation to exercise training can affect muscle volume, strength and architecture; muscle-fat distribution; and bone marrow adiposity (Baar et al., 2006; Blazevich et al., 2003). These changes depend on the exercise type, especially the forces and load patterns, the specific exercise induces. In response to exercise training, cross-sectional area and

the strength production of actively involved muscles increase because the number and cross-sectional area of the individual muscle fibres also increase until the muscle strength is adjusted to cope with the forces and loads the given muscles and bone are subjected to (Nakai et al., 2008). Conversely, less-frequent and intense exercise training is associated with smaller muscle (Bousquet-Santos et al., 2006; Browning et al., 2007; Haddad and Adams, 2006). Conventionally, the assessment of muscle adaptation to exercise has been evaluated with muscle volume. However, volume measurement does not reveal structural variation in muscle tissue or changes in intramuscular fat content. These changes may be observed with TA.

Textures have been utilized in both ex vivo and in vivo MR studies of skeletal muscles. Nakai et al. (2008) showed that walking exercise thickens and tightens the muscular fibre tissues. Mahmoud-Ghoneim et al. (2006) found TA a reproducible and non-destructive method for rat muscle examination during atrophy and regeneration. In addition, their investigation of fat structure revealed that MRI texture of subcutaneous adipose tissue differs between men and women (Mahmoud-Ghoneim et al., 2001). TA has also been proved to provide useful information contributing the diagnosis of skeletal muscle disease by Herlidou et al. (1999). TA of bone structure has been shown to give additional information to routinely measured bone density. Langenberger et al. (2003) were able to distinguish osteoporotic and nonosteoporotic subjects by means of TA. In athlete studies, high-impact and odd-impact exercise loading were associated with thicker cortex around the femoral neck (Nikander et al., 2009); and different trabecular bone (Harrison et al., 2011) and hip muscle (Nketiah et al., 2015) texture compared with non-athletes. Depending of the sports, fat tissue thickness and volume can clearly vary between athlete groups. Also, it was shown that bone marrow density is modulated by exercise loading (Rantalainen et al., 2013).

3 Aim of the Study

The aim of this thesis was to analyse textural features based on the histogram, grey level co-occurrence matrix, and grey level run-length matrix applied in medical MR images. More specific aims were to

1) Indicate of the functionality and limitations of features

2) Evaluate of the robustness of the single features in revealing subtle changes in Parkinson's disease, stroke, and healthy adult brains and thigh muscles adapted to different exercise.

4 Material and Methods

4.1 Study populations

4.1.1 Healthy adults and artificial noise images

The database comprised brain MR images of 64 healthy adults (age range, 20-60; mean age, 39.0 ± 11.7 years; 27 males, 37 females) (Study I). Exclusion criteria were neurological problems (including abnormalities on neuroimaging), psychiatric problems, history of traumatic brain injury, former neurosurgical procedure, problems with hearing or vision, first language other than Finnish, and MRI contraindications. None of the subjects had significant structural abnormalities on conventional MRI sequences. All participants gave their written consent for the study, which was conducted at Tampere University Hospital, and the study was approved by the Hospital Ethics Committee.

An artificial noise image matrix was generated using Matlab (MathWorks, Natick, MA, USA) and filled with random pixel intensity values from 0 to 255. The pixel size was set to match that of the MR images of the healthy controls (Study I).

4.1.2 Parkinson's disease

At baseline, 51 patients (age range, 40-86; mean age, 68.8 ± 11.3 years; 25 males, 26 females) with two or more of the following symptoms of PD were included in the study (Study II): resting tremor, bradykinesia or hypokinesia, rigidity or postural instability. The exclusion criteria were Alzheimer's disease or other dementia diagnosed during one year preceding the study, several general illnesses such as cardiac, lung or gastrointestinal disease, liver or kidney malfunction, active malignant neoplasm, neurological or psychiatric disease, contraindications for MRI, alcohol or drug addiction and gravidity. The control group comprised 20 healthy volunteers (age range, 58-80; mean age, 65.7 ± 6.8 years; 4 males, 16 females).

Among the patients with diagnosed PD, 26 (age range, 42-85; mean age, 68.1 ± 10.4 years; 13 males, 13 females) were selected for the longitudinal study (Study III). The control group comprised 19 healthy volunteers (age range, 58-80; mean age 65.0 years ± 6.1 years; 4 males, 15 females) with similar exclusion criteria to the patient groups and was matched by years of education. All participants gave their written consent for the study, which was conducted at Tampere University Hospital and was approved by the Hospital Ethics Committee.

4.1.3 Thigh soft tissues

The study group comprised 90 female athletes competing at the national or international level and 20 nonathletic clinically healthy female referents (Study IV). The athletes were triple-jumpers (N=9), high-jumpers (N=10), soccer-players (N=10), squash-players (N=8), power-lifters (N=17), endurance runners (N=18), and swimmers (N=18). The athletes were recruited through national sports associations and local sport clubs, and the referents were mainly students of the local University of Applied Sciences. The study was conducted at Tampere University Hospital in concert with the UKK Institute, Tampere, Finland.

4.1.4 Cerebral infarction

In total, 1,458 stroke patients were examined and treated at Tampere University Hospital between July 2005 and April 2008. For the TA study (Study V), 30 patients (age range, 46-79; mean age, 65.5 ± 8.9 years; 24 men, 6 women) were selected. The selected patients had suffered their first ever infarction located on the right hemisphere, and they had been capable of living independently before the infarction. Exclusion criteria were cerebral haemorrhage, traumatic brain injury, previous neurological or psychiatric disorder, substance abuse, lesions in the left hemisphere or previous lesions in the right hemisphere found in acute CT, remarkable brain atrophy considering patient age, severe hearing or primary visual impairment, major decline in consciousness, left-handedness, native language other than Finnish, and age over 80 years. Seven of the selected patients had received thrombolytic therapy.

4.2 Magnetic resonance imaging

4.2.1 Healthy adults

MR imaging was performed using a 3-T device (Siemens TrioTim, Erlangen, Germany) equipped with a 12-channel head matrix coil. The sequence used in our study was axial T2-weighted 2D turbo spin echo (TSE); the imaging parameters are presented in Table 4.1.

4.2.2 Parkinson's disease

Imaging was performed using a 3-T MRI device (Siemens TrioTim, Erlangen, Germany) equipped with a 12-channel head matrix coil following a clinical procedure. Sequences included in the procedure were axial T2-weighted 3D sampling perfection with application-optimised contrasts using different flip angle evolution (SPACE), axial 3D T2-weighted fluid-attenuated inversion recovery SPACE, axial 3D SWI sequence, axial 2D parametric T2* (MapIt), axial diffusion-weighted 2D EPI, axial T1-weighted 2D SE, and sagittal T1-weighted 3D MPRAGE. The baseline study of the patients and controls was performed using SWI and SPACE images; the follow-up study with SPACE images (Table 4.1). Baseline and follow-up MRI were performed with a time delay of 25.0 ± 1.5 months.

4.2.3 Thigh soft tissues

Imaging was performed using a 1.5-T MRI system (Siemens Magnetom, Avanto, Siemens Healthcare Sector, Erlangen, Germany). The thigh region of the dominant side was imaged using a combination of two 6-channel body matrix coils and a spine matrix coil.

Table 4.1: Typical acquisition parameters for the MRI sequences used in Studies I-V and an additional phantom study.

Study	Field strength (T)	Sequence name	TR (ms)	TE (ms)	TI (ms)	Slice/gap (mm/mm)	Pixel spacing (mm/mm)	Flip angle (°)
I	3	T2 2D TSE	5,790	190	-	4.0/1.2	0.49/0.49	120
II	3	3D SWI	27	20	-	1.5/0	0.60/0.60	15
II, III	3	T2 3D SPACE	3,200	354	-	3.0/0	0.60/0.60	120
IV	1.5	T2* MEDIC	40	17	-	3.0/0	0.81/0.81	12
V	1.5	T2 2D FLAIR	8,500	100	2,500	5.0/1.5	0.45/0.45	150
V	1.5	DW 2D EPI	3,500	96	-	5.0/1.5	1.80/1.80	9
Phantoms	3	T1 3D MPR	1,900	2.41	900	0.90/0	0.47/0.47	9
Phantoms	3	T1 2D SE	600	6.8	-	4.0/1.2	0.70/0.70	90
Phantoms	3	T2 3D SPACE	3,200	357	-	3.0/0	0.28/0.28	120
Phantoms	3	T2 3D FLAIR	6,000	394	2,100	3.0/0	0.47/0.47	120
Phantoms	3	3D SWI	27	20	-	1.50/0	0.94/0.94	15

The imaging sequence used in this study was an axial 3D T2*-weighted MEDIC sequence; the acquisition parameters are shown in Table 4.1.

4.2.4 Cerebral infarction

The patients underwent MRI studies in the chronic phase approximately one and a half years (mean 18.3 ± 5.5 months) after infarction. MRI was performed in normal clinical practice using a 1.5-T MRI scanner (Magnetom Avanto SQ, Siemens Medical Solutions, Erlangen, Germany) equipped with a conventional 12-channel head matrix coil. The conventional MRI protocol included sagittal 2D T1-weighted SE, sagittal 3D T2-weighted SPACE, axial T2-weighted FLAIR, axial T1-weighted SE, and axial T2-weighted GRE (T2*) sequences. DTI was performed using a single-shot diffusion-weighted EPI, and diffusion-sensitive gradients were applied along 12 gradient directions. Acquisitions were repeated 3 times, and the average result was used in the analyses. In the TA study, we used images from axial T2-weighted FLAIR and diffusion-weighted EPI series with a b-value of 1,000 s/mm^2. Typical acquisition parameters for the used sequences are presented in Table 4.1.

4.3 Image preprocessing

In all studies, the grey level normalisation of each ROI was performed using a method that normalises image intensities in the range $[\mu - 3\sigma, \mu + 3\sigma]$ (μ is the mean grey level value and σ is the standard deviation) to minimise the effects of contrast variation and brightness (Collewet et al., 2004). Eight bits per pixel were used to calculate second-order feature values; that is, the number of grey level values was 256.

4.4 Regions of interest

All studies contained selections of interesting image slices from the MR image stacks. DICOM (Digital imaging and communications in medicine) format images were manually selected using Osiris version 4.19 (The Digital Imaging Unit of the Service for Medical Computing of the University Hospitals of Geneva, Switzerland) by an operator supervised

by an experienced radiologist. ROI placement was performed using the TA software MaZda package version 4.6 (The Technical University of Lodz, Institute of Electronics, Lodz, Poland) (Strzelecki et al., 2013; Szczypinski et al., 2007, 2009).

4.4.1 Healthy adults

Axial slices representing the centrum semiovale area of each participant were selected. This location was selected because it presents clear anatomical landmarks and a relatively wide texturally homogeneous area. First, ten circular ROIs (5, 6, 7, 8, 9, 10, 15, 20, 25, 30, and 35 pixels in diameter) were manually located on the right hemisphere centrum semiovale in the selected MR slices. The ROI sizes correspond to ROI areas of from 21 to 933 pixels. The same ROI sets were randomly placed in the artificial noise image.

4.4.2 Parkinson's disease

For texture analysis, seven axial slices from every patient and healthy control were selected. Image levels were chosen to represent regions of the brain that are clinically significant in PD. Fixed-size circular ROIs were manually placed on images of both hemispheres by an operator under the supervision of an experienced radiologist. In the baseline study, we evaluated the following areas: dentate nucleus, basilar pons, SN pars reticulata, SN pars compacta, red nucleus, globus pallidus, putamen, anterior and posterior thalamus, caudate nucleus, anterior and posterior corona radiata, and anterior, medial, and posterior centrum semiovale on both hemispheres. In the follow-up study, we analysed the dentate nucleus, basilar pons, SN pars compacta, red nucleus, globus pallidus, putamen, anterior and posterior thalamus, caudate nucleus, anterior and posterior corona radiata, and anterior, medial, and posterior centrum semiovale.

4.4.3 Thigh soft tissues

The tissues were analysed at two anatomical levels of thigh that were chosen according to anatomical landmarks related to the muscles. The proximal level was the image slice just distal from the trochanter minor, and the distal level was the image slice at the insertion of the gluteus maximus muscle into the femur. The analysed tissues were thigh muscles that are actively involved in load-bearing during different exercises, subcutaneous fat, and the femoral bone marrow of the dominant leg. The muscles comprised major anterior compartment muscles such as the rectus femoris, vastus lateralis, and vastus intermedius; and medial compartment muscles such as the adductor longus and adductor magnus. Fixed-size square ROIs were placed on the central area of the muscle cross section to avoid a partial volume effect on ROIs caused by contamination with the connective tissue around the muscle and visible fascicles. In addition, a similar ROI box was placed on subcutaneous fat tissue surrounding the thigh muscles, and a spherical ROI was set on the bone marrow inside the femur.

4.4.4 Cerebral infarction

Three axial slices representing vulnerable white matter tract areas and one slice from the infarction area were selected for the analyses based on the diffusion- and the T2-weighted series. Fixed-size circular ROIss were manually placed on axial slices in the cerebral peduncle, thalamus, knee of the internal capsule, and centrum semiovale on both hemispheres. One set of ROIs was placed in the infarction area on the right and in the

corresponding areas on the left hemisphere. The ROIs were centred in the target areas, avoiding border areas and neighbouring tracts.

4.5 Texture and data analyses

Image textures were analysed using the MaZda software, and the data were statistically analysed using SPSS for Windows version 14.0.2 (Study II) and version 20.0 (Studies I, III, IV, and V) (SPSS Inc., IBM, IL, USA).

4.5.1 Healthy adults

In Study I, all histogram-, GLCM-, and GLRLM-based features were calculated for each ROI. The GLCM features were calculated using the distance of one pixel, and GLCM and GLRLM features were calculated in four directions ($\theta = 0°, 45°, 90°$, and $135°$). The four directional components of each feature were averaged into one parameter to enhance the robustness of the method because the exact position of the participants during the MR imaging could not be ensured. The same calculations were performed for the phantom images. The distributions of TA features obtained from MR and random images were analysed using scatter plots, which were constructed separately for each feature.

4.5.2 Parkinson's disease

In the baseline study (Study II), all 11 GLCM-based features were considered. The pixel distances $d = 1, 2, 3, 4$, and 5 and the directions $\theta = 0°, 45°, 90°$, and $135°$ were considered; the parameters calculated in the horizontal ($0°$) and vertical ($90°$) directions were treated as one group, and the parameters calculated in the diagonal directions ($45°$ and $135°$) were treated as another group to examine to direction-dependency of the features. Differences in texture parameters between the hemispheres in all structures were analysed using the Mann-Whitney U test.

In the follow-up study (Study III), we selected the GLCM method with two homogeneity (*angular second moment* and *inverse difference moment*) and two complexity (*entropy* and *difference entropy*) features. The features calculated using a pixel distance of one pixel were considered, and the mean value of the four directional parameters was used in further analyses. The Mann-Whitney U test was used to evaluate whether the differences between the brain MR image textures of the baseline PD patients and those of the healthy controls were statistically significant. Changes in brain structure textures between the baseline and follow-up patient images were studied using the Wilcoxon signed rank test. In addition, correlations between changes in clinical scores and MR image textures were evaluated using Pearson's correlation coefficient.

4.5.3 Thigh soft tissues

In Study IV, four GLCM-based features (*angular second moment*, *inverse difference moment*, *entropy*, and *difference entropy*) were calculated for each ROI. All features were calculated in the horizontal ($0°$), vertical ($90°$), and two diagonal ($45°$ and $135°$) directions using a pixel distance of one pixel. The direction dependency of the features was removed by calculating the mean value of the four directions. The group analyses of muscles, fat, and bone marrow were performed using the Mann-Whitney test.

4.5.4 Cerebral infarction

In Study V, four GLCM-based features (*angular second moment*, *inverse difference moment*, *entropy*, and *difference entropy*) were used in the analyses. The features were calculated in the horizontal (0°), vertical (90°), and two diagonal (45° and 135°) directions using a pixel distance of one pixel. The mean values of the four directions were used in the analyses. The mean diffusivity (MD) and FA values were calculated pixel-by-pixel based on the diffusion-weighted images. Differences between the infarcted and unaffected hemisphere were analysed using the paired t-test, and correlations were calculated using Pearson's R test.

4.6 Additional materials and methods

In addition to the published results, this thesis contains unpublished material about MRI phantoms and ROI definition in the TA procedure. The unpublished analyses were used to strengthen the published results concerning the methodology of medical MR image TA.

4.6.1 Magnetic resonance imaging phantoms

Homogeneous MRI phantoms were developed for research purposes at the Department of Biomedical Engineering at Tampere University of Technology. The phantoms were manufactured according to earlier paper by Yoshimura et al. (2003). The materials used for the phantoms were agarose (Sigma-Aldrich Finland Oy, Finland), carrageenan (Sigma-Aldrich Finland Oy, Finland), gadolinium (III) chloride ($GdCl_3$; Sigma-Aldrich Finland Oy, Finland), sodium azide (NaN_3; Tamro Medlab Oy, Finland), and distilled water. Six phantoms with differing T2 and T1 relaxation times were produced using 7-80 μmol/kg of $GdCl_3$, 0.2-1.2 % of agarose, and 3 % (fixed) of carrageenan. In addition, 0.03 % of NaN_3 was added as an antiseptic. Detailed information regarding the phantom contents is shown in Table 4.2.

The ingredients were mixed, and water was added to bring the total weight up to 100 g. The mixture was heated in a water bath at 90° and stirred with a magnetic stirrer (Ikamag, German) to dissolve the agarose. The mixture was then cooled to room temperature in a plastic container to solidify it.

The phantoms were imaged using a 3-T device (Siemens TrioTim, Erlangen, Germany) equipped with a body coil. The sequences used in our study are presented in Table 4.1, and an example image from the T2-weighted SPACE series is presented in Figure 4.1.

MR images performed with different sequences and with different pixel spacing were downscaled using Osiris to match the resolution of the largest pixel spacing (0.94/0.94

Table 4.2: Composition of the MRI phantoms.

Phantom	Agarose (g)	$GdCl_3$ (mg)	Carrageenan (g)	NaN_3 (g)	Water bath (°/min)
1	1.200	2.18	2.998	-	96/6
2	0.599	0.18	3.000	0.030	93/7
3	.201	0.20	3.000	0.031	96/7
4	0.596	0.52	2.999	0.031	95/7
5	0.200	0.52	3.000	0.031	95/7
6	1.200	2.11	2.999	0.030	95/11

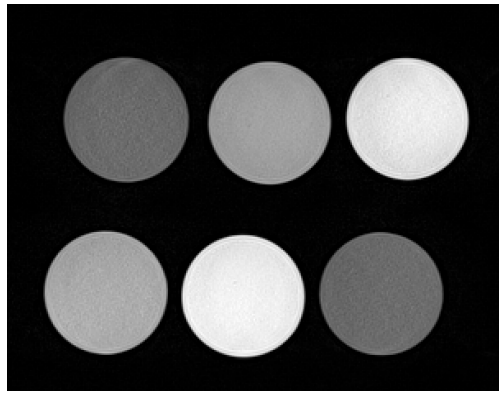

Figure 4.1: MRI phantoms imaged using the T2-weighted SPACE sequence.

in SWI). Five of each circular ROI (5, 6, 7, 8, 9, 10, 15, 20, 25, 30, and 35 pixels in diameter) were then manually located in the phantoms. Histograms and averaged GLCM and GLRLM features were calculated and analysed together with the results obtained from Study I.

4.6.2 Intra- and inter-observer variability

Intra- and inter-observer analyses concerning the ROI definition were performed for the data obtained in Study I. Standard circular ROIs of 15 pixels in diameter and freehand ROIs were manually placed and drawn on the centrum semiovale area in MR images of 64 healthy controls. Operator #1 performed the ROI definition twice at a two-week interval, and Operator #2 performed the ROI definition once. The feature distribution was analysed with box plots and statistically with Mann-Whitney U test. The ROIs are specified in Figure 4.2.

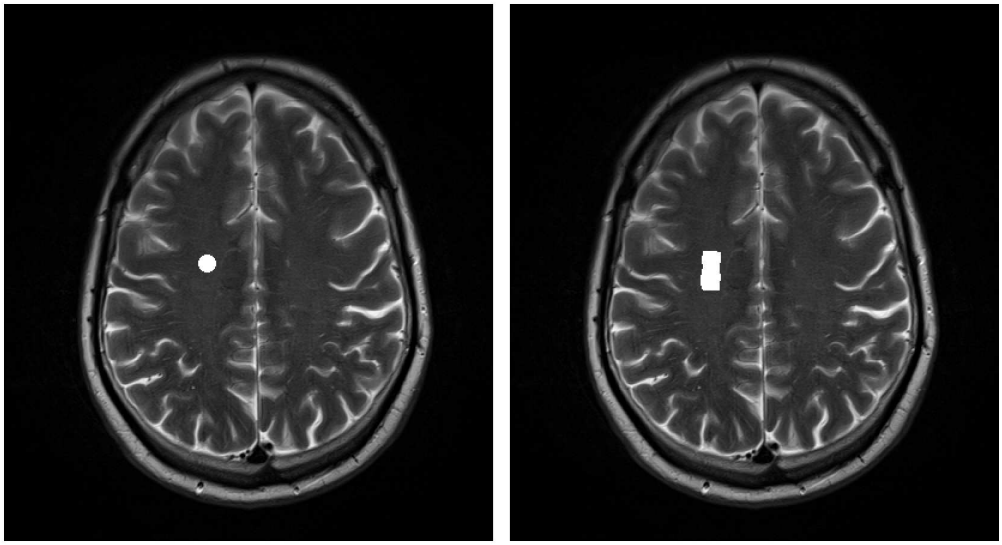

Figure 4.2: ROIs for intra- and inter-observer analyses. Left: a standard circular ROI of 15 × 15 pixels in diameter in the area of the centrum semiovale. Right: a freehand ROI at the same area.

5 Results

5.1 Information regarding textural features based on MR images of healthy controls and phantoms

The effect of ROI size on texture features was assessed in Study I. In addition, the information regarding texture features was evaluated with the following textures: the centrum semiovale from T2-weighted TSE images of healthy adults (Study I), an artificial noise image comprising a random distribution of 256 grey levels (Study I), an homogeneous agarose gel MRI phantom (T2-weighted SPACE images), and air from the TSE series of healthy adults (Study I). The texture feature values of the MRI phantom imaged with five different imaging sequences are also presented to evaluate the information content of the features in MRI TA. Moreover, the intra- and inter-observer variabilities in brain MRI scans with standard-size and freehand ROIs for each feature were evaluated.

Figures representing all three analyses for each histogram-, GLCM,-, and GLRLM-based feature are presented in Figures 5.1-5.10. The images in the top row show the feature values for the following textures as scatter plots: the centrum semiovale of healthy adults (controls), artificial noise (random), an homogeneous MRI phantom (phantom), and air (background). The images in the middle row show the feature values for the homogeneous MRI phantom imaged with the following five imaging sequences: susceptibility-weighted imaging (swi), T1-weighted MPRAGE (t1mpr), T1-weighted spin echo (t1se), T2-weighted SPACE (t2spc), and T2-weighted FLAIR (t2spcdf). The images in the bottom row show box-plots for feature values obtained from standard-size circular ROIs and freehand ROIs placed on the centrum semiovale on MR images of healthy controls (Study I) by Operator #1 (twice with two-week interval, grey plots) and Operator #2 (once, white plots).

The top row images are summarised in Table 5.1 where the mean and standard deviation values for all presented textures are presented; the middle row images are summarised in Table 5.2 where the mean and standard deviation values for phantom textures based on different sequences are presented; and the bottom row images are summarised in Table 5.3 where p-values based on Mann-Whitney U test for intra- ans inter-observer analyses are presented. A summary of all analyses concerning the behaviour of TA features is presented in Table 5.4.

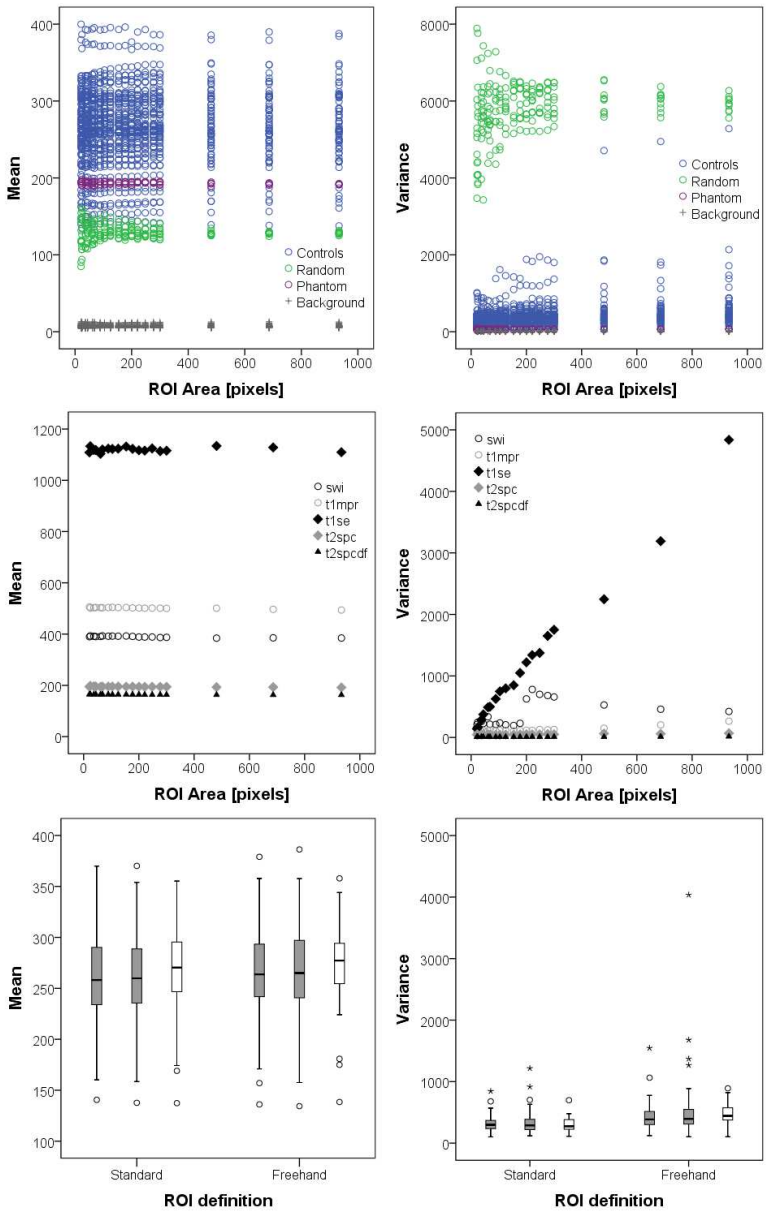

Figure 5.1: Scatter and box plots illustrating the information content and robustness of histogram *mean* and *variance*. **Top**: Feature values for the following textures using different ROI sizes: brain (controls – blue), artificial noise image (random – green), homogeneous MRI phantom (phantom – purple), and air (background – grey). **Middle**: Feature values for the homogeneous MRI phantom imaged with the following five imaging sequences: susceptibility-weighted imaging (swi), T1-weighted MPRAGE (t1mpr), T1-weighted spin echo (t1se), T2-weighted SPACE (t2spc), and T2-weighted FLAIR (t2spcdf). **Bottom**: Intra- and inter-observer variation for two ROI types: standard-size circular ROIs and freehand ROIs placed on the centrum semiovale. Operator #1 performed the ROI definition twice (grey box plots), and Operator #2 performed the ROI definition once (white box plots).

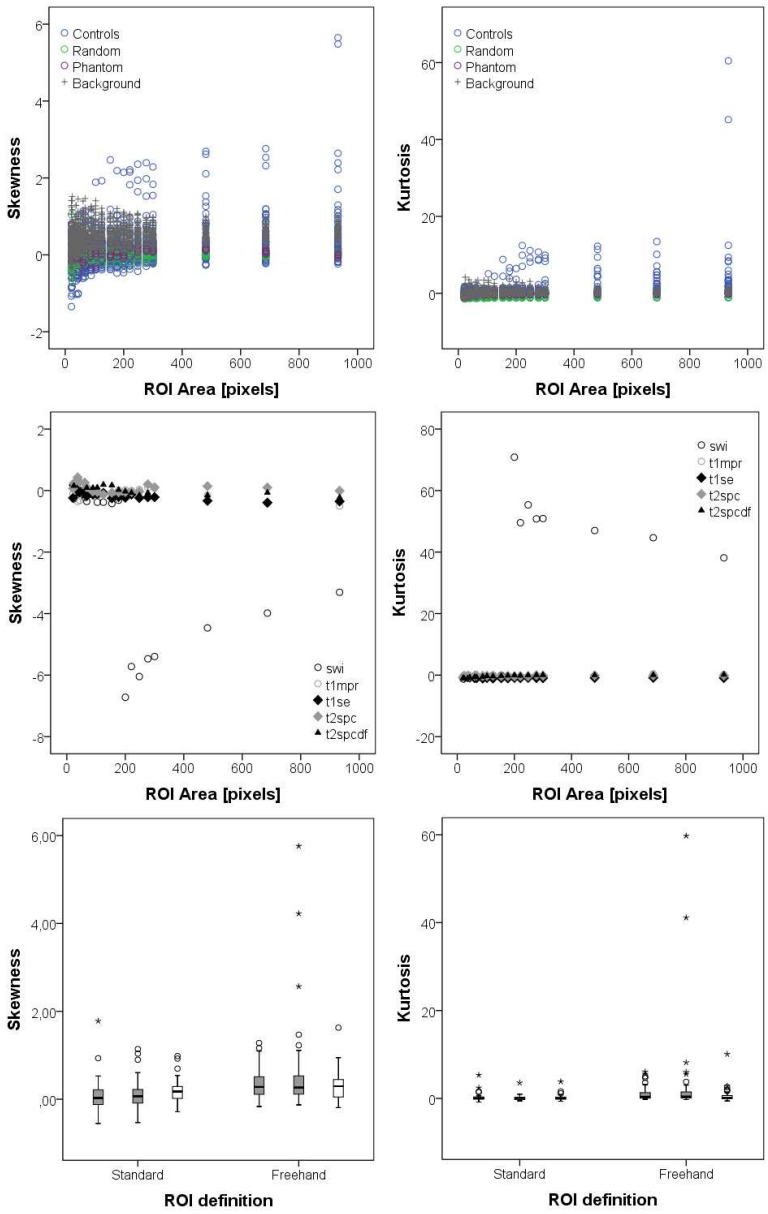

Figure 5.2: Scatter and box plots illustrating the information content and robustness of histogram *skewness* and *kurtosis*. **Top**: Feature values for the following textures using different ROI sizes: brain (controls – blue), artificial noise image (random – green), homogeneous MRI phantom (phantom – purple), and air (background – grey). **Middle**: Feature values for the homogeneous MRI phantom imaged with the following five imaging sequences: susceptibility-weighted imaging (swi), T1-weighted MPRAGE (t1mpr), T1-weighted spin echo (t1se), T2-weighted SPACE (t2spc), and T2-weighted FLAIR (t2spcdf). **Bottom**: Intra- and inter-observer variation for two ROI types: standard-size circular ROIs and freehand ROIs placed on the centrum semiovale. Operator #1 performed the ROI definition twice (grey box plots), and Operator #2 performed the ROI definition once (white box plots).

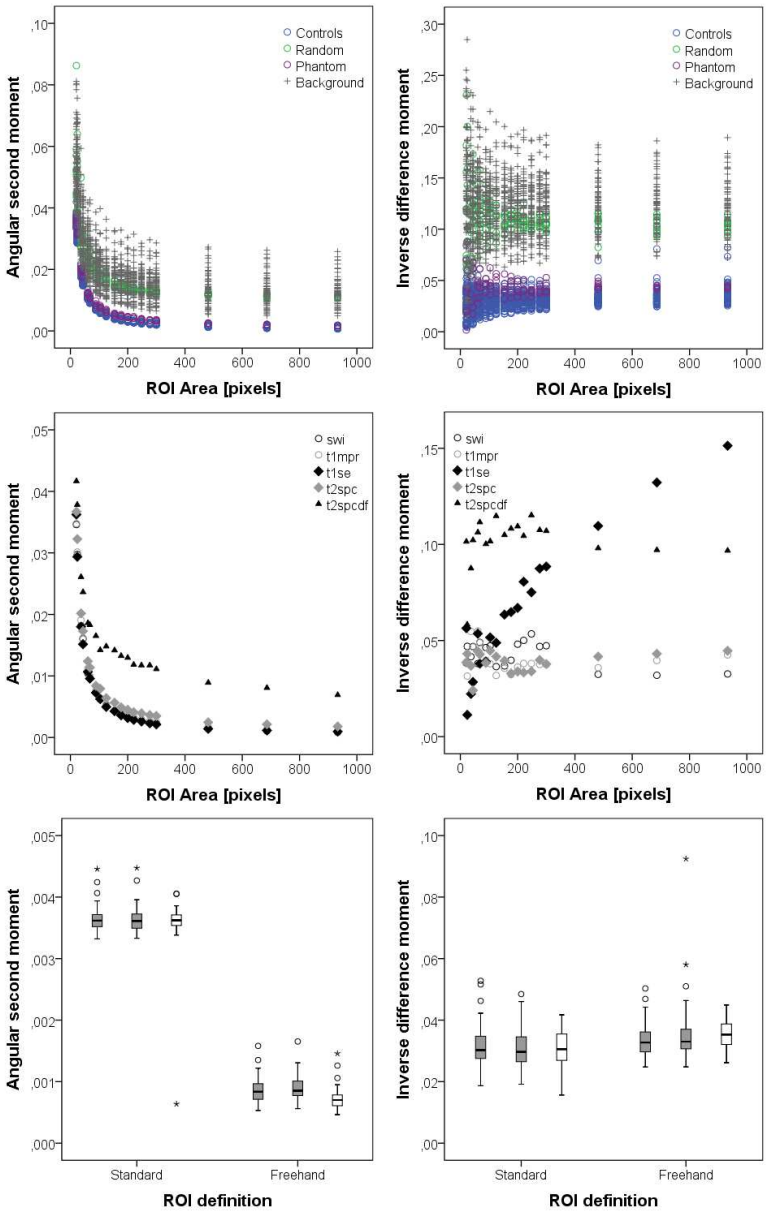

Figure 5.3: Scatter and box plots illustrating the information content and robustness of GLCM *angular second moment* and *inverse difference moment*. **Top**: Feature values for the following textures using different ROI sizes: brain (controls – blue), artificial noise image (random – green), homogeneous MRI phantom (phantom – purple), and air (background – grey). **Middle**: Feature values for the homogeneous MRI phantom imaged with the following five imaging sequences: susceptibility-weighted imaging (swi), T1-weighted MPRAGE (t1mpr), T1-weighted spin echo (t1se), T2-weighted SPACE (t2spc), and T2-weighted FLAIR (t2spcdf). **Bottom**: Intra- and inter-observer variation for two ROI types: standard-size circular ROIs and freehand ROIs placed on the centrum semiovale. Operator #1 performed the ROI definition twice (grey box plots), and Operator #2 performed the ROI definition once (white box plots).

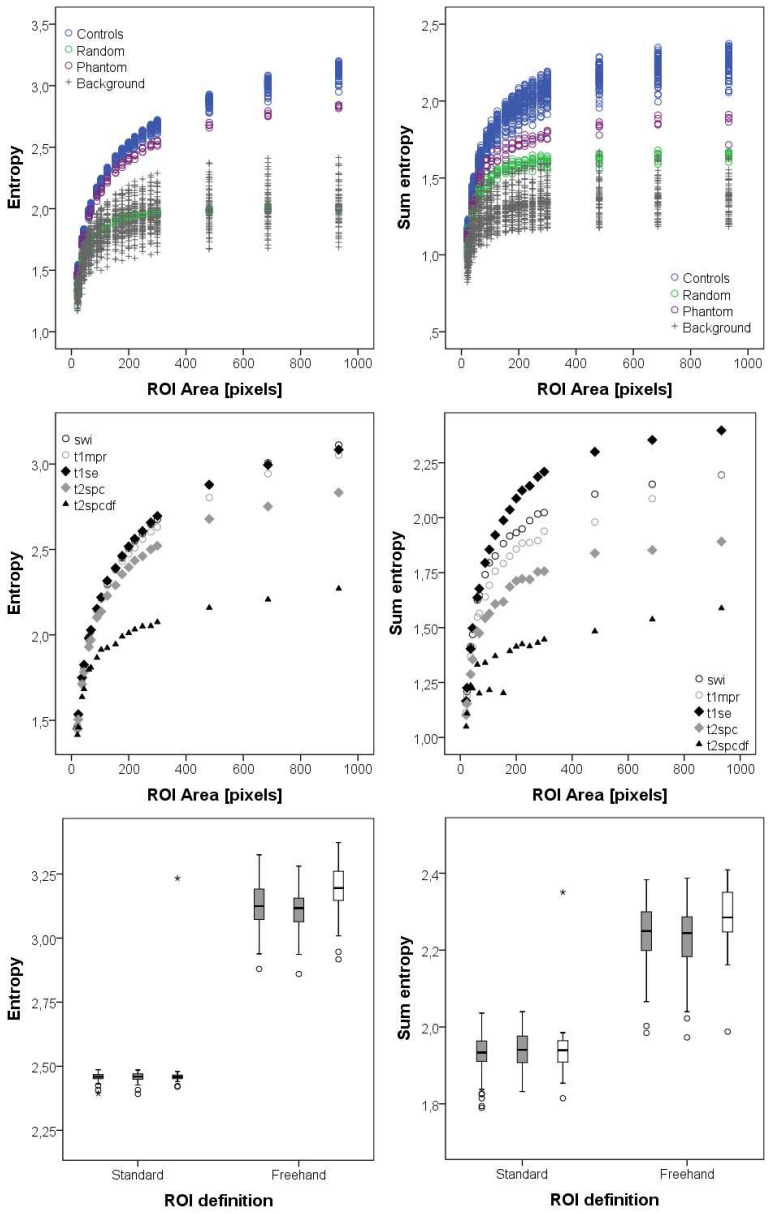

Figure 5.4: Scatter and box plots illustrating the information content and robustness of GLCM *entropy* and *sum entropy*. **Top**: Feature values for the following textures using different ROI sizes: brain (controls – blue), artificial noise image (random – green), homogeneous MRI phantom (phantom – purple), and air (background – grey). **Middle**: Feature values for the homogeneous MRI phantom imaged with the following five imaging sequences: susceptibility-weighted imaging (swi), T1-weighted MPRAGE (t1mpr), T1-weighted spin echo (t1se), T2-weighted SPACE (t2spc), and T2-weighted FLAIR (t2spcdf). **Bottom**: Intra- and inter-observer variation for two ROI types: standard-size circular ROIs and freehand ROIs placed on the centrum semiovale. Operator #1 performed the ROI definition twice (grey box plots), and Operator #2 performed the ROI definition once (white box plots).

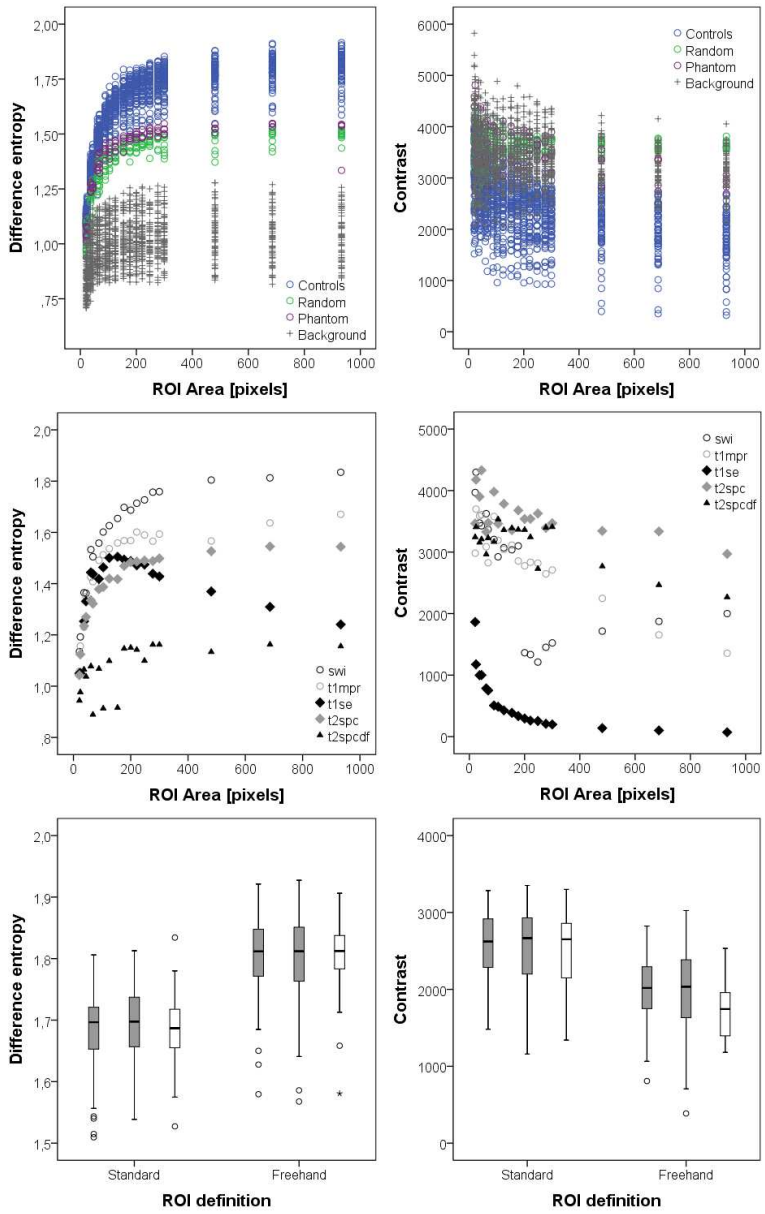

Figure 5.5: Scatter and box plots illustrating the information content and robustness of GLCM *difference entropy* and *contrast*. **Top**: Feature values for the following textures using different ROI sizes: brain (controls – blue), artificial noise image (random – green), homogeneous MRI phantom (phantom – purple), and air (background – grey). **Middle**: Feature values for the homogeneous MRI phantom imaged with the following five imaging sequences: susceptibility-weighted imaging (swi), T1-weighted MPRAGE (t1mpr), T1-weighted spin echo (t1se), T2-weighted SPACE (t2spc), and T2-weighted FLAIR (t2spcdf). **Bottom**: Intra- and inter-observer variation for two ROI types: standard-size circular ROIs and freehand ROIs placed on the centrum semiovale. Operator #1 performed the ROI definition twice (grey box plots), and Operator #2 performed the ROI definition once (white box plots).

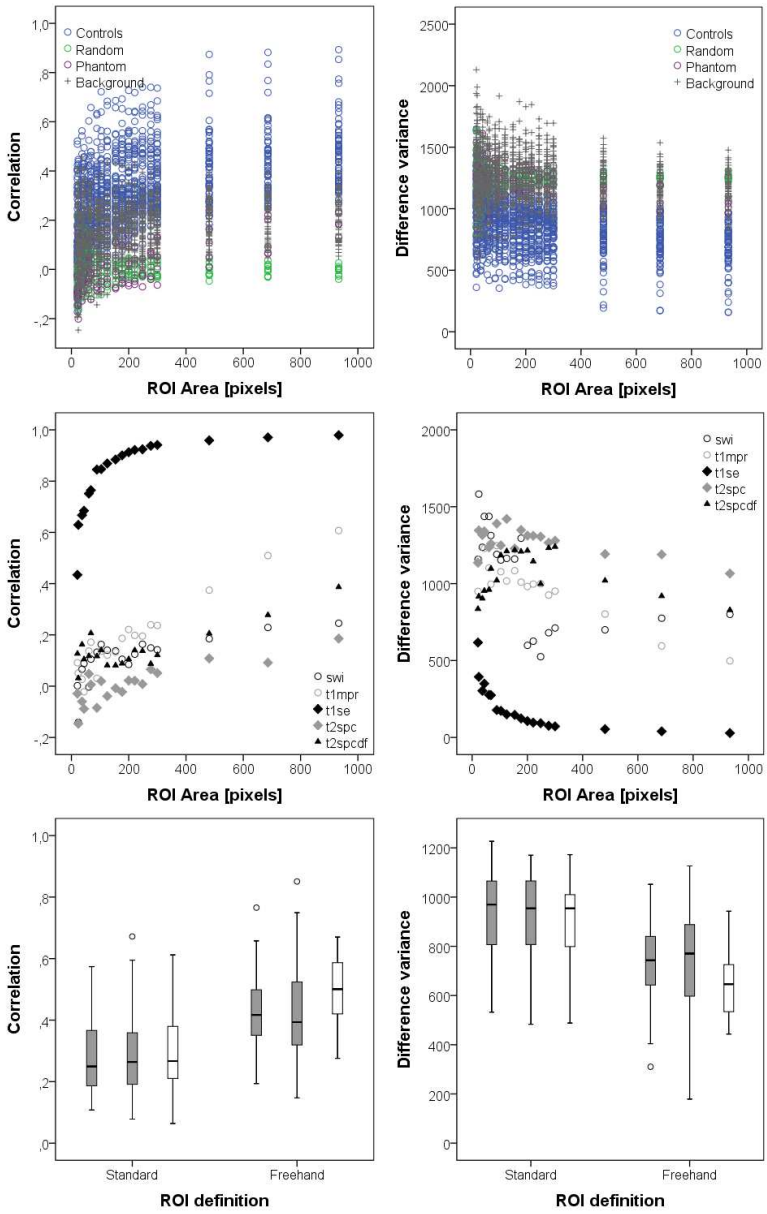

Figure 5.6: Scatter and box plots illustrating the information content and robustness of GLCM *correlation* and *difference variance*. **Top**: Feature values for the following textures using different ROI sizes: brain (controls – blue), artificial noise image (random – green), homogeneous MRI phantom (phantom – purple), and air (background – grey). **Middle**: Feature values for the homogeneous MRI phantom imaged with the following five imaging sequences: susceptibility-weighted imaging (swi), T1-weighted MPRAGE (t1mpr), T1-weighted spin echo (t1se), T2-weighted SPACE (t2spc), and T2-weighted FLAIR (t2spcdf). **Bottom**: Intra- and inter-observer variation for two ROI types: standard-size circular ROIs and freehand ROIs placed on the centrum semiovale. Operator #1 performed the ROI definition twice (grey box plots), and Operator #2 performed the ROI definition once (white box plots).

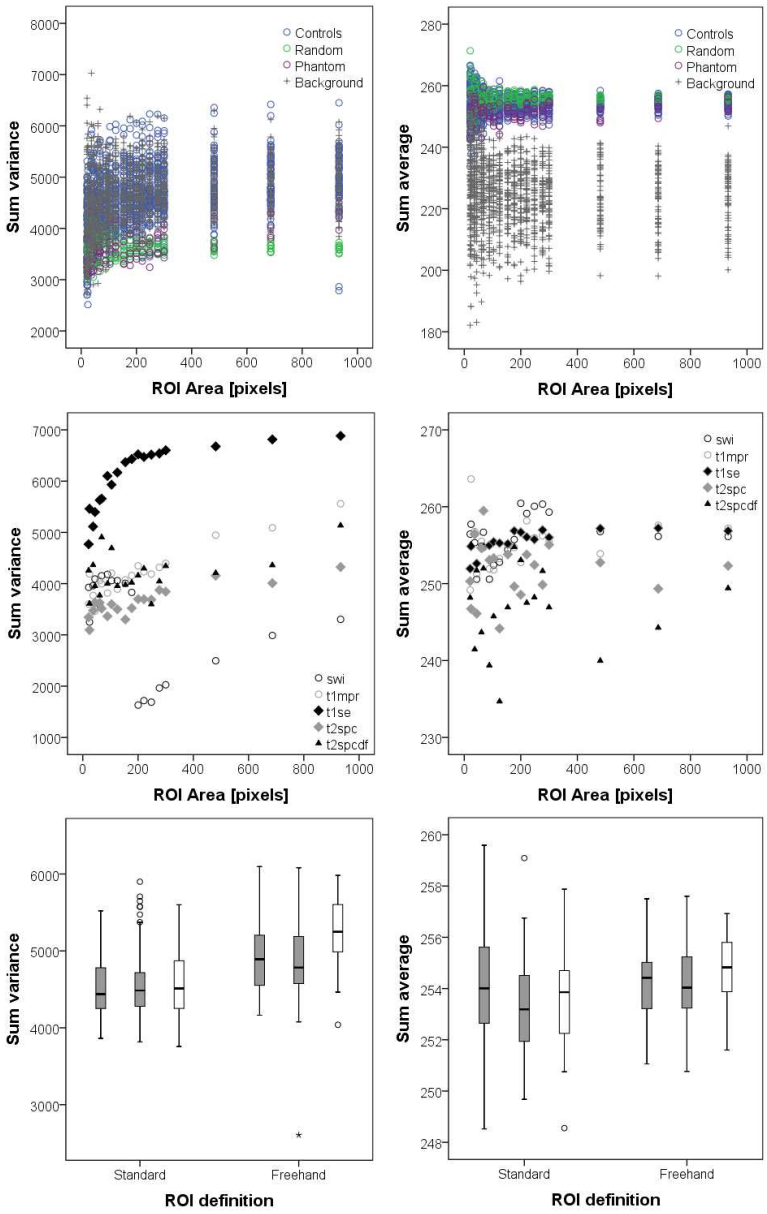

Figure 5.7: Scatter and box plots illustrating the information content and robustness of GLCM *sun variance* and *sum average*. **Top**: Feature values for the following textures using different ROI sizes: brain (controls – blue), artificial noise image (random – green), homogeneous MRI phantom (phantom – purple), and air (background – grey). **Middle**: Feature values for the homogeneous MRI phantom imaged with the following five imaging sequences: susceptibility-weighted imaging (swi), T1-weighted MPRAGE (t1mpr), T1-weighted spin echo (t1se), T2-weighted SPACE (t2spc), and T2-weighted FLAIR (t2spcdf). **Bottom**: Intra- and inter-observer variation for two ROI types: standard-size circular ROIs and freehand ROIs placed on the centrum semiovale. Operator #1 performed the ROI definition twice (grey box plots), and Operator #2 performed the ROI definition once (white box plots).

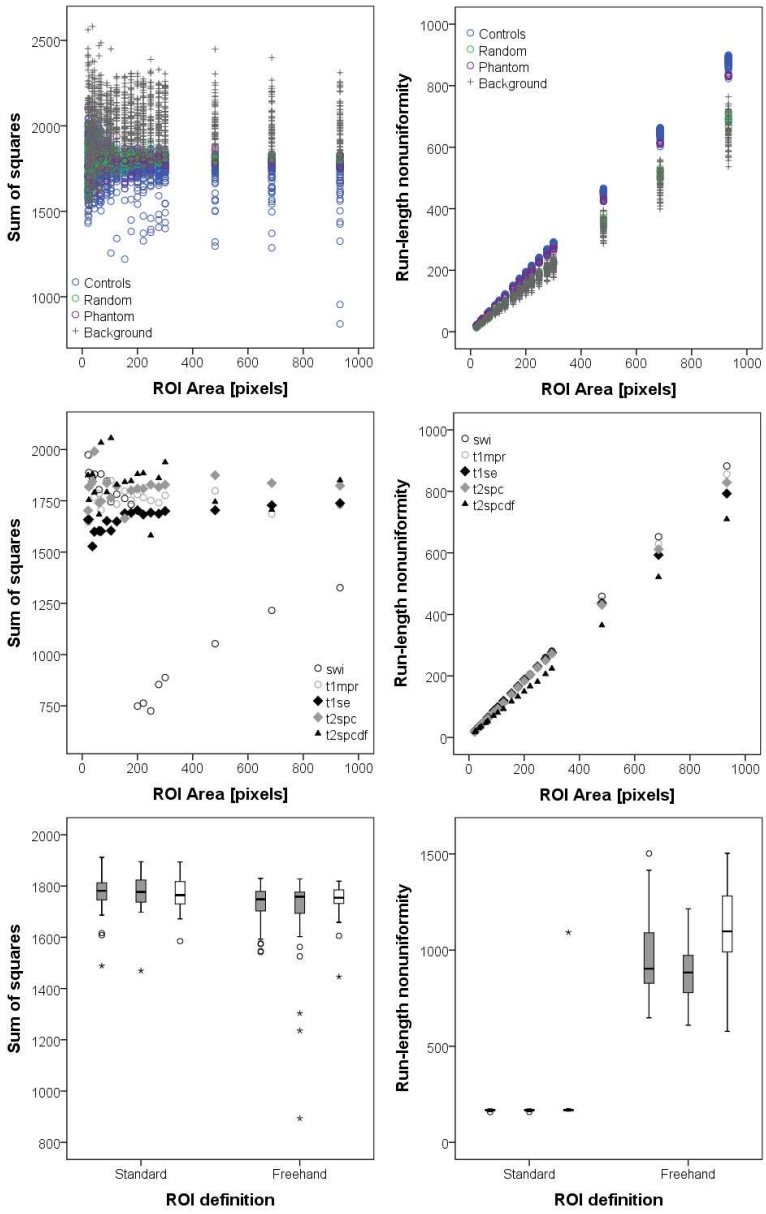

Figure 5.8: Scatter and box plots illustrating the information content and robustness of GLCM *sum of squares* and GLRLM *run-length nonuniformity*. **Top**: Feature values for the following textures using different ROI sizes: brain (controls – blue), artificial noise image (random – green), homogeneous MRI phantom (phantom – purple), and air (background – grey). **Middle**: Feature values for the homogeneous MRI phantom imaged with the following five imaging sequences: susceptibility-weighted imaging (swi), T1-weighted MPRAGE (t1mpr), T1-weighted spin echo (t1se), T2-weighted SPACE (t2spc), and T2-weighted FLAIR (t2spcdf). **Bottom**: Intra- and inter-observer variation for two ROI types: standard-size circular ROIs and freehand ROIs placed on the centrum semiovale. Operator #1 performed the ROI definition twice (grey box plots), and Operator #2 performed the ROI definition once (white box plots).

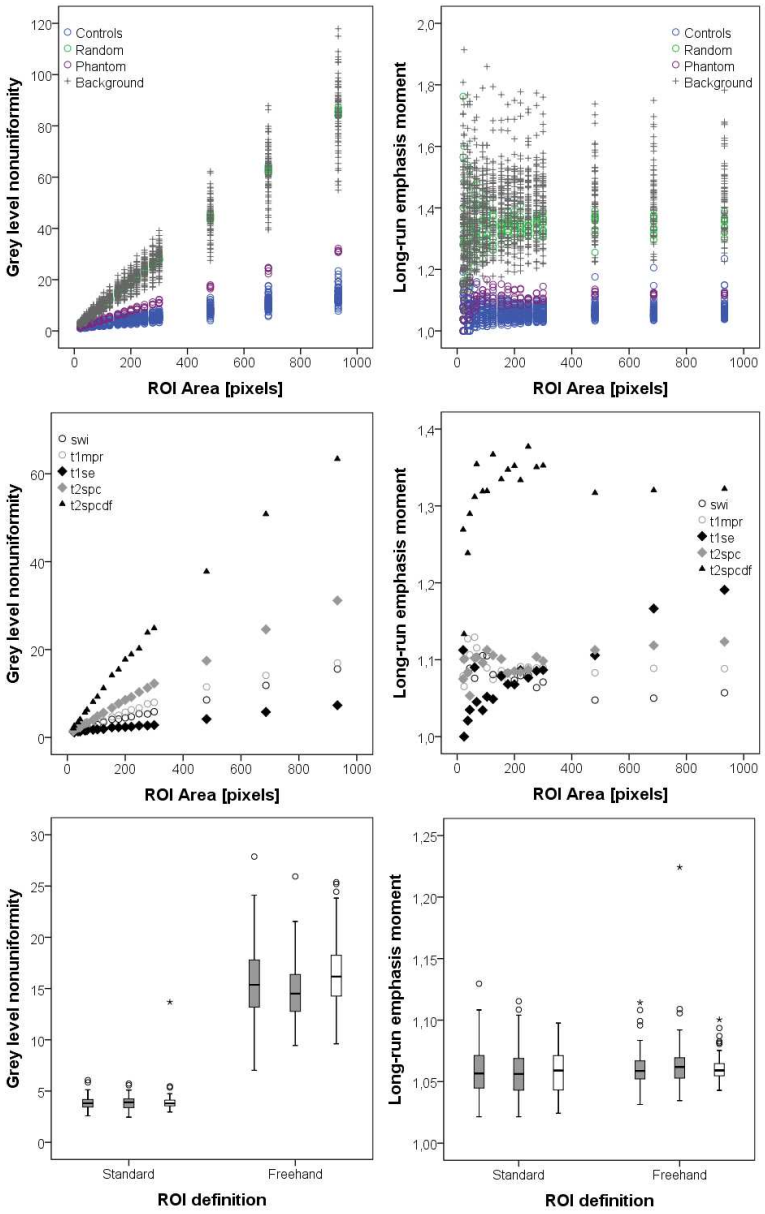

Figure 5.9: Scatter and box plots illustrating the information content and robustness of GLRLM *grey level nonuniformity* and *long-run emphasis moment*. **Top**: Feature values for the following textures using different ROI sizes: brain (controls – blue), artificial noise image (random – green), homogeneous MRI phantom (phantom – purple), and air (background – grey). **Middle**: Feature values for the homogeneous MRI phantom imaged with the following five imaging sequences: susceptibility-weighted imaging (swi), T1-weighted MPRAGE (t1mpr), T1-weighted spin echo (t1se), T2-weighted SPACE (t2spc), and T2-weighted FLAIR (t2spcdf). **Bottom**: Intra- and inter-observer variation for two ROI types: standard-size circular ROIs and freehand ROIs placed on the centrum semiovale. Operator #1 performed the ROI definition twice (grey box plots), and Operator #2 performed the ROI definition once (white box plots).

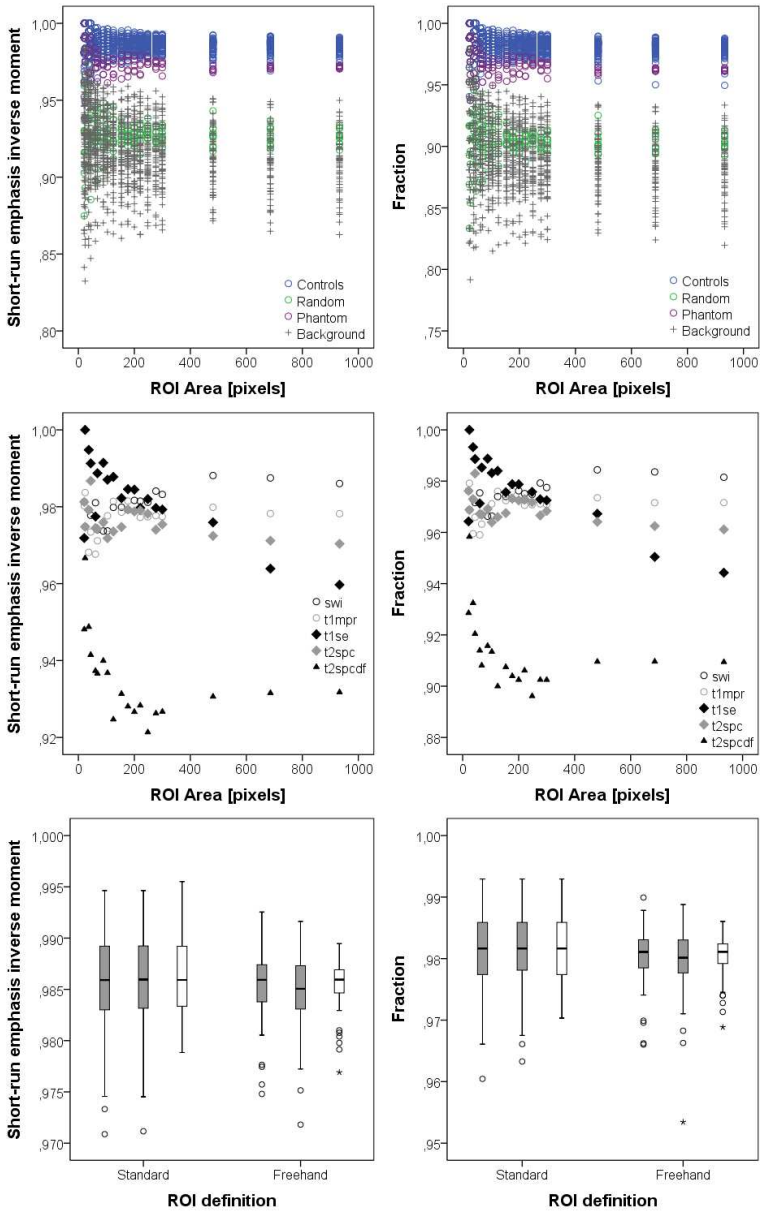

Figure 5.10: Scatter and box plots illustrating the information content and robustness of GLRLM *short-sun emphasis inverse moment* and *fraction*. **Top**: Feature values for the following textures using different ROI sizes: brain (controls – blue), artificial noise image (random – green), homogeneous MRI phantom (phantom – purple), and air (background – grey). **Middle**: Feature values for the homogeneous MRI phantom imaged with the following five imaging sequences: susceptibility-weighted imaging (swi), T1-weighted MPRAGE (t1mpr), T1-weighted spin echo (t1se), T2-weighted SPACE (t2spc), and T2-weighted FLAIR (t2spcdf). **Bottom**: Intra- and inter-observer variation for two ROI types: standard-size circular ROIs and freehand ROIs placed on the centrum semiovale. Operator #1 performed the ROI definition twice (grey box plots), and Operator #2 performed the ROI definition once (white box plots).

5.1.1 Histogram-based features

Figures 5.1 and 5.2 show that the values of histogram-based features are not dependent on ROI size. The *variance* (Figure 5.1), *skewness* (Figure 5.2), and *kurtosis* (Figure 5.2) of the MR image background texture were indistinguishable from other textures. Naturally, the MRI sequence affects the *mean* (Figure 5.1) values of homogeneous textures because this feature is related to single pixels and provides information regarding the overall grey scale distribution within the ROI. It should be noted that the histogram features are not normalized in MaZda software.

5.1.2 Grey level co-occurrence matrix-based features

Because GLCM-based features relate to pixel pairs, these features seem to carry information about the underlying structure of an image. In particular, features describing the homogeneity or the complexity of the texture: *angular second moment* (Figure 5.3), *inverse difference moment* (Figure 5.3), *entropy* (Figure 5.4), *sum entropy* (Figure 5.4), and *difference entropy* (Figure 5.5) were able to distinguish random and background textures from MR image textures of the centrum semiovale and homogeneous phantom. *Angular second moment* and *entropy* were also quite robust to the choice of imaging sequence. However, *contrast* (Figure 5.5), *correlation* (Figure 5.6), *difference variance* (Figure 5.6), and *sum variance* (Figure 5.7) did not clearly distinguish the MR image texture from artificial or background textures and were widely distributed for also homogeneous textures. Background texture was distinguishable based on *sum average* (Figure 5.7), but MR image texture was indistinguishable from artificial noise and phantom textures. All textures overlapped based on *sum of squares* (Figure 5.8).

5.1.3 Grey level run-length matrix-based features

The linearly size-dependent features *run-length* (Figure 5.8) and *grey level nonuniformity* (Figure 5.9) were able to separate background and random textures from MR image textures. The MR image brain texture was also distinguishable from the phantom texture when using larger ROI sizes. Other GLRLM features (*long-run emphasis moment* (Figure 5.9), *short-run emphasis inverse moment* (Figure 5.10), and *fraction* (Figure 5.10) were independent of ROI size. The distributions of brain and phantom textures overlapped but were different from noise textures, at least when using larger ROIs. Among the GLRLM features, only *run-length nonuniformity* produced quite similar values for the homogeneous phantom texture using different imaging sequences.

Table 5.1: Mean and standard deviation values for texture features obtained from phantoms imaged with following textures: brain (controls), artificial noise image (random), homogeneous MRI phantom (phantom), and air in MRI scan (background).

Feature	**Controls**	**Random**	**Phantom**	**Background**
Histogram mean	266 [49]	129 [11]	193 [2]	7 [2]
Histogram variance	370 [330]	5800 [700]	60 [10]	8 [4]
Histogram skewness	0.154 [0.508]	-0.006 [0.182]	0.104 [0.212]	0.509 [0.269]
Histogram kurtosis	0.359 [2.688]	-1.024 [0.219]	-0.234 [0.265]	0.001 [0.730]
GLCM angular second moment	0.0086 [0.0095]	0.0205 [0.0124]	0.0099 [0.0098]	0.0224 [0.0131]
GLCM contrast	2490 [630]	3630 [240]	3560 [420]	3420 [510]
GLCM correlation	0.293 [0.169]	-0.005 [0.055]	0.016 [0.096]	0.146 [0.113]
GLCM sum of squares	1780 [110]	1810 [60]	1810 [80]	2010 [160]
GLCM inverse difference moment	0.031 [0.010]	0.109 [0.023]	0.043 [0.012]	0.123 [0.032]
GLCM sum average	254 [3]	256 [3]	251 [3]	224 [11]
GLCM sum variance	4530 [610]	3600 [210]	3670 [350]	4600 [600]
GLCM sum entropy	1.81 [0.32]	1.48 [0.18]	1.60 [0.22]	1.26 [0.15]
GLCM entropy	2.32 [0.46]	1.81 [0.20]	2.22 [0.40]	1.79 [0.24]
GLCM difference variance	890 [220]	1240 [100]	1220 [120]	1260 [200]
GLCM difference entropy	1.58 [0.21]	1.36 [0.15]	1.41 [0.15]	0.99 [0.12]
GLRLM run-length nonuniformity	211 [220]	167 [175]	200 [210]	161 [166]
GLRLM grey level nonuniformity	4.4 [3.5]	21.1 [21.2]	8.6 [7.7]	21.5 [21.8]
GLRLM long-run emphasis	1.06 [0.03]	1.33 [0.08]	1.11 [0.03]	1.39 [0.12]
GLRLM short-run emphasis	0.986 [0.006]	0.929 [0.014]	0.973 [0.007]	0.919 [0.022]
GLRLM fraction	0.982 [0.008]	0.908 [0.019]	0.965 [0.010]	0.894 [0.027]

Table 5.2: Mean and standard deviation values for the homogeneous MRI phantom imaged with the following five imaging sequences: SWI, T1-weighted MPRAGE (T1MPR), T1-weighted SE (T1SE), and T2-weighted FLAIR (T2SPCDF). The values from T2-weighted SPACE (T2SPC) sequence are presented in Table 5.1 (phantom).

Feature	**SWI**	**T1MPR**	**T1SE**	**T2SPCDF**
Histogram mean	390 [3]	502 [3]	1120 [8]	164 [1]
Histogram variance	391 [207]	128 [41]	1240 [1160]	10 [1]
Histogram skewness	-2.27 [2.61]	-0.12 [0.17]	-0.17 [0.13]	-0.04 [0.14]
Histogram kurtosis	21.2 [26.7]	-0.4 [0.3]	-0.9 [0.1]	-0.3 [0.4]
GLCM angular second moment	0.0085 [0.0097]	0.0088 [0.0097]	0.0085 [0.0098]	0.0170 [0.0094]
GLCM contrast	2630 [1004]	2880 [610]	540 [460]	3140 [350]
GLCM correlation	0.112 [0.088]	0.192 [0.159]	0.833 [0.144]	0.143 [0.081]
GLCM sum of squares	1460 [470]	1780 [70]	1660 [50]	1830 [110]
GLCM inverse difference moment	0.043 [0.007]	0.040 [0.007]	0.067 [0.036]	0.102 [0.012]
GLCM sum average	256 [3]	255 [3]	256 [3]	247 [6]
GLCM sum variance	3210 [970]	4230 [510]	6110 [610]	4190 [400]
GLCM sum entropy	1.79 [0.30]	1.72 [0.26]	1.89 [0.37]	1.34 [0.14]
GLCM entropy	2.32 [0.47]	2.29 [0.45]	2.32 [0.47]	1.91 [0.23]
GLCM difference variance	1030 [330]	1000 [200]	190 [150]	1060 [150]
GLCM difference entropy	1.60 [0.20]	1.48 [0.17]	1.38 [0.14]	1.07 [0.10]
GLRLM run-length nonuniformity	210 [229]	205 [221]	202 [206]	169 [182]
GLRLM grey level nonuniformity	4.4 [3.7]	5.7 [4.4]	2.6 [1.6]	17.9 [16.7]
GLRLM long-run emphasis	1.08 [0.02]	1.09 [0.02]	1.08 [0.05]	1.32 [0.06]
GLRLM short-run emphasis	0.980 [0.004]	0.977 [0.004]	0.982 [0.010]	0.935 [0.011]
GLRLM fraction	0.975 [0.005]	0.971 [0.005]	0.976 [0.014]	0.913 [0.014]

Table 5.3: Mann Whitney U-test p-values for intra- and inter-observer tests. First two columns show p-values for standard ROI setting compared between Operators #1 and #2; and between the first and second operating rounds by Operator #1 (with two-week interval). Next two columns show equal values for freehand ROIs and the last column presents p-values when comparing standard and freehand ROI setting performed by Operator #1.

Feature	**Standard**		**Freehand**		**Operator #1**
	Operator #1 vs. #2	**Round #1 vs. #2**	**Operator #1 vs. #2**	**Round #1 vs. #2**	**Standard vs. freehand**
Histogram mean	0.205	0.841	0.299	0.905	**<0.001**
Histogram variance	0.708	0.617	0.059	0.853	0.930
Histogram skewness	**0.046**	0.640	0.338	0.905	0.406
Histogram kurtosis	0.834	0.864	**0.045**	0.517	0.361
GLCM angular second moment	0.713	0.971	**0.001**	0.269	0.382
GLCM contrast	0.495	0.992	**0.001**	0.886	0.062
GLCM correlation	0.590	0.982	**<0.001**	0.932	**0.049**
GLCM sum of squares	0.482	0.801	0.281	0.890	0.887
GLCM inverse difference moment	0.958	0.692	**0.023**	0.358	0.503
GLCM sum average	0.613	**0.032**	0.134	0.732	**0.005**
GLCM sum variance	0.622	0.898	**<0.001**	0.630	**0.039**
GLCM sum entropy	0.942	0.624	**0.002**	0.496	0.215
GLCM entropy	0.773	0.883	**<0.001**	0.303	0.393
GLCM difference variance	0.224	0.928	**<0.001**	0.868	**0.046**
GLCM difference entropy	0.875	0.526	0.793	0.768	0.578
GLRLM run-length nonuniformity	0.880	0.748	**<0.001**	0.064	0.274
GLRLM grey level nonuniformity	0.689	0.989	0.237	0.065	0.981
GLRLM long-run emphasis	0.890	0.543	0.732	0.345	0.769
GLRLM short-run emphasis	0.979	0.531	0.660	0.253	0.696
GLRLM fraction	0.875	0.654	0.708	0.301	0.700

Table 5.4: Summary of TA feature behaviour.

Feature	ROI size dependence	Controls vs. random	Controls vs. phantom	Controls vs. background	Effect of imaging sequence
Histogram mean, GLCM sum average	No	Overlap	Overlap	Distinguishable	High
Histogram variance	No	Distinguishable	Overlap	Overlap	High
Histogram skewness and kurtosis, GLCM sum of squares	No	Overlap	Overlap	Overlap	Low
GLCM entropy	Yes	Distinguishable	Distinguishable	Distinguishable	Low
GLCM sum entropy, difference entropy	Yes	Distinguishable	Distinguishable	Distinguishable	High
GLCM angular second moment	No	Distinguishable	Overlap	Distinguishable	Low
GLCM inverse difference moment	No	Distinguishable	Overlap	Distinguishable	High
GLCM contrast, correlation, sum variancce, difference variance	No	Overlap	Overlap	Distinguishable	Low
GLRLM run-length nonuniformity	Yes	Distinguishable	Overlap	Distinguishable	Low
GLRLM grey level nonuniformity	Yes	Distinguishable	Overlap	Distinguishable	High
GLRLM long-run empasis, short-sun emphasis inverse moments, fraction	No	Distinguishable	Overlap	Overlap	High

5.2 Textural features in Parkinson's disease, stroke, and muscle adaptation studies

A selected set of TA features was applied in Parkinson's disease, stroke, and muscle adaptation studies to reveal differences and changes that are invisible to the human eye in MR images. A summary of the results obtained from Studies II-V is presented in Table 5.5.

Table 5.5: Summary of TA features used as tools in three different medical applications.

Feature	**Parkinson's disease (Studies II, III)**	**Exercise-load (Study IV)**	**Cerebral infarction (Study V)**
GLCM angular second moment	Differences in the brain stem and mesencephalon between PD patients and controls, changes in the midbrain during the follow-up of PD patients, and correlation with clinical scores	Differences in thigh muscles and subcutaneous fat tissue between athletes and controls, robust to slice selection	Differences between the ipsilateral and unaffected sides of the brain at the infarction site
GLCM inverse difference moment	Differences in the midbrain between PD patients and controls, changes in the midbrain during the follow-up of PD patients	Differences in thigh muscles, bone marrow, and subcutaneous fat tissue between athletes and controls, robust to slice selection	No differences detected
GLCM entropy	Differences in the brain stem and mesencephalon between PD patients and controls, changes in the midbrain during the follow-up of PD patients, correlation with clinical scores	Differences in thigh muscles and subcutaneous fat tissue between athletes and controls, robust to slice selection	Differences between the ipsilateral and unaffected sides of the brain at the infarction site and centrum semiovale
GLCM difference entropy	Differences in the brain stem, mesencephalon, and midbrain between PD patients and controls, changes in the midbrain during the follow-up of PD patients, correlation with clinical scores	Differences in thigh muscles, bone marrow, and subcutaneous fat tissue between athletes and controls, robust to slice selection	Differences between the ipsilateral and unaffected sides of the brain at the infarction site, correlation with DTI parameters
GLCM contrast, correlation, sum variance, difference variance	Interhemispheric differences in the brain stem, mesencephalon and midbrain of PD patients	Not used	Not used

6 Discussion

In medical imaging, TA can be used to recognise, classify, or segment image patterns, such as pathological tissue alterations, which can be difficult or impossible to observe by human visual perception. To apply TA in medical applications, the method should be reliable and repeatable. In a recent paper, Lerski et al. (2015) provided technical recommendations regarding the use of TA methodology for muscle MRI. The authors emphasised the importance of performing a quality assessment of the MR imaging system, careful choice of the imaging sequence, and normalisation of the obtained MR images. They also stated that textures should be calculated within ROIs that are larger than 100 pixels, and the dynamic range of the images should be reduced to six or eight bits. They recommended considering a wide range of TA methods but advised against the over-interpretation of the texture data due to the large number of texture features. This thesis continues this valuable work concerning TA methodology by assessing the information yielded by different features and by evaluating the effects of MRI sequence and ROI definition on TA features.

6.1 Information regarding textural features

6.1.1 Histogram-based features

First-order histogram features are capable of identifying textures with different grey level distributions. Textures with differing *mean* and *variance* can often be distinguished by the human eye as dark or light and smooth or coarse, respectively. However, textures with differing *skewness* and *kurtosis* do not always appear different by visual inspection. Our results indicated their vulnerability to variations in image intensity. In addition, intra- and inter-observer variability had little effect on the histogram feature values, although their value ranges were wide, and they produced many outliers.

6.1.2 Grey level co-occurrence matrix-based features

The GLCM method has been widely utilised in MR image TA. An increasing number of studies considers the behaviour and results for single TA features instead of using a set of selected features. Although multivariable analyses may also perform well and distinguish textures one remains unsure of the capability of single feature. Understanding the behaviour of single features may aid in the development of more specific analyses in future studies.

Homogeneity and complexity features have shown promising results in various medical MRI TA studies. According to our results, the information provided by these features appears to describe the textural structures of the tissues because the MR image background

barely overlapped with brain textures. The values were, however, dependent on ROI size; thus, care should be taken when calculating these features within ROIs of different sizes.

Mahmoud-Ghoneim et al. (2006) applied TA as a non-invasive method for muscle MRI investigation to discriminate three muscle conditions in rats: normal, atrophy, and regeneration. The authors found that GLCM *angular second moment* and *entropy* were the most discriminative features and demonstrated that despite their different microscopic scales, gastrocnemius muscle fibres yielded results that were statistically consistent with histological findings during atrophy and regeneration. In a recent lung cancer study by Yoon et al. (2016), *entropy* was the strongest independent predictor of survival in patients with lung cancer. *Entropy* also yielded the least inter-observer variability among MR histogram and texture parameters.

Our Studies II and III concentrated on MR images of patients with symptoms of Parkinson's disease. The value of TA in finding differences between patients and controls, interhemispheric differences, and longitudinal changes in clinically interesting areas of the brain was evaluated. Based on earlier studies, we assumed that TA could reveal subtle changes in the MR images caused by PD that are invisible to the human eye and that asymmetric changes caused by PD may also be present. MR image textures of patients with PD and the control group differed in these areas in one or more of the following features: *angular second moment*, *inverse difference moment*, *entropy*, and *difference entropy*. These features were also able to reveal subtle changes in MR image textures during the 2-year follow-up of the PD patients.

GLCM homogeneity and complexity features were also used in our Study IV, where we identified differences in MR image textures obtained for thigh soft tissues between various athlete groups and non-athletes. The adaptation to different exercise loads was associated with the MR image textures of the thigh muscles, bone marrow, and subcutaneous fat.

In Study V, we compared the textures of specific brain areas along the white matter tracts in the MR images of right-sided stroke patients. We found that *angular second moment* values were lower and that both *entropy* feature values were higher at the lesion site compared to the reference area on the left hemisphere. The same trend was found for the centrum semiovale. These results indicate that the brain tissue texture in the ipsilateral hemisphere is more heterogeneous and complex than that on the contralateral side. Thus, damaged tissue might appear more coarse and random in texture compared to healthy tissue. Similar results were obtained in previous MRI studies of mild brain injuries (Holli et al., 2010) and epilepsy (Suoranta et al., 2013).

In addition to homogeneity and complexity features, our studies II and III revealed interhemispheric differences in the brain stem, mesencephalon, and midbrain areas of the patients with PD for *contrast*, *correlation*, *sum variance*, and *difference variance*. Yu et al. (2015) used histogram-, GLCM-, GLRLM, gradient- and Law's feature-based TA to analyse proton density maps to quantify hepatic fibrosis in a murine disease model. The GLCM features *correlation* and *contrast* demonstrated moderate-to-strong correlations with hepatic fibrosis. According to our results obtained from Study I, these features were less dependent on ROI size, but the values were widely spread, and the MR image brain texture overlapped with artificial, homogeneous, and background textures. These features were more related to the intensity values of the pixels and were also vulnerable to differences in image intensity and noise levels. The feature values obtained from the MR image textures varied over such a wide range that they were most likely influenced by the image intensity variations. Hence, more uniform image normalisation is needed to fully benefit from the use of these features.

Our study I showed that the GLCM features *sum of squares* and *sum average* appeared quite independent of ROI size. However, the values of *sum of squares* and *sum average* that were obtained from the MR images overlapped with the values obtained from the artificial random texture. Thus, these features might not reveal additional information regarding the underlying texture in this application.

Based on our results, GLCM features, especially features related to homogeneity and complexity, appeared robust and applicable to clinical MR image analysis concerning at least brain and muscles. These features appeared to reveal information about the true tissue structure. In addition, a phantom study of Mayerhoefer et al. (2009) demonstrated that GLCM features were superior to features derived from the GLRLM, absolute gradient, autoregressive model, and wavelets. The GLCM features enabled the discrimination of different patterns that were close to the resolution limits for the smallest structures of physical texture and functioned even for datasets that were heterogeneous with regard to various acquisition parameters, including spatial resolution.

6.1.3 Grey level run-length matrix-based features

Our results showed that the GLRLM features *run length nonuniformity* and *grey level nonuniformity* were quite linearly dependent, whereas *short-run emphasis*, *long-run emphasis*, and *fraction* were independent of ROI size. The behaviour of the nonuniformity parameters originates from the definition of the RLM features because *run-length nonuniformity* squares the number of grey levels for each run length, and *grey level nonuniformity* squares the number of run lengths for each grey level. Thus, for a larger ROI, there exist more runs, and the values of the nonuniformity features were dominated by the ROI size. All GLRLM features, however, provided clearly differing values for the brain MR image textures compared to the background and random patterns. The range of the samples was also relatively compact; therefore, these parameters appear robust and valuable for various TA studies. Our research group found that GLRLM features were capable of differentiating between aggressive and indolent lymphomas (Wu et al., 2016). Yang et al. (2015) demonstrated in their TA study that the neural subtype of glioblastoma was best predicted by GLRLM features. Thus, GLRLM features are appropriate for medical MR image TA, provided that the ROI size dependence is acknowledged.

6.2 Texture analysis in the medical environment

6.2.1 Imaging sequences

Essentially, the grey level value of an image pixel is determined by the MRI sequence used. A wide range of imaging sequences has been used in TA studies, and none has proven superior. This can be considered as strength of the method. However, our results in this thesis showed that even homogenous phantom textures produce differing feature values when imaged with differing MR sequences. Mayerhoefer et al. (2009) showed that texture features derived from the GLCM, GLRLM, gradient, AR model, and wavelets were increasingly sensitive to acquisition parameter variations with increasing spatial resolution of the T2-weighted multislice multiecho images. Nevertheless, provided that the spatial resolution was sufficiently high, variations in TR and TE had little effect on the results of pattern discrimination. Moreover, our results showed that some features are more sensitive to sequence variation than others. For example, GLCM *angular second*

moment and GLRLM *run-length nonuniformity* appeared quite robust to the imaging sequence choice in our phantom study.

Some studies comparing several sequences for MRI TA have been performed, but the results vary regarding the best option. A texture-based segmentation method applied by Saeed et al. functioned equally well when distinguishing whole brain from T1- and T2-weighted, FLAIR, and angio sequence images. Recently, our group studied the differentiation of lymphoma types based on T1-weighted pre- and post-contrast enhancement images and T2-weighted images with and without fat suppression (Wu et al., 2016). The best classification results were obtained from the T1-weighted post-contrast images. However, all sequences had advantages and disadvantages.

In practice, medical MRI is often performed according to a clinical protocol that includes diagnostic sequences. These sequences are usually optimised for use by radiologists, i.e., by the human eye. Advanced image analysis methods may reveal the most additional information based on structural sequences rather than heavily T1- or T2-weighted images. However, despite the weighting of the sequence, attention should be paid to the signal-to-noise ratio, acquiring sufficient resolution, and the imaging time. Lerski et al. (2015) discussed this topic in a review of technical recommendations regarding muscle MR image TA, in which they also emphasised the relevance of sequence selection for studying histological variations, which change during, e.g., a muscle disease. The selection of a suitable MRI sequence, therefore, represents a balance between imaging time, image quality, and the amount of textural information in the image.

6.2.2 Region of interest definition

The selection of a ROI defines the window within which the features are calculated. It should represent the tissue or structure of interest while avoiding other tissues and structures. At the same time, the ROI should contain a sufficient number of pixels for reliable feature calculation. As usual in signal processing, when observing textures from regions that are too small, the variation between samples increases. This was also seen in our studies, especially regarding the GLCM homogeneity and complexity features. On average, circular ROIs containing less than 100 pixels from different images yielded values in a wide range. In addition, when using ROIs larger than approximately 200 pixels, the textural information inside the ROI appeared to be lost in the abundance of pixels. Neither partial volume pixels nor even whole pixels of surrounding structures (which inevitably appeared in our example of centrum semiovale, on average, in ROIs larger than 200-300 pixels in diameter) appeared to have much impact on the feature values. This raises the question as to whether these GLCM parameters carry specific information after the saturation point. Hence, according to our results, rather than using a ROI as large as possible, the ROI should be suited to the structure or area under inspection. In addition, one should prefer standard ROIs of a fixed size and shape or freehand ROIs of approximately the same size because ROI size affects the values obtained.

6.2.3 Data analysis and interpretation

As reviewed earlier, hundreds of textural features can be calculated for a single ROI. This thesis has covered features based on the image histogram, GLCM, and GLRLM. In addition, several possible methods and features based on these methods exist. The calculated TA features, similar to all measures, may be analysed in various ways, e.g., as single feature values or as combinations of texture features and possibly other measures.

According to our results, the averaged second-order textural features are functional in medical brain and muscle MR image TA. When the information content of the features is known, the method may offer valuable additional information that is unobtainable by the human eye. As already stated, Lerski et al. (2015) advised against the over-interpretation of the texture data due to large number of texture features. This originates to the fact that if any two images are classified with several hundreds of features, some features will inevitably differentiate these textures. However, the clinical relevance will be questionable. Instead, understanding the properties and limitations of single features will help us combine the information of texture features and tissue properties.

Not every TA study has to be performed with similar data analysis method, and the data analysis method should not judge the quality of the research. However, based on our research work in medical MRI environment, the single feature values and conclusions based on them seem to be preferred to complex multi-parameter analyses. These results may not be suitable for generalization because of individual variation, but this thesis offers tools for popularisation of TA methods.

7 Conclusions

On the basis of this study, we recommend to focus on second-order texture features that relate to more than one pixel and ensure the use of appropriate preprocessing steps prior to image analysis (Study I). Our results have shown that all textural features have limitations regarding the discrimination capacity in medical MR images and dependence on ROI size and MR imaging parameters. However, despite these limitations, it is possible to perform quantitative analysis on medical MR images (Studies II-V).

1) Our results demonstrate that histogram parameters are highly dependent on variations in image contrast and brightness, and provide little additional information to that obtained by visual inspection. Features based on the GLCM and GLRLM contain information that cannot be evaluated visually. The size-dependence of specific features should be noted by standardizing the size and shape of the ROI.

2) When the technical aspects and limitations of texture features are appropriately considered, some texture features, such as GLCM homogeneity and complexity features, have high potential for revealing, for example, tissue pathology. Based on our results these features could detect textural brain stem and midbrain differences between PD patients and controls and changes in brain structure textures during disease progress. These features were also capable of revealing textural differences between ipsilateral and unaffected sides of the brain on stroke patients and correlated with DTI parameters. In addition, these features were associated with thigh muscle adaptation to exercise.

   The second-order features are more robust to variations in image data than histogram features. However, care must be taken that the observed differences or changes originate from the texture rather than from variations in intensity that result from the technical aspects of MRI.

8 Appendix I

Histogram-based features

Mean	$\mu = \sum_{i=1}^{N} ip(i)$
Variance	$\sigma^2 = \sum_{i=1}^{N}(i-\mu)^2 p(i)$
Skewness	$\mu_3 = \sigma^{-3}\sum_{i=1}^{N}(i-\mu)^3 p(i)$
Kurtosis	$\mu_4 = \sigma^{-4}\sum_{i=1}^{N}(i-\mu)^4 p(i) - 3$

where $p(i)$ is a normalised histogram vector (i.e. histogram whose entries are divided by the number of pixels within the ROI), $i = 1, 2, ..., N_g$ and N denotes for the number of intensity levels in an image.

GLCM-based features

The second-order histogram of an image is defined as the GLCM $P_{d\theta}(i,j)$ where d is the distance in pixels and θ is the angle between two examined pixels. For given image $f(x,y)$ with N_g discrete grey levels, the GLCM is defined such as the (i,j)th element equals to the number of times that $f(x_1,y_1) = i$ and $f(x_2,y_2) = j$ where $(x_2,y_2) = (x_1,y_1)+(d\cos\theta, \sin\theta)$. $R(d,\theta)$ is the total number of neighbouring pixels within given ROI; and the (i,j)th element of normalised GLCM is, thus, $P(i,j)/R = p(i,j)$.

Angular second moment	$f_1 = \sum_{i=1}^{N_g}\sum_{j=1}^{N_g} p(i,j)^2$
Contrast	$f_2 = \sum_{n=0}^{N_g-1} n^2 \sum_{i=1,\lvert i-j\rvert=n}^{Ng}\sum_{j=1}^{N_g} p(i,j)^2$
Correlation	$f_3 = \dfrac{\sum_{i=1}^{N_g}\sum_{j=1}^{N_g} ijp(i,j) - \mu_x\mu_y}{\sigma_x\sigma_y}$
Sum of squares	$f_4 = \sum_{i=1}^{N_g}\sum_{j=1}^{N_g}(i-\mu_x)^2 p(i,j)$
Inverse difference moment	$f_5 = \sum_{i=1}^{N_g}\sum_{j=1}^{N_g}\dfrac{1}{1+(i-j)^2}p(i,j)$

Sum average	$f_6 = \sum_{i=1}^{N_g} \sum_{j=1}^{N_g} i p_{x+y}(i)$
Sum variance	$f_7 = \sum_{i=1}^{N_g} \sum_{j=1}^{N_g} (i - f_6)^2 p_{x+y}(i)$
Sum entropy	$f_8 = -\sum_{i=1}^{N_g} p_{x+y}(i) \log\big(p_{x+y}(i)\big)$
Entropy	$f_9 = -\sum_{i=1}^{N_g} \sum_{j=k}^{N_g} p(i,j) \log\big(p(i,j)\big)$
Difference variance	$f_{10} = \sum_{i=0}^{N_g-1} (i - \mu_{x-y})^2 p_{x-y}(i)$
Difference entropy	$f_{11} = \sum_{i=0}^{N_g-1} p_{x+y}(i) \log\big(p_{x+y}(i)\big)$

where marginal probability matrices $p_x(i) = \sum_{j=1}^{N_g} P(i,j)$ $p_y(j) = \sum_{i=1}^{N_g} P(i,j)$; sum distribution $p_{x+y}(k) = \sum_{i=1,i+j=k}^{N_g} \sum_{j=1}^{N_g} p(i,j)$, $k = 2, 3, ..., 2N_g$; and difference distribution $p_{x-y}(k) = \sum_{i=1,|i-j|=k}^{N_g} \sum_{j=1}^{N_g} p(i,j)$, $k = 0, 1, ..., N_g - 1$. Means (μ) and standard deviations (σ) of p_x, p_y and p_{x+y}, p_{x-y} are μ_x, μ_y, σ_x, σ_y and μ_{x+y}, μ_{x-y}, $\sigma_{x+y}, \sigma_{x-y}$ respectively.

GLRLM-based features

The elements $p(i,j)$ of GLRLM represent the number of times there is a run of length j having grey level i. N_g denotes for the number of grey levels and N_r for the number of runs.

Run-length nonuniformity	$f_{12} = \Big(\sum_{j=1}^{N_r} \big(\sum_{i=1}^{N_g} p(i,j) \big)^2 \Big) / C$
Grey level nonuniformity	$f_{13} = \Big(\sum_{i=1}^{N_g} \big(\sum_{j=1}^{N_r} p(i,j) \big)^2 \Big) / C$
Long-run emphasis moment	$\big(\sum_{i=1}^{N_g} \sum_{j=1}^{N_r} j^2 p(i,j) \big) / C$
Short-run emphasis inverse moment	$\big(\sum_{i=1}^{N_g} \sum_{j=1}^{N_r} \frac{p(i,j)}{j^2} \big) / C$
Fraction	$f_{16} = C / \sum_{i=1}^{N_g} \sum_{j=1}^{N_r} j p(i,j)$

where $C = \sum_{i=1}^{N_g} \sum_{j=1}^{N_r} p(i,j)$

References

Ahlhelm, F., Schneider, G., Backens, M., Reith, W., and Hagen, T., "Time course of the apparent diffusion coefficient after cerebral infarction," *European Radiology*, vol. 12, no. 9, pp. 2322 – 2329, 2002.

Allen, R. L. and Mills, D. W., *Signal analysis - time, frequency, scale and structure*. Wiley-IEEE Press, 2004.

Antonini, A., Leenders, K. L., Meier, D., Oertel, W. H., Boesiger, P., and Anliker, M., "T2 relaxation time in patients with Parkinson's disease," *Neurology*, vol. 43, no. 4, pp. 697 – 700, 1993.

Avril, N., Menzel, M., Dose, J., Schelling, M., Weber, W., Jänicke, F., Nathrath, W., and Schwaiger, M., "Glucose metabolism of breast cancer assessed by 18F-FDG PET: Histologic and immunohistochemical tissue analysis," *Journal of Nuclear Medicine*, vol. 42, no. 1, pp. 9 – 16, 2001.

Baar, K., Nader, G., and Bodine, S., "Resistance exercise, muscle loading/unloading and the control of muscle mass," *Essays in Biochemistry*, vol. 42, pp. 61 – 74, 2006.

Bahl, G., Cruite, I., Wolfson, T., Gamst, A. C., Collins, J. M., Chavez, A. D., Barakat, F., Hassanein, T., and Sirlin, C. B., "Noninvasive classification of hepatic fibrosis based on texture parameters from double contrast-enhanced magnetic resonance images," *Journal of Magnetic Resonance Imaging*, vol. 36, no. 5, pp. 1154 – 1161, 2012.

Blazevich, A. J., Gill, N. D., Bronks, R., and Newton, R. U., "Training-specific muscle architecture adaptation after 5-wk training in athletes," *Medicine and Science in Sports and Exercise*, vol. 35, no. 12, pp. 2013 – 2022, 2003.

Blechinger, J. C., Madsen, E. L., and Frank, G. R., "Tissue-mimicking gelatin-agar gels for use in magnetic resonance imaging phantoms," *Medical Physics*, vol. 15, no. 4, pp. 629 – 636, 1988.

Bloch, F., "Nuclear induction," *Physical Review*, vol. 70, pp. 460 – 474, 1946.

Bousquet-Santos, K., Vaisman, M., Barreto, N. D., Cruz-Filho, R. A., Salvador, B. A., Frontera, W. R., and Nobrega, A. C., "Resistance training improves muscle function and body composition in patients with hyperthyroidism," *Archives of Physical Medicine and Rehabilitation*, vol. 87, no. 8, pp. 1123 – 1130, 2006.

Bracewell, R., *The Fourier transform and its applications*, 3rd ed. New York: McGrawHill, 1999.

Brar, S., Henderson, D., Schenck, J., and Zimmerman, E. A., "Iron accumulation in the substantia nigra of patients with Alzheimer disease and parkinsonism," *Archives of Neurology*, vol. 66, no. 3, pp. 371–374, 2009.

Browning, R. C., Modica, J. R., Kram, R., and Goswami, A., "The effects of adding mass to the legs on the energetics and biomechanics of walking," *Medicine and Science in Sports and Exercise*, vol. 39, no. 3, pp. 515–525, 2007.

Bucciolini, M., Ciraolo, L., and Lehmann, B., "Simulation of biologic tissues by using agar gels at magnetic resonance imaging," *Acta Radiologica*, vol. 30, no. 6, pp. 667–669, 1989.

Camicioli, R., Sabino, J., Gee, M., Bouchard, T., Fisher, N., Hanstock, C., Emery, D., and Martin, W. R., "Ventricular dilatation and brain atrophy in patients with Parkinson's disease with incipient dementia," *Movement Disorders*, vol. 26, no. 8, pp. 1443–1450, 2011.

Chen, C. C., DaPonte, J. S., and Fox, M. D., "Fractal feature analysis and classification in medical imaging," *IEEE Transactions on Medical Imaging*, vol. 8, no. 2, pp. 133–142, 1989.

Collewet, G., Strzelecki, M., and Mariette, F., "Influence of MRI acquisition protocols and image intensity normalization methods on texture classification," *Magnetic Resonance Imaging*, vol. 22, no. 1, pp. 81–91, 2004.

Damadian, R., "Tumor detection by nuclear magnetic resonance," *Science*, vol. 171, no. 3976, pp. 1151–1153, 1971.

Davie, C. A., "A review of Parkinson's disease," *British Medical Bulletin*, vol. 86, pp. 109–127, 2008.

de Oliveira, M. S., Balthazar, M. L., D'Abreu, A., Yasuda, C. L., Damasceno, B. P., Cendes, F., and Castellano, G., "MR imaging texture analysis of the corpus callosum and thalamus in amnestic mild cognitive impairment and mild Alzheimer disease," *American Journal of Neuroradiology*, vol. 32, no. 1, pp. 60–66, 2011.

Dexter, D. T., Carayon, A., Javoy-Agid, F., Agid, Y., Wells, F. R., Daniel, S. E., Lees, A. J., Jenner, P., and Marsden, C. D., "Alterations in the levels of iron, ferritin and other trace metals in Parkinson's disease and other neurodegenerative diseases affecting the basal ganglia," *Brain*, vol. 114, no. 4, pp. 1953–1975, 1991.

Donnan, G. A., Fisher, M., Macleod, M., and Davis, S. M., "Stroke," *Lancet*, vol. 371, no. 9624, pp. 1612–1623, 2008.

Drayer, B., Burger, P., Darwin, R., Riederer, S., Herfkens, R., and Johnson, G. A., "MRI of brain iron," *American Journal of Roentgenology*, vol. 147, no. 1, pp. 103–110, 1986.

Farrar, T. C., "Pulsed and Fourier transform NMR spectroscopy," *Analytical Chemistry*, vol. 42, no. 4, pp. 109A–112A, 1970.

Fetit, A. E., Novak, J., Peet, A. C., and Arvanitits, T. N., "Three-dimensional textural features of conventional MRI improve diagnostic classification of childhood brain tumours," *NMR in Biomedicine*, vol. 28, no. 9, pp. 1174–1184, 2015.

Filler, A. G., Tsuruda, J. S., Richards, T. L., and Howe, F. A., "Images, apparatus, algorithms and methods," 1992.

Fox, M. J., Gibbs, P., and Pickles, M. D., "Minkowski functionals: An MRI texture analysis tool for determination of the aggressiveness of breast cancer," *Journal of Magnetic Resonance Imaging*, vol. 43, no. 4, pp. 903 – 910, 2016.

Freeborough, P. A. and Fox, N. C., "MR image texture analysis applied to the diagnosis and tracking of Alzheimer's disease," *IEEE Transactions on Medical Imaging*, vol. 17, no. 3, pp. 475 – 478, 1998.

Fruehwald-Pallamar, J., Hesselink, J. R., Mafee, M. F., Holzer-Fruehwald, L., Czerny, C., and Mayerhoefer, M. E., "Texture-based analysis of 100 MR examinations of head and neck tumors - is it possible to discriminate between benign and malignant masses in a multicenter trial?" *RoFo : Fortschritte auf dem Gebiete der Rontgenstrahlen und der Nuklearmedizin*, vol. 188, no. 2, pp. 195 – 202, 2016.

Galloway, M. M., "Texture analysis using gray level run lengths," *Computer Graphics and Image Processing*, vol. 4, no. 2, pp. 172 – 179, 1975.

Graham, J. M., Paley, M. N., Grunewald, R. A., Hoggard, N., and Griffiths, P. D., "Brain iron deposition in Parkinson's disease imaged using the PRIME magnetic resonance sequence," *Brain*, vol. 123 Pt 12, pp. 2423 – 2431, 2000.

Griffiths, P. D., Dobson, B. R., Jones, G. R., and Clarke, D. T., "Iron in the basal ganglia in Parkinson's disease. an in vitro study using extended X-ray absorption fine structure and cryo-electron microscopy," *Brain*, vol. 122 (Pt 4), no. Pt 4, pp. 667 – 673, 1999.

Haddad, F. and Adams, G. R., "Aging-sensitive cellular and molecular mechanisms associated with skeletal muscle hypertrophy," *Journal of Applied Physiology*, vol. 100, no. 4, pp. 1188 – 1203, 2006.

Hajek, M., Dezortova, M., Materka, A., and Lerski, R. A., Eds., *Texture Analysis for Magnetic Resonance Imaging*. Prague, Czech Republic: Med4publishing r.s.o., 2006.

Haralick, R. M., "Statistical and structural approaches to texture," *Proceedings of the IEEE*, vol. 67, no. 5, pp. 786 – 804, 1979.

Haralick, R. M., Shanmugam, K., and Dinstein, I., "Textural features for image classification," *IEEE Transactions on Systems, Man and Cybernetics*, vol. 3, no. 6, pp. 610 – 621, 1973.

Harrison, L. C., Nikander, R., Sikio, M., Luukkaala, T., Helminen, M. T., Ryymin, P., Soimakallio, S., Eskola, H. J., Dastidar, P., and Sievanen, H., "MRI texture analysis of femoral neck: Detection of exercise load-associated differences in trabecular bone," *Journal of Magnetic Resonance Imaging*, vol. 34, no. 6, pp. 1359 – 1366, 2011.

Herlidou, S., Rolland, Y., Bansard, J. Y., Rumeur, E. L., and de Certaines, J. D., "Comparison of automated and visual texture analysis in MRI: Characterization of normal and diseased skeletal muscle," *Magnetic Resonance Imaging*, vol. 17, no. 9, pp. 1393 – 1397, 1999.

Herlidou-Meme, S., Constans, J. M., Carsin, B., Olivie, D., Eliat, P. A., Nadal-Desbarats, L., Gondry, C., Rumeur, E. L., Idy-Peretti, I., and de Certaines, J. D., "MRI texture analysis on texture test objects, normal brain and intracranial tumors," *Magnetic Resonance Imaging*, vol. 21, no. 9, pp. 989–993, 2003.

Holli, K. K., Waljas, M., Harrison, L., Liimatainen, S., Luukkaala, T., Ryymin, P., Eskola, H., Soimakallio, S., Ohman, J., and Dastidar, P., "Mild traumatic brain injury: tissue texture analysis correlated to neuropsychological and DTI findings," *Academic Radiology*, vol. 17, no. 9, pp. 1096–1102, 2010.

Hornykiewicz, O., "Parkinson's disease: from brain homogenate to treatment," *Federation Proceedings*, vol. 32, no. 2, pp. 183–190, 1973.

Hornykiewicz, O., "Biochemical aspects of Parkinson's disease," *Neurology*, vol. 51, no. 2 Suppl 2, pp. S2–9, 1998.

Huang, X., Lee, Y. Z., McKeown, M., Gerig, G., Gu, H., Lin, W., Lewis, M. M., Ford, S., Troster, A. I., Weinberger, D. R., and Styner, M., "Asymmetrical ventricular enlargement in Parkinson's disease," *Movement Disorders*, vol. 22, no. 11, pp. 1657–1660, 2007.

Kaizer, H., "A quantification of textures on aerial photographs," Boston University Research Laboratory, Technical report, Technical note 121, 1995.

Kassner, A., Liu, F., Thornhill, R. E., Tomlinson, G., and Mikulis, D. J., "Prediction of hemorrhagic transformation in acute ischemic stroke using texture analysis of postcontrast T1-weighted MR images," *Journal of Magnetic Resonance Imaging*, vol. 30, no. 5, pp. 933–941, 2009.

Kjaer, L., Ring, P., Thomsen, C., and Henriksen, O., "Texture analysis in quantitative MR imaging tissue characterisation of normal brain and intracranial tumours at 1.5 T," *Acta Radiologica*, vol. 36, no. 2, pp. 127–135, 1995.

Ko, E. S., Kim, J. H., Lim, Y., Han, B. K., Cho, E. Y., and Nam, S. J., "Assessment of invasive breast cancer heterogeneity using whole-tumor magnetic resonance imaging texture analysis: Correlations with detailed pathological findings," *Medicine*, vol. 95, no. 3, p. e2453, 2016.

Kosta, P., Argyropoulou, M. I., Markoula, S., and Konitsiotis, S., "MRI evaluation of the basal ganglia size and iron content in patients with Parkinson's disease," *Journal of Neurology*, vol. 253, no. 1, pp. 26–32, 2006.

Kovalev, V. A., Kruggel, F., Gertz, H. J., and Cramon, D. Y. V., "Three-dimensional texture analysis of MRI brain datasets," *IEEE Transactions on Medical Imaging*, vol. 20, no. 5, pp. 424–433, 2001.

Kovalev, V. A., Kruggel, F., and von Cramon, D. Y., "Gender and age effects in structural brain asymmetry as measured by MRI texture analysis," *NeuroImage*, vol. 19, no. 3, pp. 895–905, 2003.

Kraft, K. A., Fatouros, P. P., Clarke, G. D., and Kishore, P. R., "An MRI phantom material for quantitative relaxometry," *Magnetic Resonance in Medicine*, vol. 5, no. 6, pp. 555–562, 1987.

Kuhn, M. J., Mikulis, D. J., Ayoub, D. M., Kosofsky, B. E., Davis, K. R., and Taveras, J. M., "Wallerian degeneration after cerebral infarction: evaluation with sequential MR imaging," *Radiology*, vol. 172, no. 1, pp. 179–182, 1989.

Kumar, A., Welti, D., and Ernst, R. R., "NMR Fourier zeugmatography," *Journal of Magnetic Resonance*, vol. 18, pp. 69–83, 1975.

Langenberger, H., Shimizu, Y., Windischberger, C., Grampp, S., Berg, A., Ferlitsch, K., and Moser, E., "Bone homogeneity factor: an advanced tool for the assessment of osteoporotic bone structure in high-resolution magnetic resonance images," *Investigative Radiology*, vol. 38, no. 7, pp. 467–472, 2003.

Lee, C. S., Schulzer, M., Mak, E., Hammerstad, J. P., Calne, S., and Calne, D. B., "Patterns of asymmetry do not change over the course of idiopathic parkinsonism: implications for pathogenesis," *Neurology*, vol. 45, no. 3 Pt 1, pp. 435–439, 1995.

Lees, A. J., Hardy, J., and Revesz, T., "Parkinson's disease," *Lancet*, vol. 373, no. 9680, pp. 2055–2066, 2009.

Lerski, R. A. and Schad, L. R., "The use of reticulated foam in texture test objects for magnetic resonance imaging," *Magnetic Resonance Imaging*, vol. 16, no. 9, pp. 1139–1144, 1998.

Lerski, R. A., Straughan, K., Schad, L. R., Boyce, D., Bluml, S., and Zuna, I., "MR image texture analysis - an approach to tissue characterization," *Magnetic Resonance Imaging*, vol. 11, no. 6, pp. 873–887, 1993.

Lerski, R. A., Schad, L. R., Luypaert, R., Amorison, A., Muller, R. N., Mascaro, L., Ring, P., Spisni, A., Zhu, X., and Bruno, A., "Multicentre magnetic resonance texture analysis trial using reticulated foam test objects," *Magnetic Resonance Imaging*, vol. 17, no. 7, pp. 1025–1031, 1999.

Lerski, R. A., de Certaines, J. D., Duda, D., Klonowski, W., Yang, G., Coatrieux, J. L., Azzabou, N., and Eliat, P.-A., "Application of texture analysis to muscle MRI: 2 – technical recommendations," *EPJ Nonlinear Biomedical Physics*, vol. 3, no. 1, pp. 1–20, 2015.

Lewis, M. M., Smith, A. B., Styner, M., Gu, H., Poole, R., Zhu, H., Li, Y., Barbero, X., Gouttard, S., McKeown, M. J., Mailman, R. B., and Huang, X., "Asymmetrical lateral ventricular enlargement in Parkinson's disease," *European Journal of Neurology*, vol. 16, no. 4, pp. 475–481, 2009.

Li, Z., Mao, Y., Li, H., Yu, G., Wan, H., and Li, B., "Differentiating brain metastases from different pathological types of lung cancers using texture analysis of T1 postcontrast MR," *Magnetic Resonance in Medicine*, 2015, [Epub ahead of print].

Liu, J., Mao, Y., Li, Z., Zhang, D., Zhang, Z., Hao, S., and Li, B., "Use of texture analysis based on contrast-enhanced MRI to predict treatment response to chemoradiotherapy in nasopharyngeal carcinoma," *Journal of Magnetic Resonance Imaging*, 2016, [Epub ahead of print].

Maani, R., Yang, Y. H., and Kalra, S., "Voxel-based texture analysis of the brain," *PloS one*, vol. 10, no. 3, p. e0117759, 2015.

Madsen, E. L. and Fullerton, G. D., "Prospective tissue-mimicking materials for use in NMR imaging phantoms," *Magnetic Resonance Imaging*, vol. 1, no. 3, pp. 135–141, 1982.

Mahmoud-Ghoneim, D., de Certaines, J. D., Herlidou, S., Rolland, Y., and Maniere, A., "Gender difference on magnetic resonance imaging texture analysis of human adipose tissue." *Journal of Womens Imaging*, vol. 3, no. 3, pp. 105–107, 2001.

Mahmoud-Ghoneim, D., Cherel, Y., Lemaire, L., de Certaines, J. D., and Maniere, A., "Texture analysis of magnetic resonance images of rat muscles during atrophy and regeneration," *Magnetic Resonance Imaging*, vol. 24, no. 2, pp. 167–171, 2006.

Mano, I., Goshima, H., Nambu, M., and Iio, M., "New polyvinyl alcohol gel material for MRI phantoms," *Magnetic Resonance in Medicine*, vol. 3, no. 6, pp. 921–926, 1986.

Martin, W. R., Roberts, T. E., Ye, F. Q., and Allen, P. S., "Increased basal ganglia iron in striatonigral degeneration: in vivo estimation with magnetic resonance," *The Canadian Journal of Neurological Sciences*, vol. 25, no. 1, pp. 44–47, 1998.

Martin, W. R., Wieler, M., and Gee, M., "Midbrain iron content in early Parkinson disease: a potential biomarker of disease status," *Neurology*, vol. 70, no. 16 Pt 2, pp. 1411–1417, 2008.

Materka, A. and Strzelecki, M., "On the importance of MRI nonuniformity correction for texture analysis," in *IEEE Proceedings on Signal Processing, Algorithms, Architectures, Arrangements and Applications*, 2013, pp. 118–123.

Materka, A. and Strzelecki, M., "Texture analysis method - a review, COST B11 report," 1998.

Materka, A., Strzelecki, M., and Lerski, R. A., "Feature evaluation of texture test objects for magnetic resonance imaging," in *Texture Analysis in Machine Vision, Series in Machine Perception and Artificial Intelligence*, Pietikainen, M. K., Ed. Singapore: World Scientific, 2000, pp. 197–206.

Mayerhoefer, M. E., Breitenseher, M. J., Kramer, J., Aigner, N., Hofmann, S., and Materka, A., "Texture analysis for tissue discrimination on T1-weighted MR images of the knee joint in a multicenter study: Transferability of texture features and comparison of feature selection methods and classifiers," *Journal of Magnetic Resonance Imaging*, vol. 22, no. 5, pp. 674–680, 2005.

Mayerhoefer, M. E., Szomolanyi, P., Jirak, D., Materka, A., and Trattnig, S., "Effects of MRI acquisition parameter variations and protocol heterogeneity on the results of texture analysis and pattern discrimination: an application-oriented study," *Medical Physics*, vol. 36, no. 4, pp. 1236–1243, 2009.

McKeown, M. J., Uthama, A., Abugharbieh, R., Palmer, S., Lewis, M., and Huang, X., "Shape (but not volume) changes in the thalami in Parkinson disease," *BMC Neurology*, vol. 8, pp. 8–2377–8–8, 2008.

Menke, R. A., Scholz, J., Miller, K. L., Deoni, S., Jbabdi, S., Matthews, P. M., and Zarei, M., "MRI characteristics of the substantia nigra in Parkinson's disease: a combined quantitative T1 and DTI study," *NeuroImage*, vol. 47, no. 2, pp. 435–441, 2009.

Merboldt, K. D., Hanicke, W., and Frahm, J., "Self-diffusion NMR imaging using stimulated echoes," *Journal of Magnetic Resonance*, vol. 64, pp. 479 – 486, 1985.

Mitchell, M. D., Kundel, H. L., Axel, L., and Joseph, P. M., "Agarose as a tissue equivalent phantom material for NMR imaging," *Magnetic Resonance Imaging*, vol. 4, no. 3, pp. 263 – 266, 1986.

Nakai, R., Azuma, T., Sudo, M., Urayama, S., Takizawa, O., and Tsutsumi, S., "MRI analysis of structural changes in skeletal muscles and surrounding tissues following long-term walking exercise with training equipment," *Journal of Applied Physiology*, vol. 105, no. 3, pp. 958 – 963, 2008.

Nikander, R., Kannus, P., Dastidar, P., Hannula, M., Harrison, L., Cervinka, T., Narra, N. G., Aktour, R., Arola, T., Eskola, H., Soimakallio, S., Heinonen, A., Hyttinen, J., and Sievanen, H., "Targeted exercises against hip fragility," *Osteoporosis International*, vol. 20, no. 8, pp. 1321 – 1328, 2009.

Nketiah, G., Savio, S., Dastidar, P., Nikander, R., Eskola, H., and Sievanen, H., "Detection of exercise load-associated differences in hip muscles by texture analysis," *Scandinavian Journal of Medicine and Science in Sports*, vol. 25, no. 3, pp. 428 – 434, 2015.

Obeso, J. A., Marin, C., Rodriguez-Oroz, C., Blesa, J., Benitez-Temino, B., Mena-Segovia, J., Rodriguez, M., and Olanow, C. W., "The basal ganglia in Parkinson's disease: current concepts and unexplained observations," *Annals of Neurology*, vol. 64 Suppl 2, pp. S30 – 46, 2008.

Ojala, T., Pietikainen, M., and Harwood, D., "A comparative study of texture measures with classification based on features distributions," *Pattern Recognition*, vol. 29, no. 1, pp. 51 – 59, 1996.

Piccini, P. and Brooks, D. J., "New developments of brain imaging for Parkinson's disease and related disorders," *Movement Disorders*, vol. 21, no. 12, pp. 2035 – 2041, 2006.

Pickles, M. D., Lowry, M., and Gibbs, P., "Pretreatment prognostic value of dynamic contrast-enhanced magnetic resonance imaging vascular, texture, shape, and size parameters compared with traditional survival indicators obtained from locally advanced breast cancer patients," *Investigative Radiology*, vol. 51, no. 3, pp. 177 – 185, 2016.

Purcell, E. M., Torrey, H. C., and Ound, R. V., "Resonance absorption by nuclear magnetic moments in a solid," *Physical Review*, vol. 69, p. 37, 1946.

Qian, S. and Chen, D., "Discrete Gabor transform," *IEEE Transactions on Signal Processing*, vol. 41, no. 7, pp. 2429 – 2438, 1993.

Ramirez-Ruiz, B., Marti, M. J., Tolosa, E., Bartres-Faz, D., Summerfield, C., Salgado-Pineda, P., Gomez-Anson, B., and Junque, C., "Longitudinal evaluation of cerebral morphological changes in Parkinson's disease with and without dementia," *Journal of Neurology*, vol. 252, no. 11, pp. 1345 – 1352, 2005.

Rantalainen, T., Nikander, R., Heinonen, A., Cervinka, T., Sievanen, H., and Daly, R. M., "Differential effects of exercise on tibial shaft marrow density in young female athletes," *Journal of Clinical Endocrinology and Metabolism*, vol. 98, no. 5, pp. 2037 – 2044, 2013.

Rossi, M., Ruottinen, H., Elovaara, I., Ryymin, P., Soimakallio, S., Eskola, H., and Dastidar, P., "Brain iron deposition and sequence characteristics in Parkinsonism: comparison of SWI, T(2)* maps, T(2)-weighted-, and FLAIR-SPACE," *Investigative Radiology*, vol. 45, no. 12, pp. 795–802, 2010.

Russ, J. C., *The image processing handbook*. CRC Press, 2002.

Ryvlin, P., Broussolle, E., Piollet, H., Viallet, F., Khalfallah, Y., and Chazot, G., "Magnetic resonance imaging evidence of decreased putamenal iron content in idiopathic Parkinson's disease," *Archives of Neurology*, vol. 52, no. 6, pp. 583–588, 1995.

Sikio, M., Holli, K. K., Harrison, L. C., Ruottinen, H., Rossi, M., Helminen, M. T., Ryymin, P., Paalavuo, R., Soimakallio, S., Eskola, H. J., Elovaara, I., and Dastidar, P., "Parkinson's disease: interhemispheric textural differences in MR images," *Academic Radiology*, vol. 18, no. 10, pp. 1217–1224, 2011.

Sikio, M., Holli-Helenius, K. K., Harrison, L. C., Ryymin, P., Ruottinen, H., Saunamaki, T., Eskola, H. J., Elovaara, I., and Dastidar, P., "MR image texture in Parkinson's disease: a longitudinal study," *Acta Radiologica*, vol. 56, no. 1, pp. 97–104, 2015.

Strzelecki, M. and Materka, A., "On sensitivity of texture parameters to smooth variations of local image intensity and contrast," in *IEEE Proceedings on Signal Processing, Algorithms, Architectures, Arrangements and Applications*, 22-24th September 2014 2014, pp. 48–53.

Strzelecki, M., Szczypinski, P., Materka, A., and Klepaczko, A., "A software tool for automatic classification and segmentation of 2D/3D medical images," *Nuclear Instruments and Methods in Physics Research Section A: Accelerators, Spectrometers, Detectors and Associated Equipment*, vol. 702, no. 0, pp. 137–140, 2013.

Suoranta, S., Holli-Helenius, K., Koskenkorva, P., Niskanen, E., Kononen, M., Aikia, M., Eskola, H., Kalviainen, R., and Vanninen, R., "3D texture analysis reveals imperceptible MRI textural alterations in the thalamus and putamen in progressive myoclonic epilepsy type 1, EPM1," *PloS one*, vol. 8, no. 7, p. e69905, 2013.

Szczypinski, P. M., Strzelecki, M., and Materka, A., "MaZda - a software for texture analysis," in *IEEE Proceedings of International Symposium on Information Technology Convergence*, 2007, pp. 245–249.

Szczypinski, P. M., Strzelecki, M., Materka, A., and Klepaczko, A., "Mazda—a software package for image texture analysis," *Computer Methods and Programs in Biomedicine*, vol. 94, no. 1, pp. 66–76, 2009.

Taylor, D. G. and Bushell, M. C., "The spatial mapping of translational diffusion coefficients by the NMR imaging technique," *Physics in Medicine and Biology*, vol. 30, no. 4, pp. 345–349, 1985.

Teruel, J. R., Heldahl, M. G., Goa, P. E., Pickles, M., Lundgren, S., Bathen, T. F., and Gibbs, P., "Dynamic contrast-enhanced MRI texture analysis for pretreatment prediction of clinical and pathological response to neoadjuvant chemotherapy in patients with locally advanced breast cancer," *NMR in Biomedicine*, vol. 27, no. 8, pp. 887–896, 2014.

Thomalla, G., Glauche, V., Koch, M. A., Beaulieu, C., Weiller, C., and Rother, J., "Diffusion tensor imaging detects early Wallerian degeneration of the pyramidal tract after ischemic stroke," *NeuroImage*, vol. 22, no. 4, pp. 1767 – 1774, 2004.

Tuceryan, M. and Jain, A. K., *The handbook of pattern recognition and computer vision*, 2nd ed. Singapore: World Scientific, 1998.

Vre, R. M.-D., Grimee, R., Parmentier, F., and Binet, J., "The use of agar gel as a basic reference material for calibrating relaxation times and imaging parameters," *Magnetic Resonance in Medicine*, vol. 2, no. 2, pp. 176 – 179, 1985.

Vymazal, J., Righini, A., Brooks, R. A., Canesi, M., Mariani, C., Leonardi, M., and Pezzoli, G., "T1 and T2 in the brain of healthy subjects, patients with Parkinson disease, and patients with multiple system atrophy: relation to iron content," *Radiology*, vol. 211, no. 2, pp. 489 – 495, 1999.

Waller, A. V., "Experiments on the section of the glossopharyngeal and hypoglossal nerves of the frog, and observations of the alterations produced thereby in the structure of their primitive fibres," *Philosophical Transactions of the Royal Society London B*, vol. 140, pp. 423 – 429, 1850.

Wallis, L. I., Paley, M. N., Graham, J. M., Grunewald, R. A., Wignall, E. L., Joy, H. M., and Griffiths, P. D., "MRI assessment of basal ganglia iron deposition in Parkinson's disease," *Journal of Magnetic Resonance Imaging*, vol. 28, no. 5, pp. 1061 – 1067, 2008.

Wang, L. and He, D.-C., "Texture classification using texture spectrum," *Pattern Recognition*, vol. 23, no. 8, pp. 905 – 910, 1990.

Wu, S. F., Zhu, Z. F., Kong, Y., Zhang, H. P., Zhou, G. Q., Jiang, Q. T., and Meng, X. P., "Assessment of cerebral iron content in patients with Parkinson's disease by the susceptibility-weighted MRI," *European Review for Medical and Pharmacological Sciences*, vol. 18, no. 18, pp. 2605 – 2608, 2014.

Wu, X., Sikio, M., Pertovaara, H., Jarvenpaa, R., Eskola, H., Dastidar, P., and Kellokumpu-Lehtinen, P. L., "Differentiation of diffuse large B-cell lymphoma from follicular lymphoma using texture analysis on conventional MR images at 3.0 Tesla," *Academic Radiology*, vol. 23, no. 6, pp. 696 – 703, 2016.

Yang, D., Rao, G., Martinez, J., Veeraraghavan, A., and Rao, A., "Evaluation of tumor-derived MRI-texture features for discrimination of molecular subtypes and prediction of 12-month survival status in glioblastoma," *Medical Physics*, vol. 42, no. 11, pp. 6725 – 6735, 2015.

Yoon, S. H., Park, C. M., Park, S. J., Yoon, J. H., Hahn, S., and Goo, J. M., "Tumor heterogeneity in lung cancer: Assessment with dynamic contrast-enhanced MR imaging," *Radiology*, p. 151367, 2016.

Yoshimura, K., Kato, H., Kuroda, M., Yoshida, A., Hanamoto, K., Tanaka, A., Tsunoda, M., Kanazawa, S., Shibuya, K., Kawasaki, S., and Hiraki, Y., "Development of a tissue-equivalent MRI phantom using carrageenan gel," *Magnetic Resonance in Medicine*, vol. 50, no. 5, pp. 1011 – 1017, 2003.

Youdim, M. B. and Riederer, P., "The role of iron in senescence of dopaminergic neurons in Parkinson's disease," *Journal of Neural Transmission*, vol. 40, pp. 57 – 67, 1993.

Yu, H., Buch, K., Li, B., O'Brien, M., Soto, J., Jara, H., and Anderson, S. W., "Utility of texture analysis for quantifying hepatic fibrosis on proton density MRI," *Journal of Magnetic Resonance Imaging*, vol. 42, no. 5, pp. 1259–1265, 2015.

Yu, O., Mauss, Y., Namer, I. J., and Chambron, J., "Existence of contralateral abnormalities revealed by texture analysis in unilateral intractable hippocampal epilepsy," *Magnetic Resonance Imaging*, vol. 19, no. 10, pp. 1305–1310, 2001.

Zhang, J., Zhang, Y., Wang, J., Cai, P., Luo, C., Qian, Z., Dai, Y., and Feng, H., "Characterizing iron deposition in Parkinson's disease using susceptibility-weighted imaging: an in vivo MR study," *Brain Research*, vol. 1330, pp. 124–130, 2010.

Zhang, W., Sun, S. G., Jiang, Y. H., Qiao, X., Sun, X., and Wu, Y., "Determination of brain iron content in patients with Parkinson's disease using magnetic susceptibility imaging," *Neuroscience Bulletin*, vol. 25, no. 6, pp. 353–360, 2009.

Zhang, X., Gao, X., Liu, B. J., Ma, K., Yan, W., Liling, L., Yuhong, H., and Fujita, H., "Effective staging of fibrosis by the selected texture features of liver: Which one is better, CT or MR imaging?" *Computerized Medical Imaging and Graphics*, vol. 46 Pt 2, pp. 227–236, 2015.

Original Publications

The Effect of Region of Interest Size on Textural Parameters

A study with clinical magnetic resonance images and artificial noise images

Minna Sikiö, Kirsi K Holli-Helenius, Pertti Ryymin, Prasun Dastidar, Hannu Eskola
Department of Radiology
Medical Imaging Center and Hospital Pharmacy, Tampere University Hospital
Tampere, Finland

Minna Sikiö, Lara Harrison, Hannu Eskola
Department of Electronics and Communications Engineering
Tampere University of Technology
Tampere, Finland

***Abstract*—Texture analysis provides quantitative information describing the properties of a digital image. The value of texture analysis has been tested in various medical applications, using mostly magnetic resonance images because of the amount of information the method is capable to provide. However, there exists no certain practice to define the region of interest (ROI) within the texture parameters are calculated. Many parameters seem to be dependent on the ROI size. We studied the effect of the ROI size with magnetic resonance head images from 64 healthy adults and artificial noise images. According to our results, ROI size has a significant effect on the computed value of several second-order texture features. We conclude that comparisons of different size ROIs will therefore lead to falsely optimistic classification between analyzed tissues.**

Keywords—texture analysis; region of interest; size; magnetic resonance imaging; random pattern

I. BACKGROUND

Magnetic resonance (MR) images may reveal significantly more detailed information about the underlying tissue than the human perception is capable to distinguish. Because of the vast growth of the acquired information from medical images, the development of new computer-aided systems has become increasingly important. Computer vision can, for example, be used to assist radiologists in focusing their attention on diagnostically relevant information and to provide quantitative measures for suspicious regions.

Texture analysis (TA) methods evaluate the spatial location and signal intensity characteristics of the fundamental structural elements, pixels, of images. TA allows one to calculate mathematical patterns i.e. texture features which can be used to characterize and classify the underlying properties of tissues [1].

Texture analysis exploits a numerous different methods for calculating texture parameters. Statistical approaches are widely used in TA of medical images. They analyze the spatial distribution of grey values, computing local features at each point in the image, and deriving a set of statistics from the distributions of the local features. Most commonly used features are derived from the histogram, co-occurrence matrix (COM), and run-length matrix (RLM).

TA has been successfully applied in classification of various pathological tissues from, for example, the liver [2], brain [3, 4], breast [5, 6] and tumours with variable locations such as lymphomas [7]. TA has also been applied in numerous neurological disorders and neurodegenerative diseases [8-11]. Reports of the utility of TA have been ranging from promising to good depending on the application, patient material, imaging methods and other technical factors [12-17]. There are many factors affecting the calculated texture parameters. Since it is obvious that MRI sequences, patient material and tissue under analysis affect the magnitude of texture parameters we have now concentrated on studying the factors which might affect the TA result within the same study question and material.

One essential factor in texture analysis is the region of interest (ROI) size. In the selection of image ROI, one has to balance between the need to capture appropriate textural information for classification purposes with the desire to avoid multiple tissue categories. The ROI size and shape vary greatly between different studies. Unfortunately, the ROI definition has not always been accurately specified in all reports.

The aim of our study is to determine the effect of ROI size on histogram, COM, and RLM-based texture parameters.

II. MATERIAL AND METHODS

A. Study Population

In total, 64 healthy adults (aged between 20 and 60 years, mean age 39.0 years, standard deviation 11.7 years, 27 males, 37 females) were recruited for the study. Exclusion criteria were (i) neurological problems (including abnormalities on neuroimaging), (ii) psychiatric problems, (iii) history of traumatic brain injury, (iv) former neurosurgical procedure, (v) problems with hearing or vision, (vi) first language other than Finnish, (vii) MRI contraindications, and (viii) refusal to participate. None of the subjects had significant structural abnormalities on conventional MRI sequences. The study was conducted at Tampere University Hospital.

B. Study Images

MR imaging was performed using a 3-T device (Siemens TrioTim, Erlangen, Germany) with a 12-channel head matrix coil following a clinical procedure. The sequence used in our study was axial T2-weighted 2D turbo spin echo with the following imaging parameters: repetition time 5790 ms, echo time 109 ms, slice thickness 4.0 mm with gap of 1.2 mm, matrix size 448 × 326 pixels, field of view 230 mm, and flip angle 120°. Axial slice representing the centrum semiovale area was selected from every participant. The particular location was selected because of clear anatomical landmarks and a relatively wide texturally homogeneous area.

The artificial noise image matrices were generated with Matlab (MathWorks, Natick, Massachusetts, U.S.A.) and filled with random pixel intensity values from 0 to 255 with uniform intensity distribution. The pixel size was set to match with that of the real MR images. Examples of both MR and noise images are presented in Fig. 1.

C. TA

The TA software used in the study was MaZda package version 4.6 (The Technical University of Lodz, Institute of Electronics, Lodz, Poland) [18-20]. First, ten of each circular ROIs of 5, 6, 7, 8, 9, 10, 15, 20, 25, 30, and 35 pixels in diameter were drawn into various locations of the random images. The ROI sizes correspond to ROI areas from 21 to 933 pixels. Second, the same ROIs were manually placed on the right hemisphere centrum semiovale in every MR image. The ROI setting is defined in Fig. 1a-b.

In total, four histogram-based (*mean, variance, kurtosis,* and *skewness*), 11 COM-based (*angular second moment, contrast, correlation, sum of squares, inverse difference moment, sum average, sum variance, sum entropy, entropy, difference variance,* and *difference entropy*), and five RLM-based (*run-length nonuniformity, grey-level nonuniformity, short-run emphasis moment, long-run emphasis moment,* and *fraction*) parameters were calculated for each ROI. The COM parameters were calculated with the distance of one pixel and both COM and RLM parameters were calculated in four directions (0°, 45°, 90°, and 135°) using eight bits per pixel. The four directional components of each parameter were averaged into one parameter in order to enhance the robustness of the method because the exact position of the participants during the MR imaging could not be ensured.

The grey level normalization of each ROI was performed using method which normalizes image intensities in the range $[\mu-3\sigma, \mu+3\sigma]$, where μ is the mean grey level value and σ the standard deviation, to minimize the influence of contrast variation and brightness.

III. Results

A. Histogram Parameters

An example of the behaviour of the histogram parameters can be seen in Fig. 2a where *mean* is plotted against ROI area. The value of *mean* does not alter as the ROI size increases. The behaviour of other histogram parameters is the same which means they are independent on the ROI size. However, the value range obtained from the MR images is large.

B. COM Parameters

There are three examples of COM parameters presented in Fig 2: *angular second moment* (2b), *sum of squares* (2c), and *contrast* (2d).

Entropy parameters (*entropy, sum entropy,* and *difference entropy*) otherwise follow the behaviour of *angular second moment* but their value increases along with the ROI size. After a particular ROI size the value of these parameters seems to saturate to a certain level. *Inverse difference moment* and *sum average* follow the behaviour of *sum of squares* as they all converge towards a limit. *Contrast, correlation, sum variance,* and *difference variance* are also quite independent on the ROI size but the parameter distribution among MR image textures from the centrum semiovale area appears very wide.

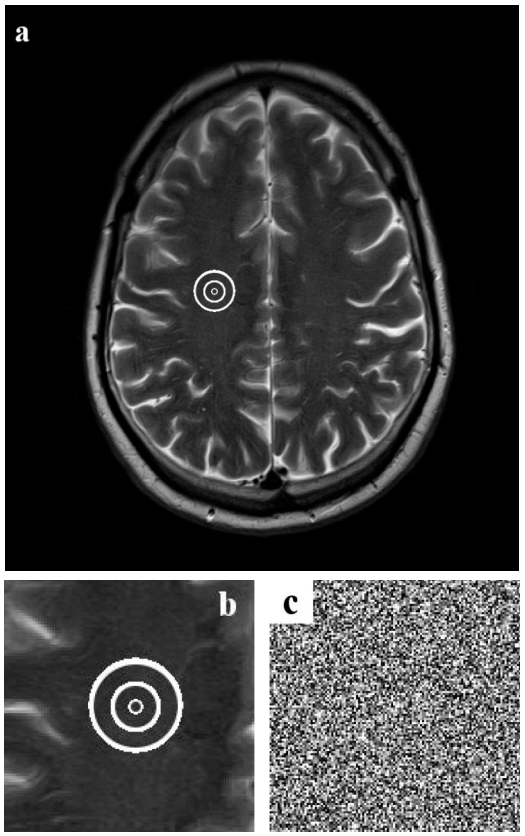

Fig. 1. Examples of a magnetic resonance image and regions of interest on the centrum semiovale (a), zoomed regions of interest of size 5, 20, and 35 pixels in diameter (b), and artificial noise image with random pattern (c).

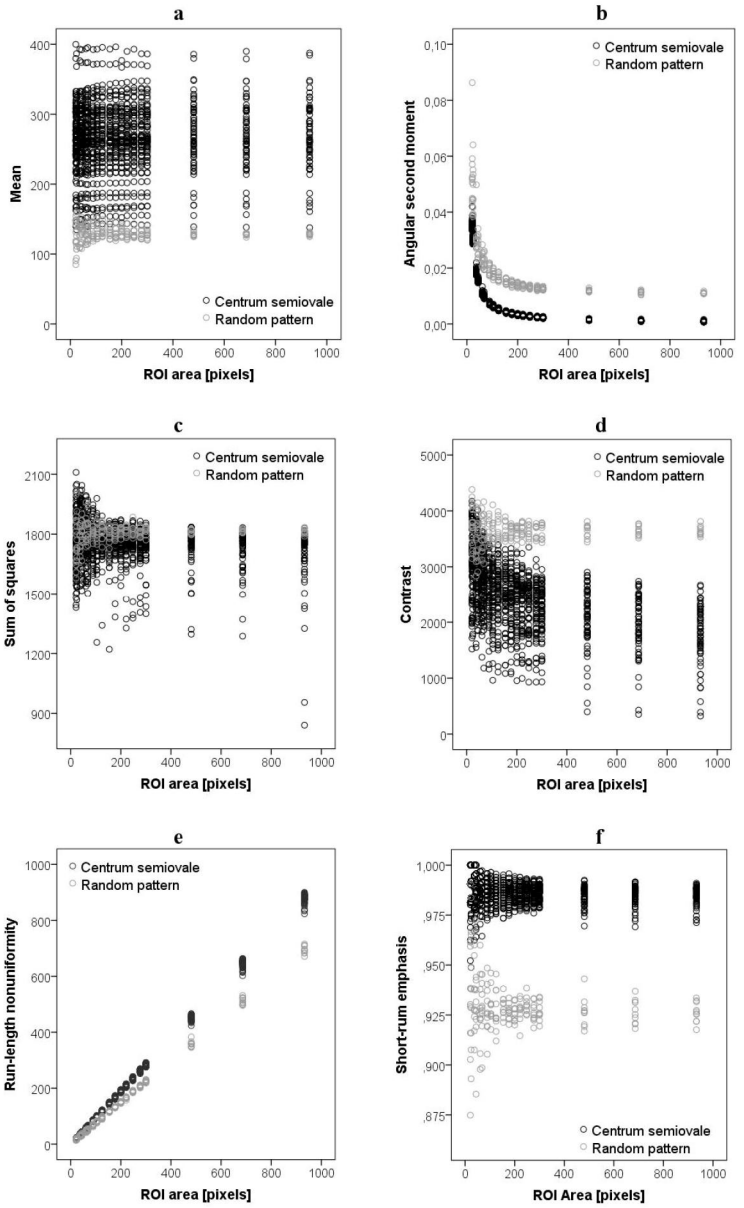

Fig. 2. Example scatter plots of histogram, co-occurrence matrix, and run-length matrix-based parameters calculated from centrum semiovale area on MR images and artificial random noise pattern within circular regions of interest of size 5, 6, 7, 8, 9, 10, 15, 20, 25, 30, and 35 pixels in diameter.

C. RLM Parameters

Fig. 2 shows the scatter plots of RLM parameters *run-length nonuniformity* (2e) and *short-run emphasis* (2f). Both *run-length nonuniformity* and *grey-level nonuniformity* increase linearly along with the ROI size. Instead, *short-sun emphasis, long-run emphasis,* and *fraction* are quite independent on the ROI size.

IV. Discussion

During the past decade TA has gained a footing in medical image analysis. Advancements on medical imaging systems have made it possible to obtain texture information which is not visible to human perception.

Even though TA has proven to be very promising tool in medical image analysis [1-17], it still has a numerous pitfalls and problems. Especially TA of MR images has numerous matters to consider before applying the method, ranging from MR image sequences and machinery configurations to the technical factors of actual textural analysis such as the ROI size and shape definition. For instance, the effect of ROI definition is not often properly addressed in TA studies. Therefore our goal in this study was to determine the effect of ROI size on histogram, COM, and RLM-based texture parameters.

Histogram parameters are calculated based on single pixel values and, therefore, their information content is quite simple and understandable. Our results show that their values are independent on the ROI size. However, they provide little additional information to visual inspection of images. Our results also demonstrate that histogram parameters are highly dependent on the image contrast and brightness variation and, therefore, a wide variation in the magnitude of histogram based texture features between the MR images was observed. The variation in histogram parameter *mean* relates to variation in sensitivity of the MR machine which is patient-specific. There can be a large intensity variation between the inspected study images which may be reduced by various normalizing methods available in MaZda software. The artificial texture made of 256 different grey scale values gives predictable histogram values: the *mean* approaches the value 128 as the ROI gets bigger.

Higher-order parameters relate to several pixels: the COM is a second-order histogram of image intensity and relates to pixel pairs. Parameters derived from the COM contain information that cannot be evaluated visually. Our results show that COM parameters behave in two different ways: they are either dependent on the ROI size and approach a certain limit or quite independent on the ROI size and converge a certain value as the ROI size increases. Parameters describing the image homogeneity and complexity (*angular second moment, entropy, sum entropy,* and *difference entropy*) are examples of parameters that depend on the ROI size, especially with small ROI sizes, and approach a limit value. There is some variation within the ROIs of the same size with smaller ROIs but with bigger ROIs the values of different samples are quite equal. In addition, the size of the ROI becomes insignificant as all samples saturate to a certain value.

As usual in signal processing, when observing textures from too small regions the variation between samples increases. This is visible also in our study, especially with the COM homogeneity and complexity parameters. In average, with ROIs smaller than 10 pixels in diameter the samples from different images perform values in wide range. In addition, with ROIs larger than approximately 15 pixels in diameter the textural information inside the ROI seems to be lost in the abundance of pixels. Neither partial volume pixels nor even whole pixels of surrounding structures, which inevitably appeared in average in ROIs larger than 20 pixels in diameter, seem to have much impact on the parameter values. This raises a question whether these COM parameters carry specific information after the saturation point. Hence, rather than using a ROI as large as possible, the ROI should be fitted according to the structure or area under inspection. In addition, when comparing COM parameters, the values should be obtained from ROIs of the same size because the ROI size has an effect on the values.

Our study show that COM parameters *sum of squares, inverse difference moment,* and *sum average* appeared quite independent on the ROI size. However, the values of *sum of squares* and *sum average* obtained from the MR images overlap with the values from the artificial random texture. These parameters might, thus, not reveal any additional information of the underlying texture in this application. *Inverse difference moment* describing the uniformity of the texture inside the ROI, instead, performed differing values from the MR image and random textures.

Overall, COM and RLM parameters are not so sensitive to the variation of intensity level between images as histogram parameters since their calculation is always based on the relationships of two image pixels, not only the insensitivity values of single pixels. However, based on our study, there are also COM parameters that are clearly more responsive to image quality aspects: *contrast, correlation, sum variance,* and *difference variance*. These parameters are more related to the intensity values of the pixels and are also vulnerable to different image intensity and noise levels. The parameter values obtained from the MR image textures vary in such a wide scale that they are most likely influenced by the image intensity variations. More uniform image normalization is needed in order to fully benefit from these parameters.

Based on our study, RLM parameters *run length nonuniformity* and *grey level nonuniformity* are linearly dependent whereas *short run emphasis, long run emphasis,* and *fraction* are independent on the ROI size. The linear behaviour of the nonuniformity parameters is due to the definition of the RLM features as the *run length nonuniformity* squares the number of grey levels for each run length and the *grey level nonuniformity* squares the number of run lengths for each grey level. Thus, for a larger ROI there will be more runs. When the functions are multiplied by the normalization factor which is inversely proportional to ROI size, instead of the texture appearance the values of the *nonuniformity* parameters are dominated by the ROI size. All RLM parameters, however, provide clearly differing values from the two different test image sets, MR images and random pattern. The range of the samples is also relatively compact and, thus, the RLM parameters seem robust and valuable in various TA studies.

In conclusion, based on our study we recommend (i) to focus on texture parameters that relate to more than one pixel or to ensure proper image normalization, (ii) to use standard ROIs of size selected according to the application, and (iii) to clearly report the ROI definition and localization in all TA studies of MR images.

ACKNOWLEDGMENT

MS was supported by grant from the Finnish Cultural Science Foundation, Ella and Georg Ehrnrooth Foundation, and Parkinson Foundation and KKHH by grant from the Jenny and Antti Wihuri Foundation.

REFERENCES

[1] G. Castellano, L. Bonilha, L.M. Li, and F. Cendes, "Texture analysis of medical images," Clin. Radiol., vol. 59, pp. 1061-1069, December 2004.

[2] D. Jirak, M. Dezortova, P. Taimr, and M. Hajek, "Texture analysis of human liver," J. Magn. Reson. Imaging, vol. 15, pp. 68-74, January 2002.

[3] L.R. Schad, S. Bluml, I. Zuna, "MR tissue characterization of intracranial tumors by means of texture analysis," Magn. Reson. Imaging, vol. 11, pp. 889-896, 1993.

[4] D. Mahmoud-Ghoneim, G. Toussaint, J.M. Constans, and J.D. de Certaines, "Three dimensional texture analysis in MRI: a preliminary evaluation in gliomas," Magn. Reson. Imaging, vol. 21, pp. 983-987, November 2003.

[5] P. Gibbs and L.W. Turnbull, "Textural analysis of contrast-enhanced MR images of the breast," Magnet. Reson. Med., vol. 50, pp.92-98, July 2003.

[6] K. Holli, A.L. Lääperi, L. Harrison, T. Luukkaala, T. Toivonen, P. Ryymin, P. Dastidar, S. Soimakallio, and H. Eskola, "Characterization of breast cancer types by texture analysis of magnetic resonance images," Acad. Radiol., vol. 17, pp. 135-141, February 2010.

[7] L.C. Harrison, T. Luukkaala, H. Pertovaara, T.O. Saarinen, T.T. Heinonen, R. Järvenpää, S. Soimakallio, P.L. Kellokumpu-Lehtinen H.J. Eskola, and P. Dastidar, "Non-Hodgkin lymphoma response evaluation with MRI texture classification," J. Exp. Clin. Cancer Res., vol. 28, p. 87, June 2009.

[8] P.A. Freeborough and N.C. Fox, "MR image texture analysis applied to the diagnosis and tracking of Alzheimer's disease," IEEE Trans. Med. Imaging, vol. 17, pp. 475-479, June 1998.

[9] L. Bonilha, E. Kobayashi, G. Castellano, G. Coelho, E. Tinois, F. Cendes, and L.M. Li, "Texture analysis of hippocampal sclerosis," Epilepsia, vol. 44, pp. 1546-1550, December 2003.

[10] L.C. Harrison, M. Raunio, K.K. Holli, T. Luukkaala, S. Savio, I. Elovaara, S. Soimakallio, H.J. Eskola, and P. Dastidar, "MRI texture analysis in multiple sclerosis: toward a clinical analysis protocol," Acad. Radiol., vol. 17, pp. 696-707, June 2010.

[11] M. Sikiö, K.K. Holli-Helenius, L.C. Harrison, P. Ryymin, H. Ruottinen, T. Saunamäki, H.J. Eskola, I. Elovaara, and P. Dastidar, "MR image texture in Parkinson's disease: a longitudinal study," Acta Radiol. Vol. 56, pp. 97-104, January 2015.

[12] G. Blumenkrantz, R. Stahl, J. Carballido-Gamio, S. Zhao, Y. Lu, T. Munoz, M.P. Hellio Le Graverand-Gastineau, S.K. Jain, T.M. Link, and S. Majumdar, "The feasability of characterizing the spatial distribution of cartilage T(2) using texture analysis," Osteoarthritis Cartilage, vol. 16, pp. 584-590, May 2008.

[13] M.F. Mayerhoefer, W. Schima, S. Trattnig, K. Pinker, V. Berger-Kulemann, and A. Ba-Ssalamah, "Texture-based classification of focal liver lesions on MRI at 3.0 Tesla: a feasability study in cysts and hemangiomas," J Magn. Reson. Imaging, vol. 32, pp. 352-359, August 2010.

[14] J. Marques, R. Granlund, M. Lillholm, P.C. Pettersen, E.B. Dam, "Automatic analysis of trabecular bone structure from knee MRI," Comput. Biol. Med., vol. 42, pp. 735-742, July 2012.

[15] P. Kölhi, J. Järnstedt, M. Sikiö, P. Dastidar, T. Peltomäki, and H. Eskola, "A texture analysis method for MR images of airway dilator muscles: a feasability study," Dentomaxillofac. Radiol., vol. 43, 2014.

[16] Y. Zhang, L.M. Metz, J.N. Scott, J. Trufyn, G.H. Fick, and F. Costello, "MRI texture heterogeneity in the opstic nerve predicts visual recovery after acute optic neuritis," Neuroimage Clin., vol. 4, pp. 302-307, January 2014.

[17] M. Sikiö, L.C. Harrison, R. Nikander, P. Ryymin, P. Dastidar, H.J. Eskola, and H. Sievänen, "Influence of exercise loading on magnetic resonance image texture of thigh sift tissues," Clin. Physiol. Funct. Imaging, vol. 34, pp. 370-376, September 2014.

[18] P. Szczypinski, M. Strzelecki, and A. Materka, "MaZda – a software for texture analysis," Proc. of ISITC 2007, pp. 245-249, Republic of Korea, November 23-23, 2007.

[19] P. Szczypinski, M. Strzelecki, A Materka, and A. Klepaczko, "MaZda – a software package for image texture analysis," Comput. Meth. Prog. Bio., vol. 94, pp. 66-76, April 2009.

[20] M. Strzelecki, P. Szczypinski, A. Materka, and A. Klepaczko, "A software tool for automatic classification and segmentation of 2D/3D medical images," Nucl. Instrum. Meth. A, vol. 702, pp. 137-140, February 2013.

Parkinson's Disease:

Interhemispheric Textural Differences in MR Images

Minna Sikiö, MSc, Kirsi K. Holli, MSc, Lara C. V. Harrison, MSc, MD, Hanna Ruottinen, MD, PhD, Maija Rossi, MSc, Mika T. Helminen, MSc, Pertti Ryymin, PhLic, Raija Paalavuo, BHc, Seppo Soimakallio, MD, PhD, Hannu J. Eskola, PhD, Irina Elovaara, MD, PhD, Prasun Dastidar, MD, PhD

Rationale and Objectives: Early-stage diagnosis of Parkinson's disease (PD) is essential in making decisions related to treatment and prognosis. However, there is no specific diagnostic test for the diagnosis of PD. The aim of this study was to evaluate the role of texture analysis (TA) of magnetic resonance images in detecting subtle changes between the hemispheres in various brain structures in patients with early symptoms of parkinsonism. In addition, functional TA parameters for detecting textural changes are presented.

Materials and Methods: Fifty-one patients with symptoms of PD and 20 healthy controls were imaged using a 3-T magnetic resonance device. Co-occurrence matrix–based TA was applied to detect changes in textures between the hemispheres in the following clinically interesting areas: dentate nucleus, basilar pons, substantia nigra, globus pallidus, thalamus, putamen, caudate nucleus, corona radiata, and centrum semiovale. The TA results were statistically evaluated using the Mann-Whitney *U* test.

Results: The results showed interhemispheric textural differences among the patients, especially in the area of basilar pons and midbrain. Concentrating on this clinically interesting area, the four most discriminant parameters were defined: co-occurrence matrix correlation, contrast, difference variance, and sum variance. With these parameters, differences were also detected in the dentate nucleus, globus pallidus, and corona radiata.

Conclusions: On the basis of this study, interhemispheric differences in the magnetic resonance images of patients with PD can be identified by the means of co-occurrence matrix–based TA. The detected areas correlate with the current pathophysiologic and neuroanatomic knowledge of PD.

Key Words: Texture analysis; Parkinson's disease; co-occurrence matrix.

Parkinson's disease (PD) is a progressive disorder of the central nervous system. Signs of PD include rest tremor, bradykinesia, rigidity, and the loss of postural reflexes (1). There is no specific diagnostic test for PD, and therefore the disease is diagnosed on the basis of clinical symptoms. Early-stage diagnosis of PD or other degenerative causes of parkinsonism is essential for deciding on treatment and prognosis, but early-stage disease may be difficult to recognize because it usually begins subtly. In addition, diagnosis is complicated because symptoms of other neurologic conditions resemble those of PD.

Acad Radiol 2011; 18:1217–1224

From the Medical Imaging Center (M.S., K.K.H., M.R., P.R., S.S., H.J.E., P.D.) and the Department of Neurology and Rehabilitation (H.R., I.E.), Teiskontie 35, PO Box 2000, Tampere University Hospital, FIN-33521 Tampere, Finland; the Department of Biomedical Engineering, Tampere University of Technology, Tampere, Finland (M.S., K.K.H., L.C.V.H., M.R., H.J.E.); Tampere Medical School (L.C.V.H., R.P., S.S., I.E., P.D.) and the Tampere School of Public Health (M.T.H.), University of Tampere, Tampere, Finland; and the Science Center, Pirkanmaa Hospital District, Tampere, Finland (M.T.H.). Received February 17, 2011; accepted June 21, 2011. This research was supported by grants from City of Tampere, the Pirkanmaa Regional Fund of the Finnish Cultural Science Foundation, and the Finnish Foundation for Technology Promotion. **Address correspondence to:** M.S. e-mail: minna.sikio@iki.fi

doi:10.1016/j.acra.2011.06.007

Among other symptoms, PD is characterized pathophysiologically by the loss of dopaminergic neurons in the substantia nigra (SN) pars compacta (2,3). The structure participates in controlling voluntary movements, and when information transfer is disturbed by the loss of neurotransmitter dopamine, the consequences can be seen as symptoms of PD (1). The identification of the midbrain dopaminergic regions is useful for evaluating the structural changes associated with PD (4).

Significant iron accumulation in the area of SN has been shown in several studies (5–15). However, few changes are visible on magnetic resonance (MR) imaging (MRI), except for narrowed SN pars compacta (5,16). Increased iron levels may also be present in caudate nucleus (14). Results from the iron deposition studies concerning the putamen and globus pallidus are conflicting, as controversies exist over increased (14,15,17,18), decreased (13,19), and unchanged (8,9) iron levels. Increased deposition of iron leads to the generation of reactive oxygen, which plays a major role in cellular damage and ultimate cellular death (10).

Some neuroimaging technologies, for example, diffusion-weighted MRI and heavily T2-weighted MRI, have produced promising results in revealing structural changes in the brain (20,21). There is still a need, however, for a method that is capable of identifying tissue changes that

are not apparent on MR images with visual inspection. Moreover, both the iron deposition changes and symptoms of PD are typically asymmetric (21). Asymmetric changes have previously been associated, for example, with lateral ventricles (22,23). On the basis of earlier studies, we assume that asymmetric changes caused by PD may be also present in other clinically significant regions of the brain.

In this study, texture analysis (TA) was applied to detect interhemispheric differences in various brain structures. Textures are features of images, surfaces, and volumes. TA is used to quantify the spatial distribution and intensity of gray levels in an image. Medical applications of TA enable, for example, the classification and analysis of tissue properties and physiologic and pathologic stages. This quantitative image analysis method has shown successful results when studying other neurologic diseases (24–28), brain tumors (29–32), liver disease (33), breast cancer (34,35), and lymphomas (36). To the best of our knowledge, there are no published results concerning the use of TA in PD available at present.

The aim of this novel study was to evaluate the role of TA in detecting subtle changes in brain structures in early-stage PD. First, differences in TA results between hemispheres were evaluated. Second, we concentrated on the clinically interesting midbrain area, and we present functional TA parameters for detecting changes in these areas. Finally, we compared our TA results between patients and healthy controls. The TA method used in this study is based on the co-occurrence matrix (COM). The co-occurrence method, first introduced by Haralick (37), has shown promising results (25,38) and also performs well for the small regions present in this study.

MATERIALS AND METHODS

Patients and Controls

The study was conducted at Tampere University Hospital. In total, 51 patients (age range, 40–86 years; mean age, 67.8 ± 11.3 years; 25 men, 26 women) with symptoms of PD were recruited. Patients who had two or more of the following symptoms were included in the study: resting tremor, bradykinesia or hypokinesia, rigidity, or postural instability. The exclusion criteria were Alzheimer's disease or other dementia diagnosed 1 year preceding the study; several general illnesses such as cardiac, lung, or gastrointestinal disease, liver or kidney malfunction, active malignant neoplasm, and neurologic or psychiatric disease; contraindications to MRI; alcohol or drug addiction; and gravidity. All participants gave written consent for the study, which was approved by the hospital ethics committee.

The control group comprised 20 healthy volunteers (age range, 58–80 years; mean age, 65.7 ± 6.8 years; four men, 16 women) with no earlier diagnoses of neurologic diseases.

MRI

Imaging was performed using a 3-T MRI device (Siemens TrioTim; Siemens Medical Systems, Erlangen, Germany) with a 12-channel head matrix coil following a clinical procedure. The imaged sequences used in the analyses and imaging parameters for these sequences are presented in Table 1.

Image Selection

Images used in the study were from axial three-dimensional susceptibility-weighted imaging (SWI) and T2-weighted three-dimensional sampling perfection with application-optimized contrasts using different flip-angle evolutions (SPACE) series. Example slices from both sequences can be seen in Figure 1. For TA, seven axial slices were selected from every patient and healthy control. Image levels were chosen to represent the clinically significant regions of the brain in PD. Image selection was performed with the Digital Imaging and Communications in Medicine viewer Osiris version 4.19 for Windows (The Digital Imaging Unit of the Service for Medical Computing of the Radiology Department of the University Hospital of Geneva, Geneva, Switzerland).

Region of Interest (ROI) Localization

ROIs were manually placed on the dentate nucleus, basilar pons, SN pars reticulata, SN pars compacta, red nucleus, globus pallidus, putamen, anterior and posterior thalamus, caudate nucleus, anterior and posterior corona radiata, and anterior, medial, and posterior centrum semiovale on both hemispheres. Anatomic levels and ROIs placed on different image levels can be seen in Figure 2. The ROIs are specified in Table 2. The ROIs were circular and 5 × 5 pixels (SN pars compacta and corona radiata), 8 × 8 pixels (dentate nucleus, SN pars reticulata, and red nucleus), 10 × 10 pixels (putamen, globus pallidus, thalamus, caudate nucleus, and centrum semiovale), and 15 × 15 pixels (basilar pons) in size. ROI localization was performed by an operator (M.S.) under the supervision of an experienced radiologist (P.D.).

TA

TA for the Digital Imaging and Communications in Medicine images was performed with MaZda version 4.6 (39). In this study, only the COM-based parameters were considered. The 11 COM parameters calculated for all ROIs were as follows: angular second moment, contrast, correlation, difference entropy, difference variance, entropy, inverse difference moment, sum average, sum entropy, sum of squares, and sum variance. In MaZda, the pixel distances $d = 1, 2, 3, 4$, and 5 and directions $\theta = 0°, 45°, 90°$, and 135° are considered. In this study, we treated parameters calculated in horizontal (0°) and vertical (90°) directions as one group and parameters calculated in diagonal directions (45° and 135°) as another group.

To minimize the influence of contrast variation and brightness, the images were normalized using a method that normalizes the image gray levels between $[\mu - 3\sigma, \mu + 3\sigma]$, where μ is the mean gray level and σ is the standard deviation.

TABLE 1. MRI Sequences and Imaging Parameters for Patients and Controls at 3 T

Sequence	TR (ms)	TE (ms)	TI (ms)	Slice Thickness (mm)/ Slice Gap (mm)	Matrix Size (Pixels)	FOV (mm)	Flip Angle (°)
Axial T2-weighted SPACE	3200	354	—	3.0/0	384 × 290	230	120
Axial 3D SWI	27	20	—	1.5/0	256 × 128	230	15

FOV, field of view; MRI, magnetic resonance imaging; SPACE, sampling perfection with application-optimized contrasts using different flip-angle evolutions; SWI, susceptibility-weighted imaging; TE, echo time; TI, inversion time; TR, repetition time.

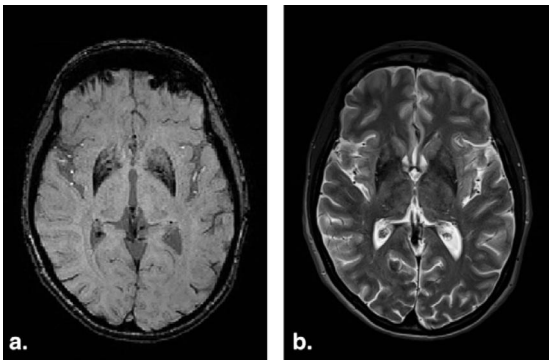

Figure 1. Difference between susceptibility-weighted imaging (SWI) and sampling perfection with application-optimized contrasts using different flip-angle evolutions (SPACE) sequences. Example slices from **(a)** three-dimensional SWI and **(b)** T2-weighted three-dimensional SPACE series.

Among different normalization methods, this method has been shown to produce the best results in MRI TA tasks (40).

Statistical Analysis

Statistical analyses were run for texture features using SPSS for Windows version 14.0.2 (SPSS, Inc, Chicago, IL). Because ROI size varied from 5 × 5 to 15 × 15 pixels depending on the structure examined, reliable distances for parameter calculation were defined for all ROI sizes. For ROIs at sizes of 5 × 5 pixels, parameters calculated in horizontal and vertical directions with pixel distances $d = 1$ and 2 and parameters calculated in diagonal directions with pixel distance $d = 1$ were considered reliable. For ROIs at sizes of 8 × 8 pixels, all parameters in horizontal and vertical directions and parameters with pixel distance $d = 1$, 2, and 3 in diagonal directions were included. For ROIs at sizes of 10 × 10 and 15 × 15 pixels, all features were analyzed. Differences in texture parameters between hemispheres in all structures were analyzed using the Mann-Whitney U test. P values < .01 were considered statistically significant.

RESULTS

Textural Differences Between Hemispheres Using All COM Parameters

First, all COM-based texture parameters were tested to find out if there were differences between the hemispheres in the selected structures. We searched for regions with significant differences in texture parameters. The analyzed structures, the number of tested parameters, and a symbol describing the relation of significant P values ($P < .01$) to all tested parameters for patients are presented in Table 3. The parameters were examined in two groups: parameters calculated in horizontal and vertical directions (0° and 90°) and parameters calculated in diagonal directions (45° and 135°). The results are presented with a threshold value of 40%. With this value, we were able to differentiate the structures with a large and little amount of significant parameters. Concurrently, we could eliminate the structures with incidental differences.

In horizontal and vertical directions, no area with ≥40% of significant P values was found. With parameters calculated in diagonal directions, one common area, the SN pars compacta, was found from both sequences. In addition, in SPACE images, the basilar pons and caudate nucleus and in SWI, the thalamus anterior showed >40% of significant P values among all P values calculated from the parameters. In healthy controls, one area, the caudate nucleus, met this requirement, with parameters calculated in diagonal directions in SPACE images.

TA Results From Clinically Significant Areas in Patient Images

Second, we considered the most interesting areas in PD (the SN and midbrain) and searched for functional parameters in finding interhemispheric differences in these areas among patients. We examined all COM-based parameters separately to find out if there were major differences in the discrimination capacity between the parameters. Again, most of the significant differences were found in the diagonal directions. Therefore, only the diagonal directions were considered in this analysis. Among all COM parameters, four parameters were distinguished: correlation, contrast, difference variance, and sum variance. Analysis results with these parameters for patients are shown in Table 4. The analyzed areas, number of tested parameters, and a symbol describing the relation of significant P values ($P < 0.01$) to all tested parameters are presented.

Using the SPACE sequence, all four parameters showed significant differences between the hemispheres in the areas of basilar pons, SN pars compacta, thalamus anterior, and caudate nucleus. In addition, three of the four parameters had >40% significant P values in the dentate nucleus and

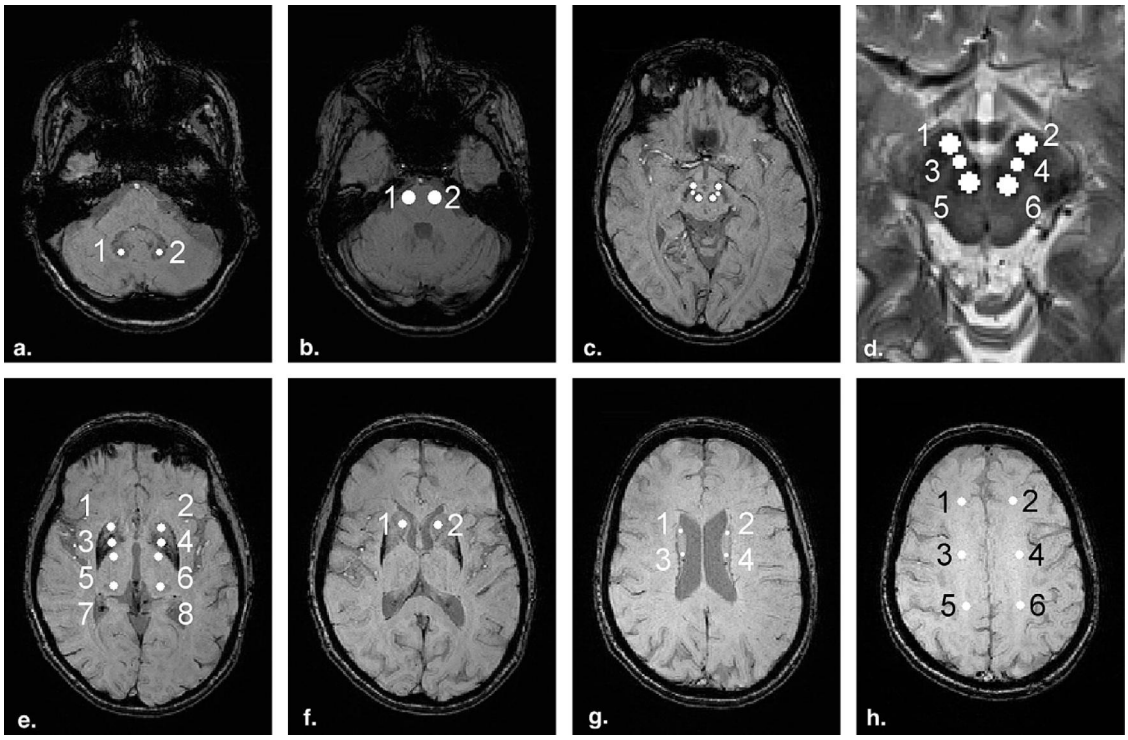

Figure 2. Image levels and regions of interest (ROIs). Specific ROI definitions can be found in Table 2. **(a)** Level 1, dentate nucleus; **(b)** level 2, basilar pons; **(c)** level 3, substantia nigra; **(d)** magnification of level 3; **(e)** level 4, putamen, globus pallidus, thalamus anterior and posterior; **(f)** level 5, caudate nucleus; **(g)** level 6, corona radiata; **(h)** level 7, centrum semiovale.

TABLE 2. Image Levels and ROIs

Level	ROI 1	ROI 2	ROI 3	ROI 4	ROI 5	ROI 6	ROI 7	ROI 8
Axial 1	Dentate nucleus dex	Dentate nucleus sin						
Axial 2	Basilar pons dex	Basilar pons sin						
Axial 3	SN pars reticulata dex	SN pars reticulata sin	SN pars compacta dex	SN pars compacta sin	Red nucleus dex	Red nucleus sin		
Axial 4	Putamen dex	Putamen sin	Globus pallidus dex	Globus pallidus sin	Thalamus ant dex	Thalamus ant sin	Thalamus post dex	Thalamus post sin
Axial 5	Caudate nucleus dex	Caudate nucleus sin						
Axial 6	Corona radiata ant dex	Corona radiata ant sin	Corona radiata post dex	Corona radiata post sin				
Axial 7	Centrum semiovale ant dex	Centrum semiovale ant sin	Centrum semiovale med dex	Centrum semiovale med sin	Centrum semiovale post dex	Centrum semiovale post sin		

Ant, anterior; dex, dexter; post, posterior; ROI, region of interest; sin, sinister; SN, substantia nigra.

globus pallidus and two of the four in the SN pars reticulata.

When using the SWI sequence, >40% significant differences between the hemispheres with all four parameters were found in the SN pars reticulata, thalamus anterior, and corona radiata posterior. Three of the four parameters qualified the terms in the areas of the SN pars compacta and red nucleus and two of the four in the basilar pons.

TABLE 3. Occurrence of Significant P Values (P < .01) When Comparing Tissues Between Hemispheres Using COM Parameters Calculated in Different Directions Among Patients (n = 51)

	SPACE				SWI			
	Horizontal and Vertical		Diagonals		Horizontal and Vertical		Diagonals	
Structure	*n*	Occurrence of Significant *P* Values	*n*	Occurrence of Significant *P* Values	*n*	Occurrence of Significant *P* Values	*n*	Occurrence of Significant *P* Values
Dentate nucleus	110	○	66	○	110	○	66	○
Basilar pons	110	○	110	●	110	○	110	○
SN pars reticulata	44	○	66	○	110	○	66	○
SN pars compacta	110	○	22	●	44	○	22	●
Red nucleus	110	○	66	○	110	○	66	○
Putamen	110	○	110	○	110	○	110	○
Globus pallidus	110	○	110	○	110	○	110	○
Thalamus ant	110	○	110	○	110	○	110	●
Thalamus post	110	○	110	○	110	○	110	○
Caudate nucleus	110	○	110	●	110	○	110	○
Corona radiata ant	44	○	22	○	44	○	22	○
Corona radiata post	44	○	22	○	44	○	22	○
Centrum semiovale ant	110	○	110	○	110	○	110	○
Centrum semiovale med	110	○	110	○	110	○	110	○
Centrum semiovale post	110	○	110	○	110	○	110	○

In structures marked with black circles (●), ≥40% of the evaluated parameters had *P* values < .01. White circles (○) indicate that <40% of the parameters showed significant changes in the region.

Ant, anterior; co-occurrence matrix; *n*, number of analyzed texture parameters; post, posterior; SN, substantia nigra; SPACE, sampling perfection with application-optimized contrasts using different flip-angle evolutions; SWI, susceptibility-weighted imaging.

TA Results From the Control Group Using the Four Most Discriminative Parameters

We analyzed the control group with the same parameters that proved discriminative among patients. The results are shown in Table 5. The analyzed areas, number of tested parameters, and a symbol describing the relation of significant *P* values ($P < .01$) to all tested parameters are presented. Again, only diagonal directions were considered because no significant changes were detected in other directions.

In the control group, >40% of *P* values were significant in the areas of the basilar pons, SN pars compacta, and caudate nucleus with all four parameters when analyzing SPACE images. COM correlation and sum variance showed significant differences also in the corona radiata posterior and COM contrast in the dentate nucleus. In susceptibility-weighted images, >40% of all *P* values were found significant in the SN pars compacta with all four parameters and in thalamus anterior with three parameters. In addition, COM contrast showed differences in SN pars compacta and thalamus posterior.

DISCUSSION

Patients with symptoms of PD underwent MRI studies, and clinically interesting areas of the brain were analyzed from the images by means of TA. As a quantitative image analysis method, TA may provide additional information to the visual inspection of the MR images. The textures of MR images contain a large amount of microscopic information concerning tissue properties and changes in them. We detected textural differences between hemispheres in areas specific to PD and evaluated functional parameters in finding these changes.

TA has been proved to extract valuable information from MR images of the brain. Previous studies have considered Alzheimer's disease (26), brain tumors (29,30), multiple sclerosis (24,28,41), brain infarctions (42), and brain injuries (43,44). Our research group has also successfully applied TA in breast cancer (34) and lymphoma (36) studies.

PD associated with pathophysiologic notifications and complementary tissue characteristics such as volume atrophy, iron deposition, and microstructural damage can be analyzed on MRI using segmentation, volumetry, SWI or gradient-echo sequences, and diffusion tensor imaging (DTI). The combination of these three markers is sufficient to discriminate between patients with PD from controls (45), and different MR biomarkers create a new perspective with which to investigate pathologic changes, disease progression, and the long-term impact of anti-PD medications.

In our study, the COM-based changes in the texture parameters of various brain structures between hemispheres in patients with symptoms of PD and healthy controls were evaluated. On the basis of our analyses with all COM parameters, significant changes between hemispheres were detected in the basilar pons, SN pars compacta, and caudate nucleus by means

TABLE 4. Occurrence of Significant P Values (P < .01) When Comparing Tissues Between Hemispheres Using Selected COM Parameters Calculated in Diagonal Directions Among Patients (n = 51)

		SPACE				SWI			
		Occurrence of Significant *P* Values							
Structure	*n*	Correlation	Contrast	Difference Variance	Sum Variance	Correlation	Contrast	Difference Variance	Sum Variance
Dentate nucleus	6	●	●	●	○	○	○	○	○
Basilar pons	10	●	●	●	●	○	●	●	○
SN pars reticulata	6	●	●	○	○	●	●	●	●
SN pars compacta	2	●	●	●	●	●	○	●	●
Red nucleus	6	○	○	○	○	●	●	○	●
Putamen	10	○	○	○	○	○	○	○	○
Globus pallidus	10	●	●	○	●	○	○	○	○
Thalamus ant	10	●	●	●	●	●	●	●	●
Thalamus post	10	○	○	○	○	○	○	○	○
Caudate nucleus	10	●	●	●	●	○	○	○	○
Corona radiata ant	2	○	○	○	○	○	○	○	○
Corona radiata post	2	○	○	○	○	●	●	●	●
Centrum semiovale ant	10	○	○	○	○	○	○	○	○
Centrum semiovale med	10	○	○	○	○	○	○	○	○
Centrum semiovale post	10	○	○	○	○	○	○	○	○

In structures marked with black circles (●), ≥40% of the evaluated parameters had *P* values < .01. White circles (○) indicate that <40% of the parameters showed significant changes in the region.

Ant, anterior; co-occurrence matrix; *n*, number of analyzed texture parameters; post, posterior; SN, substantia nigra; SPACE, sampling perfection with application-optimized contrasts using different flip-angle evolutions; SWI, susceptibility-weighted imaging.

TABLE 5. Occurrence of Significant P Values (P < .01) When Comparing Tissues Between Hemispheres Using Selected COM Parameters Calculated in Diagonal Directions Among Healthy Controls (n = 20)

		SPACE				SWI			
		Occurrence of Significant *P* Values							
Structure	*n*	Correlation	Contrast	Difference Variance	Sum Variance	Correlation	Contrast	Difference Variance	Sum Variance
Dentate nucleus	6	○	●	○	○	○	○	○	○
Basilar pons	10	●	●	●	●	○	○	○	○
SN pars reticulata	6	○	○	○	○	○	●	○	○
SN pars compacta	2	●	●	●	●	●	●	●	●
Red nucleus	6	○	○	○	○	○	○	○	○
Putamen	10	○	○	○	○	○	○	○	○
Globus pallidus	10	○	○	○	○	○	○	○	○
Thalamus ant	10	○	○	○	○	●	●	●	○
Thalamus post	10	○	○	○	○	○	●	○	○
Caudate nucleus	10	●	●	●	●	○	○	○	○
Corona radiata ant	2	○	○	○	○	○	○	○	○
Corona radiata post	2	●	○	○	●	○	○	○	○
Centrum semiovale ant	10	○	○	○	○	○	○	○	○
Centrum semiovale med	10	○	○	○	○	○	○	○	○
Centrum semiovale post	10	○	○	○	○	○	○	○	○

In structures marked with black circles (●), ≥40% of the evaluated parameters had *P* values < .01. White circles (○) indicate that <40% of the parameters showed significant changes in the region.

Ant, anterior; co-occurrence matrix; *n*, number of analyzed texture parameters; post, posterior; SN, substantia nigra; SPACE, sampling perfection with application-optimized contrasts using different flip-angle evolutions; SWI, susceptibility-weighted imaging.

of TA in patient images using the 3D SPACE sequence. In susceptibility-weighted images of patients, most changes were found in the SN pars compacta and thalamus anterior. Interestingly, the only noticeable differences were in diagonal parameter calculation directions. The direction dependence may originate from the directions of the brain tracts visible on DTI.

Only one area, the caudate nucleus, in SPACE images met our criteria of significant differences in brain textures between hemispheres in the control group with all COM parameters. This encourages us to believe that the detected interhemispheric differences among patients might be due to PD.

When using the four most discriminative COM parameters calculated in diagonal directions, some additional areas to those found with all parameters were detected in patient images. The basilar pons, SN pars reticulata, SN pars compacta, and thalamus anterior were common structures for both sequences. In SPACE images, also the dentate nucleus, globus pallidus, and caudate nucleus had >40% of significant differences between the hemispheres. Areas detected only on SWI were the red nucleus and corona radiata posterior.

Areas with the most detectable differences are in line with earlier studies concerning iron deposition transitions, as textural tissue differences were found in the SN (5–15), globus pallidus (10,13,15,17), and caudate nucleus (14). Moreover, the thalamus has also been associated with PD by changes in neuronal firing rates (46,47). The detected areas also represent the structures that are involved in the pathophysiology of PD (48).

Unlike with the analysis using all COM parameters, when considering the four most discriminative ones, changes were also detectable among the control group. Most of the significant differences between the hemispheres were found in the area of the SN pars compacta. These differences may originate from dopaminergic neuronal loss that is also seen in normal aging. However, the loss is less severe and concerns different subpopulations of neurons than in PD (49,50).

The most differing areas between patients and controls proved to be the globus pallidus and thalamus anterior in SPACE image series and the SN pars reticulata, red nucleus, and corona radiata in susceptibility-weighted images. The difference between the two sequences in the differentiation of various anatomic structures is based on the property of the sequence in detecting the mineral deposition in the gray matter areas. On T2 SPACE sequences, as previously mentioned in the literature, the differentiation between the white and gray matter areas is the most optimal of all sequences. Therefore, the above-mentioned structures are well delineated on T2 SPACE sequences. The property of the SWI sequence in differentiating the iron or mineral deposition in various gray matter structures is the reason the SN pars compacta and red nucleus are best differentiated with SWI. These structures also represent the areas where the maximal deposition of iron or mineral occurs in PD.

The limitations of our study were the relatively small study group and the fact that symptoms of PD may originate from various neurologic stages. However, we detected considerably more interhemispheric differences in the patient group than among the healthy controls. Therefore, it can be assumed that most of the texture changes detected between the hemispheres are caused by PD.

Future studies at 7 T, in which optimized SWI data are combined with gradient-echo sequences, may provide further improvements in accurately delineating these dopaminergic regions in the midbrain (4). The next step in our project is to compare our TA results with clinical information, DTI, and volumetry results and conduct a 2-year follow-up for all patients.

CONCLUSIONS

On the basis of our study, interhemispheric differences in the MR images of patients with PD can be found by means of COM-based TA. Textural differences appear in clinically significant structures, the dentate nucleus, basilar pons, SN, globus pallidus, thalamus, caudate nucleus, and corona radiata. Among these areas, only the caudate nucleus met our criteria for significant differences among healthy controls when analyzed with all COM parameters.

We also defined the four most discriminative textural features in detecting changes in the midbrain area. When using the parameters COM correlation, contrast, sum variance, and difference variance, differences were also present in the control group, most in the basilar pons, SN pars compacta, and caudate nucleus. On the basis of our results, there are more areas with interhemispheric differences in the brains of patients with PD than in the brains of healthy controls. The areas with several significant differences follow the brain tracks vulnerable to PD (5–15,17).

Our findings on TA are similar to those of earlier studies on volumetry, iron deposition analyses, and DTI analyses. Our forthcoming studies include comparison of TA to the above-mentioned modalities. In future, there is a possibility that TA characterization of PD will act as an additional complementary examination to access the progression of the disease.

REFERENCES

1. Lees AJ, Hardy J, Revesz T. Parkinson's disease. Lancet 2009; 373: 2055–2066.
2. Hornykiewicz O. Parkinson's disease: from brain homogenate to treatment. Fed Proc 1973; 32:183–190.
3. Hornykiewicz O. Biochemical aspects of Parkinson's disease. Neurology 1998; 51(suppl):S2–S9.
4. Eapen M, Zald DH, Gatenby JC, et al. Using high-resolution MR imaging at 7T to evaluate the anatomy of the midbrain dopaminergic system. AJNR Am J Neuroradiol 2010; 32:688–694.
5. Graham JM, Paley MNJ, Grünewald RA, et al. Brain iron deposition in Parkinson's disease imaged using the PRIME magnetic resonance sequence. Brain 2000; 123:2423–2431.
6. Brar S, Henderson D, Schenck J, et al. Iron accumulation in the substantia nigra of patients with Alzheimer disease and parkinsonism. Arch Neurol 2009; 66:371–374.
7. Vymazal J, Righini A, Brooks RA, et al. T1 and T2 in the brain of healthy subjects, patients with Parkinson disease, and patients with multiple system atrophy: relation to iron content. Radiology 1999; 211:489–495.
8. Zhang J, Zhang Y, Wang J, et al. Characterizing iron deposition in Parkinson's disease using susceptibility-weighted imaging: an in vivo MR study. Brain Res 2010; 1330:124–130.
9. Martin WR, Wieler M, Gee M. Midbrain iron content in early Parkinson disease: A potential biomarker of disease status. Neurology 2008; 70: 1411–1417.
10. Dexter DT, Carayon A, Javoy-Agid F, et al. Alterations in the levels of iron, ferritin and other trace metals in Parkinson's disease and other neurodegenerative diseases affecting the basal ganglia. Brain 1991; 114: 1953–1975.

11. Wallis LI, Paley MNJ, Graham JM, et al. MRI assessment of basal ganglia iron deposition in Parkinson's disease. J Magn Reson Imaging 2008; 28: 1061–1067.
12. Youdim MB, Riederer P. The role of iron in senescence of dopaminergic neurons in Parkinson's disease. J Neural Transm Suppl 1993; 40:57–67.
13. Ryvlin P, Broussolle E, Piollet H, et al. Magnetic resonance imaging evidence of decreased putamenal iron content in idiopathic Parkinson's disease. Arch Neurol 1995; 52:583–588.
14. Antonini A, Leenders KL, Meier D, et al. T2 relaxation time in patients with Parkinson's disease. Neurology 1993; 43:697–700.
15. Griffiths PD, Dobson BR, Jones GR, et al. Iron in the basal ganglia in Parkinson's disease. Brain 1999; 122:667–673.
16. Menke RA, Scholz J, Miller KL, et al. MRI characteristics of the substantia nigra in Parkinson's disease: a combined quantitative T1 and DTI study. Neuroimage 2009; 47:435–441.
17. Drayer B, Burger P, Darwin R, et al. MRI of brain iron. AJR Am J Roentgenol 1986; 147:103–110.
18. Martin WR, Roberts TE, Ye FQ, et al. Increased basal ganglia iron in striatonigral degeneration: In vivo estimation with magnetic resonance. Can J Neurol Sci 1998; 25:44–47.
19. Kosta P, Argyropoulou MI, Markoula S, et al. MRI evaluation of the basal ganglia size and iron content in patients with Parkinson's disease. J Neurol 2006; 253:26–32.
20. Piccini P, Brooks DJ. New developments of brain imaging for Parkinson's disease and related disorders. Movement Disord 2006; 21:2035–2041.
21. Lee CS, Schulzer M, Mak E, et al. Patterns of asymmetry do not change over the course of idiopathic parkinsonism: implications for pathogenesis. Neurology 1995; 45:435–439.
22. Lewis MM, Smith AB, Styner M, et al. Asymmetrical lateral ventricular enlargement in Parkinson's disease. Eur J Neurol 2009; 16:475–481.
23. Huang X, Lee YZ, McKeown M, et al. Asymmetrical ventricular enlargement in Parkinson's disease. Movement Disord 2007; 22:1657–1660.
24. Harrison LCV, Raunio M, Holli KK, et al. MRI texture analysis in multiple sclerosis: toward a clinical analysis protocol. Acad Radiol 2010; 17: 696–707.
25. Mathias JM, Tofts PS, Losseff NA. Texture analysis of spinal cord pathology in multiple sclerosis. Magnet Reson Med 1999; 42:929–935.
26. Freeborough PA, Fox NC. MR image texture analysis applied to the diagnosis and tracking of Alzheimer's disease. IEEE Trans Med Imaging 1998; 17:475–478.
27. Bonilha L, Kobayashi E, Castellano G, et al. Texture analysis of hippocampal sclerosis. Epilepsia 2003; 44:1546–1550.
28. Zhang J, Tong L, Wang L, et al. Texture analysis of multiple sclerosis: a comparative study. Magn Reson Imaging 2008; 26:1160–1166.
29. Kjaer L, Ring P, Thomsen C, et al. Texture analysis in quantitative MR imaging tissue characterisation of normal brain and intracranial tumours at 1.5 T. Acta Radiol 1995; 36:127–135.
30. Herlidou-Meme S, Constans JM, Carsin B, et al. MRI texture analysis on texture test objects, normal brain and intracranial tumors. Magn Reson Imaging 2003; 21:989–993.
31. Mahmoud-Ghoneim D, Toussaint G, Constans J-M, et al. Three dimensional texture analysis in MRI: a preliminary evaluation in gliomas. Magn Reson Imaging 2003; 21:983–987.
32. Schad LR, Bluml S, Zuna I. MR tissue characterization of intracranial tumors by means of texture analysis. Magn Reson Imaging 1993; 11: 889–896.
33. Jirak D, Dezortova M, Taimr P, et al. Texture analysis of human liver. J Magn Reson Imaging 2002; 15:68–74.
34. Holli K, Lääperi AL, Harrison L, et al. Characterization of breast cancer types by texture analysis of magnetic resonance images. Acad Radiol 2010; 17:135–141.
35. Gibbs P, Turnbull LW. Textural analysis of contrast-enhanced MR images of the breast. Magnet Reson Med 2003; 50:92–98.
36. Harrison LC, Luukkaala T, Pertovaara H, et al. Non-hodgkin lymphoma response evaluation with MRI texture classification. J Exp Clin Cancer Res 2009; 28:87.
37. Haralick RM. Statistical and structural approaches to texture. Proc IEEE 1979; 67:786–804.
38. Kassner A, Thornhill RE. Texture analysis: a review of neurologic MR imaging applications. AJNR Am J Neuroradiol 2010; 31:809–816.
39. Hájek M, Dezortova M, Materka A, Lerski RA, eds. Texture Analysis for Magnetic Resonance Imaging. Prague, Czech Republic: Med4Publishing, 2006.
40. Collewet G, Strzelecki M, Mariette F. Influence of MRI acquisition protocols and image intensity normalization methods on texture classification. Magn Reson Imaging 2004; 22:81–91.
41. Loizou CP, Murray V, Pattichis MS, et al. Multiscale amplitude-modulation frequency-modulation (AMFM) texture analysis of multiple sclerosis in brain MRI images. IEEE Trans Inf Technol B 2011; 15:119–129.
42. Kassner A, Liu F, Thornhill RE, et al. Prediction of hemorrhagic transformation in acute ischemic stroke using texture analysis of postcontrast T1-weighted MR images. J Magn Reson Imaging 2009; 30: 933–941.
43. Holli KK, Waljas M, Harrison L, et al. Mild traumatic brain injury: Tissue texture analysis correlated to neuropsychological and DTI findings. Acad Radiol 2010; 17:1096–1102.
44. Holli KK, Harrison L, Dastidar P, et al. Texture analysis of MR images of patients with mild traumatic brain injury. BMC Med Imaging 2010; 10:8.
45. Peran P, Cherubini A, Assogna F, et al. Magnetic resonance imaging markers of Parkinson's disease nigrostriatal signature. Brain 2010; 133: 3423–3433.
46. Molnar GF, Pilliar A, Lozano AM, et al. Differences in neuronal firing rates in pallidal and cerebellar receiving areas of thalamus in patients with Parkinson's disease, essential tremor, and pain. J Neurophysiol 2005; 93: 3094–3101.
47. Chen H, Zhuang P, Miao S-H, et al. Neuronal firing in the ventrolateral thalamus of patients with Parkinson's disease differs from that with essential tremor. Chin Med J 2010; 123:695–701.
48. Mandir AS, Vaughan C. Pathophysiology of Parkinson's disease. Int Rev Psychiatr 2000; 12:270–280.
49. Fearnley JM, Lees AJ. Ageing and Parkinson's disease: substantia nigra regional selectivity. Brain 1991; 114:2283–2301.
50. Damier P, Hirsch EC, Agid Y, et al. The substantia nigra of the human brain: II. Patterns of loss of dopamine-containing neurons in Parkinson's disease. Brain 1999; 122:1437–1448.

Acta Radiologica
2015, Vol. 56(1) 97–104

DOI: 10.1177/0284185113519775
acr.sagepub.com

MR image texture in Parkinson's disease: a longitudinal study

Minna Sikiö[1,2], Kirsi K Holli-Helenius[1], Lara CV Harrison[2,3], Pertti Ryymin[1], Hanna Ruottinen[4,5], Tiia Saunamäki[5], Hannu J Eskola[1,2], Irina Elovaara[4,5] and Prasun Dastidar[1,4]

Abstract

Background: Few of the structural changes caused by Parkinson's disease (PD) are visible in magnetic resonance imaging (MRI) with visual inspection but there is a need for a method capable of observing the changes beyond the human eye. Texture analysis offers a technique that enables the quantification of the image gray-level patterns.

Purpose: To investigate the value of quantitative image texture analysis method in diagnosis and follow-up of PD patients.

Material and Methods: Twenty-six PD patients underwent MRI at baseline and after 2 years of follow-up. Four co-occurrence matrix-based texture parameters, describing the image homogeneity and complexity, were calculated within clinically interesting areas of the brain. In addition, correlations with clinical characteristics (Unified Parkinson's Disease Ranking Scales I–III and Mini-Mental State Examination score) along with a comparison to healthy controls were evaluated.

Results: Patients at baseline and healthy volunteers differed in their brain MR image textures mostly in the areas of substantia nigra pars compacta, dentate nucleus, and basilar pons. During the 2-year follow-up of the patients, textural differences appeared mainly in thalamus and corona radiata. Texture parameters in all the above mentioned areas were also found to be significantly related to clinical scores describing the severity of PD.

Conclusion: Texture analysis offers a quantitative method for detecting structural changes in brain MR images. However, the protocol and repeatability of the method must be enhanced before possible clinical use.

Keywords

Parkinson's disease, magnetic resonance imaging (MRI), texture analysis, image analysis, follow-up

Date received: 16 July 2013; accepted: 16 December 2013

Introduction

Parkinson's disease (PD) is a degenerative disorder of the central nervous system. Pathophysiologically, PD is characterized by the loss of dopaminergic neurons in the basal ganglia in which the most seriously affected brain area is the substantia nigra (SN) pars compacta (1). Changes in brain pathology caused by PD have also been reported in areas of thalami (2,3), caudate nucleus (4), putamen, and globus pallidus (4–9).

The identification of the midbrain dopaminergic regions is essential also when evaluating the structural changes associated with PD (10). Magnetic resonance imaging (MRI) has revealed narrowing in SN pars compacta (11,12), progressive ventricular enlargement

[1]Department of Radiology, Medical Imaging Center and Hospital Pharmacy, Tampere University Hospital, Tampere, Finland
[2]Department of Electronics and Communications Engineering, Tampere University of Technology, Tampere, Finland
[3]Department of Anaesthesia, Tampere University Hospital, Tampere, Finland
[4]Tampere Medical School, University of Tampere, Tampere, Finland
[5]Department of Neurology and Rehabilitation, Tampere University Hospital, Tampere, Finland

Corresponding author:
Minna Sikiö, Department of Radiology, Medical Imaging Center and Hospital Pharmacy, Tampere University Hospital, Teiskontie 35, PO Box 2000, FIN-33521, Tampere, Finland.
Email: minna.sikio@tut.fi

(13,14), and shape changes in the thalami (15). In a longitudinal MRI study, voxel-based morphometry analysis revealed a significant loss in gray matter volume during 2 years of follow-up (16). However, during a 1.4-year follow-up, the morphology method showed no significant progression of brain atrophy in PD patients (17).

Few of the structural changes are visible in MR images with visual inspection. Diffusion-weighted and heavily T2-weighted (T2W) MRI have produced promising results in revealing brain structure changes (18) but there is also need for a method capable of observing the invisible changes for the human eye. In addition to morphometry and shape analysis, texture analysis (TA) may be applied. TA refers to mathematical methods that describe the gray-level dependence between the image pixels. Texture parameters are used to characterize the underlying structures of the observed tissues. The hypothesis of TA is that by studying the gray-level transitions in medical images, we are able to extract textural features that characterize the pathology or the disease process of interest. In earlier studies concerning brain MR image texture TA has been proved, for example, to characterize brain tumors (19) and to discriminate between active and non-active lesions of multiple sclerosis patients (20). The co-occurrence matrix method (21) has proved useful for several clinical study materials and performs well for small regions present also in this study.

In our previous study, increased amount of interhemispheric textural differences in MR images of PD patients compared to controls were detected (22). However, to the best of our knowledge, no studies concerning the longitudinal textural changes caused by PD exist. Thus, we applied co-occurrence matrix-based TA method to study the possible MR image texture changes in vulnerable brain structures during a 2-year follow-up and compared the patients to a group of healthy controls. In addition, we evaluated the correlations between co-occurrence based TA parameters and clinical scores including the Unified Parkinson's Disease Ranking Scales (UPRDS) I–III measuring the severity of PD and Mini-Mental State Examination (MMSE) score estimating the severity of cognitive impairment.

Material and Methods

Patients and controls

At baseline, 51 patients with two or more of the following symptoms were recruited for the study: resting tremor, bradykinesia or hypokinesia, muscle stiffness, or postural instability. The exclusion criteria were Alzheimer's disease or other dementia, cerebrovascular attack, several general illnesses such as cardiac, lung or gastrointestinal disease, liver or kidney malfunction, active malignant neoplasm, neurological or psychiatric disease, contraindications for MRI, alcohol or drug addiction, and gravidity. Among the patients with diagnosed PD, 26 patients (age range, 42–85 years; mean age, 68.1 ± 10.4 SD years; 13 men, 13 women) were selected for this longitudinal study (Table 1).

The control group consisted of 19 healthy volunteers (age range, 58–80 years; mean age, 65.0 years $\pm$ 6.1 SD years; 4 men, 15 women) with similar exclusion criteria to the patient group and was matched by years of education. All participants gave their written consent for the study that was conducted at Tampere University Hospital and approved by the Pirkanmaa Hospital District Ethics Committee.

Clinical examinations

Clinical assessment was performed to patients both at the baseline and follow-up (Table 1). The Unified Parkinson's Disease Rating Scales (UPDRS) I, II, and III were established: UPDRS-I evaluates the mentation, behavior, and mood; UPDRS-II is a self-evaluated measure of the activities of daily living; and UPDRS-III is a clinician-scored motor examination. The Mini-Mental State Examination (MMSE) was used to estimate the severity of cognitive impairment and exclude dementia and Alzheimer's disease.

MRI

Imaging was performed using a 3-T MRI device (Siemens Trio, A Tim System, Siemens Healthcare Sector, Erlangen, Germany) with a 12-channel head matrix coil following a clinical procedure. From the imaging protocol, the images from the T2W three-dimensional (3D) sampling perfection with application-optimized contrasts using different flip angle evolution (SPACE) series was used in this study (Table 2). Baseline and follow-up MRI was performed with a time delay of 25.0 ± 1.5 months in PD patients.

Image levels of interest were selected with a DICOM image viewer Osiris (Windows version 4.19, The Digital Imaging Unit of the Service for Medical Computing of the Radiology Department of the University Hospital of Geneva, Switzerland) (Fig. 1). The selection was performed on the basis of appropriate landmarks in brain structures.

Image analysis

Regions of interest (ROIs) were the following clinically interesting brain structures: dentate nucleus, basilar pons, SN pars compacta, red nucleus, globus pallidus,

Table 1. Patient characteristics.

		Baseline				Follow-up			
Age (years)	Sex	UPDRS-I	UPDRS-II	UPDRS-III	MMSE	UPDRS-I	UPDRS-II	UPDRS-III	MMSE
58	M	2	2	12	30	2	7	–	29
80	F	3	7	32	27	3	8	30	27
52	F	3	5	14	30	4	5	22	29
68	F	1	3	21	28	–	–	–	28
73	M	0	11	12	26	2	10	15	29
85	M	2	14	36	26	3	30	45	26
69	F	2	2	15	30	1	3	7	29
84	F	2	5	21	29	2	7	26	28
66	M	1	1	14	27	0	1	17	27
80	F	4	7	20	29	2	4	12	26
62	F	1	1	14	30	1	3	22	29
66	M	3	14	27	25	7	10	20	24
42	F	2	21	25	28	4	10	24	27
76	F	2	9	25	29	2	9	25	29
54	M	1	4	15	30	1	4	27	28
60	M	4	0	21	29	3	21	32	30
72	F	2	7	20	27	–	–	–	–
60	M	6	11	35	27	2	5	17	28
77	M	1	5	35	28	1	4	41	24
71	F	0	3	19	30	3	4	23	28
61	M	2	2	30	27	2	5	33	27
77	M	3	14	26	21	–	23	15	15
63	F	2	2	21	25	–	4	30	27
74	F	3	4	9	29	2	5	19	29
75	M	4	5	13	27	–	–	8	–
62	M	3	3	17	29	–	–	14	28

MMSE, Mini-Mental State Examination; UPDRS, Unified Parkinson's Disease Rating Scale.

Table 2. MR image sequences and acquisition parameters.

Sequence	TR (ms)	TE (ms)	TI (ms)	Slice/gap (mm/mm)	Matrix size (pixels)	FOV (mm)	Flip angle (°)
Axial T2W SPACE	3200	354	–	3.0/0	384 × 290	75	120
Axial T2W 3D FLAIR SPACE	6000	383	2100	3.0/0	256 × 194	75	120
Axial 3D SWI	27	20	–	1.5/0	256 × 128	75	15
Axial parametric T2*/(MapIt)	422	25.6	–	4.0/4.8	384 × 384	100	60
Axial MDDW EPI 20dir (b = 0, b = 1000)	5100	94	–	3.0/3.9	128 × 128	100	90
Axial T1W SE	600	6.8	–	4.0/5.2	320 × 245	90	90
Sagittal 3D T1W MPRAGE	1900	2.4	900	1.0/0	256 × 246	100	9

EPI, echo planar imaging; FLAIR, fluid attenuated inversion recovery; FOV, field of view; MDDW, multi-directional diffusion weighting; MPRAGE, magnetization prepared rapid gradient echo; SE, spin echo; SPACE, sampling perfection with application optimized contrast using different flip-angle evolution; SWI, susceptibility weighted imaging; T1W, T1-weighted; TE, echo time; TI, inversion time; TR, repetition time.

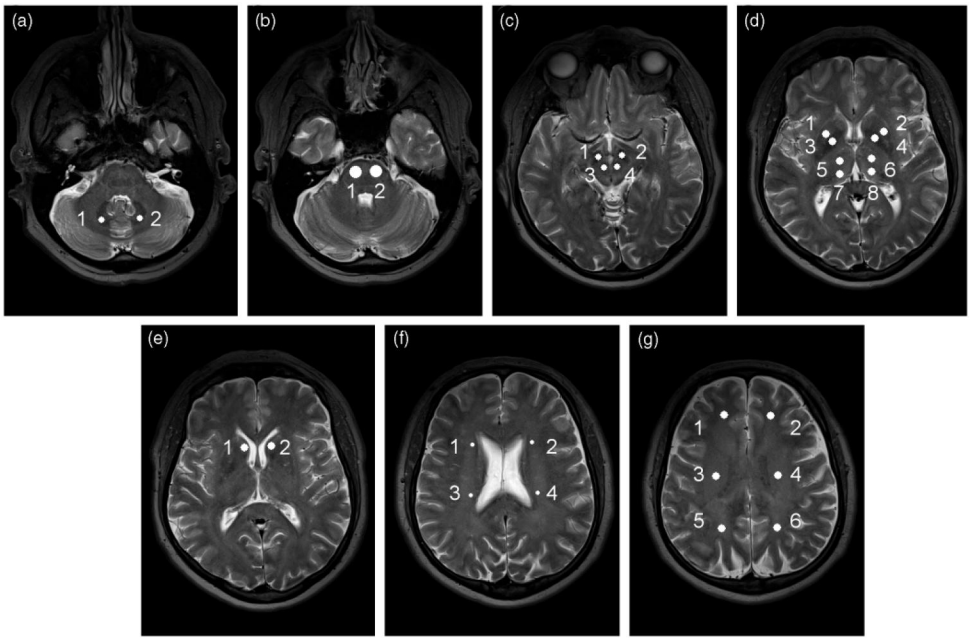

Fig. 1. Image levels. Visualization of MR image levels (a–g) and regions of interest. The regions of interest are marked with numbers and specified in Table 3.

putamen, anterior and posterior thalamus, caudate nucleus, anterior and posterior corona radiata, and anterior, medial, and posterior centrum semiovale (Fig. 1; Table 3). ROIs were manually placed on both hemispheres by an operator (MS) under the supervision of an experienced radiologist (PD).

TA was performed with MaZda software package (version 4.6) (23). MaZda enables calculation of almost 300 texture parameters but our goal was to select specific parameter setting of four parameters in advance the analyses. Based on earlier studies (24,25), we selected the co-occurrence method and two homogeneity (angular second moment and inverse difference moment) and two complexity (entropy and difference entropy) parameters derived from it. In MaZda, the parameters are calculated in four different directions (0°, 45°, 90°, and 135°) with pixel distances of one to five pixels. In our study, only the features calculated with pixel distance of one pixel were considered and the mean value of the four directional parameters was used in the further analyses. The analyses were performed in two-dimensional imaging because of the small pixel size compared to the 3.0-mm slice thickness.

MaZda offers three options to image normalization from which we chose the method that normalizes the image gray-levels between $\mu \pm 3\sigma$, where μ is the mean gray-level and σ is the standard deviation.

Statistical analysis

Statistical analysis of data was performed using SPSS (Windows version 20.0, SPSS Inc., Chicago, IL, USA). Due to the skewed distributions of the texture parameters, the comparisons were run with non-parametric tests. Mann-Whitney U test was used to evaluate whether there were statistically significant difference between the brain MR image textures of the baseline PD patients and those of the healthy controls. Differences in brain structure textures between the baseline and follow-up patient images were studied with Wilcoxon signed rank test. P values <0.05 were considered significant.

Correlations between changes in clinical scores and MR textures were evaluated with Pearson's correlation. Correlation coefficients >0.5 with P value <0.05 were considered significant.

Results

Textural differences

At baseline, most textural differences between patients and controls were found in areas of dentate nucleus and basilar pons (Table 4). There areas showed significant differences in MR image textures in both hemispheres

Table 3. MR image levels and regions of interest (ROI).

Level	ROI 1	ROI 2	ROI 3	ROI 4	ROI 5	ROI 6	ROI 7	ROI 8
A	Dentate nucleus dex (8 × 8)	Dentate nucleus sin (8 × 8)						
B	Basilar pons dex (15 × 15)	Basilar pons sin (15 × 15)						
C	SN pars compacta dex (8 × 8)	SN pars compacta sin (8 × 8)	Red nucleus dex (8 × 8)	Red nucleus sin (8 × 8)				
D	Putamen dex (10 × 10)	Putamen sin (10 × 10)	Globus pallidus dex (10 × 10)	Globus pallidus sin (10 × 10)	Thalamus ant dex (10 × 10)	Thalamus ant sin (10 × 10)	Thalamus post dex (10 × 10)	Thalamus post sin (10 × 10)
E	Caudate nucleus dex (10 × 10)	Caudate nucleus sin (10 × 10)						
F	Corona radiata ant dex (5 × 5)	Corona radiata ant sin (5 × 5)	Corona radiata post dex (5 × 5)	Corona radiata post sin (5 × 5)				
G	Centrum semiovale ant dex (10 × 10)	Centrum semiovale ant sin (10 × 10)	Centrum semiovale med dex (10 × 10)	Centrum semiovale med sin (10 × 10)	Centrum semiovale post dex (10 × 10)	Centrum semiovale post sin (10 × 10)		

The image levels and ROIs are specified in Fig. 1. ROI sizes in pixels are shown in brackets.
Ant, anterior; dex, dexter; med, medial; post, posterior; sin, sinister.

and with several co-occurrence matrix-based parameters. SN pars compacta differed significantly at the right hemisphere. Significant differences with single parameters were also found in the areas of posterior thalamus, putamen, caudate nucleus, and posterior corona radiata.

Significant differences in MR images of PD patients between baseline and follow-up appeared in anterior and posterior thalamus, putamen, caudate nucleus, and anterior corona radiata (Table 4). Of these above mentioned areas, posterior thalamus and putamen showed significant differences in both hemispheres.

Correlations between clinical scores and textures

Significant relations between the change in clinical scores and in texture parameters appeared during the 2-year period were found (Table 5). Change in the UPDRS-I score (evaluates the mentation, behavior, and mood) correlated with the change in entropy and difference entropy calculated from the area of posterior corona radiata; and with difference entropy calculated in the area of SN pars compacta. The shift in UPDRS-II score (the self-evaluation of the activities of daily living) within the 2 years correlated with texture parameters angular second moment, entropy, and difference entropy in the areas of putamen, dentate nucleus, and thalamus while UPDRS-III score (clinician-scored motor examination) correlated with angular second moment and entropy in the area of basilar pons. MMSE score showed significant correlation with the texture parameters in the areas of corona radiata and putamen. Inverse difference moment showed no correlations with the clinical scores and is, thus, not presented in the Table.

Discussion

In our study, we assessed the longitudinal differences in MR image textures of brain structures vulnerable to PD with a 2-year follow-up of diagnosed PD patients. We also evaluated the textural differences in brain MR images of PD patients and healthy controls.

First, textural differences between controls and PD patients at baseline were found in the areas of dentate nucleus, basilar pons, and SN pars compacta. These areas showed the lowest *P* values with several co-occurrence matrix-derived parameters. In earlier studies, especially the area of SN pars compacta has been associated with neuronal and volume loss (1,11,12,26,27) and iron deposition transitions (4–8,11,28) caused by PD. In addition, it has been proved that the T2-intensity of MR images of PD patients is lower in dentate nucleus and SN pars compacta compared to controls (29). Our present results

Table 4. Textural differences* when comparing controls to patients at baseline and patients at baseline to patients after a 2-year follow-up.

		Controls *vs.* patients at baseline				Patients at baseline *vs.* patients at follow-up			
	Structure	Ang sc mom	Inv dif mom	Ent	Dif ent	Ang sc mom	Inv dif mom	Ent	Dif ent
Right hemisphere	Dentate nucleus	0.176	0.080	0.126	**0.017**	1.000	0.970	0.909	0.395
	Basilar pons	**0.036**	0.859	**0.020**	**0.002**	0.439	0.568	0.469	0.638
	SN pars compacta	**0.004**	0.215	**0.003**	**0.006**	0.929	0.657	0.849	0.137
	Globus pallidus	0.097	0.116	0.076	0.258	0.534	0.091	0.469	0.238
	Thalamus ant	0.565	0.240	0.535	0.199	0.269	0.829	0.238	0.790
	Thalamus post	0.425	**0.044**	0.451	0.387	**0.020**	0.770	**0.012**	0.166
	Putamen	0.478	0.451	0.478	0.341	**0.012**	0.159	**0.015**	0.151
	Caudate nucleus	0.535	0.842	0.520	**0.039**	0.620	0.454	0.454	0.889
	Corona radiata ant	0.120	0.400	0.118	0.166	**0.011**	**0.012**	**0.018**	0.292
	Corona radiata post	0.261	0.894	0.201	0.912	0.328	0.439	0.303	0.790
Left hemisphere	Dentate nucleus	**0.006**	**0.013**	**0.009**	**0.025**	0.367	0.078	0.454	0.151
	Basilar pons	**0.005**	0.465	**0.003**	**0.005**	0.131	0.424	0.096	0.732
	SN pars compacta	0.173	0.982	0.176	0.132	0.361	0.603	0.316	0.144
	Globus pallidus	0.066	**0.018**	0.076	0.506	0.657	0.869	0.809	0.517
	Thalamus ant	0.419	0.550	0.425	0.790	**0.005**	0.316	**0.006**	**0.016**
	Thalamus post	0.947	0.610	0.825	0.690	0.058	**0.025**	**0.046**	**0.025**
	Putamen	0.069	**0.044**	0.097	0.580	0.485	0.751	0.269	**0.041**
	Caudate nucleus	0.492	0.506	0.535	0.520	0.970	0.517	0.657	**0.032**
	Corona radiata ant	0.277	0.658	0.258	0.842	0.316	0.238	0.275	0.354
	Corona radiata post	0.991	**0.049**	0.973	0.176	0.467	0.534	0.346	0.594

*Significant P values ($P < 0.05$) are given in boldface type.
Ang sc mom, angular second moment; ant, anterior; dif ent, difference entropy; ent, entropy; inv dif mom, inverse difference moment; post, posterior.

Table 5. Areas that showed significant correlation* between changes in clinical scores and local textures from baseline to follow-up after 2 years.

	Clinical score			
Texture parameter	UPDRS I	UPDRS II	UPDRS III	MMSE
Angular second moment	–	Putamen	Basilar pons	Corona radiata post
Entropy	Corona radiata post	Putamen	Basilar pons	Corona radiata post
Difference entropy	SN pars compacta	Dentate nucleus	–	Putamen
	Corona radiata post	Thalamus ant		
		Thalamus post		

*Relations with correlation coefficient >0.5 and P value <0.05.
Ant, anterior; post, posterior.

suggest that the pathophysiological and structural changes in these areas may also be characterized by alteration of the local texture.

Second, we studied the PD patients and compared the MR images at baseline to those obtained after a 2-year follow-up. Textural differences were detected in thalamus, putamen, caudate nucleus, and corona radiata. Previous studies have shown lowering in neuronal firing rates in the thalami and iron deposition transitions in putamen and caudate nucleus (6,8,9,30). Our findings in the midbrain area also refer to changes in this area caused by progressing PD. However, more TA studies are needed to ensure whether the textural differences suggest the direction of the iron deposition transformation.

Clinical scores have been correlated with different disease markers and factors in various studies. Significant relationship between UPDRS motor score measuring the severity of PD and different biomarkers have been shown (31,32). In a longitudinal morphometry study, the progression of brain atrophy was not correlated with the UPDRS-III score in any brain region (17). However, a volumetric study showed positive correlation between ventricular enlargement and worsening motor function assessed by UPDRS-III score (13). Our study showed correlation between changes in clinical scores and MR image textures calculated from brain areas vulnerable to PD.

The main drawback of this study is the lack of follow-up of the control group which was impossible because of schedule problems during the non-stop clinical work. The textural changes in aging human brain are an ongoing research area with, to our knowledge, no results yet reported. However, a brain volume loss study between healthy controls and PD patients showed no significant loss in the control group while the patients had significant reduction in both percentage and absolute annual brain volume (33). In addition, we found textural differences already at the baseline status of the patients and, hence, we assume the changes are due to PD. Also our results from the clinical score correlations suggest that the textural changes appeared during the 2-year follow-up are related to PD. All areas that showed significant textural differences between healthy controls and patients at baseline and after 2 years of follow-up were also found related to clinical scores measuring the severity of PD.

The strength of our study is the homogeneous patient material. The patients were carefully selected among all PD patients treated in Tampere University Hospital. Our study showed the existence of textural differences between PD patients and healthy controls but more studies with larger patient materials are needed to ensure the pathophysiological significance of the TA findings. The potential of TA in clinical use is to be an additional marker that gives information from clinical images and help the decision making in diagnosis. Therefore, future studies should also deal with the development of the TA practices. When considering TA as a clinical tool, the used manual image selection and ROI localization are too slow and cumbersome. Instead, automatic or semi-automatic analyses based on clear and appropriate anatomical landmarks and segmentation of the tissues of interest would be reasonable in respect to time-consuming and the need of special expertise. In order to become an assistive tool in diagnosis and follow-up of medical conditions, TA needs to be available and usable also for non-specialists in image analysis.

In conclusion, our study showed that there are textural differences in MR images of healthy controls and those of patients with PD. We also found differences in brain structure textures after a 2-year follow-up of PD patients and showed that they correlate with clinical scores measuring the severity of PD. Our study demonstrated that co-occurrence matrix-based TA method is able to detect such changes in brain structure textures that cannot be evaluated visually.

Funding

MS was supported by grants from the Research Fund of the City of Tampere, the Pirkanmaa Regional Fund of the Finnish Cultural Science Foundation, the Finnish Foundation for Technology Promotion, the Paulo Foundation, and the Ella and Georg Ehrnrooth Foundation.

References

1. Hornykiewicz O. Biochemical aspects of Parkinson's disease. Neurology 1998;51:S2–S9.
2. Henderson JM, Carpenter K, Cartwright H, et al. Loss of thalamic intralaminar nuclei in progressive supranuclear palsy and Parkinson's disease: Clinical and therapeutic implications. Brain 2000;123:1410–1421.
3. Bacci JJ, Kachidian P, Kerkerian-Le Goff L, et al. Intralaminar thalamic nuclei lesions: Widespread impact on dopamine denervation-mediated cellular defects in the rat basal ganglia. J Neuropathol Exp Neurol 2004; 63:20–31.
4. Antonini A, Leenders KL, Meier D, et al. T2 relaxation time in patients with Parkinson's disease. Neurology 1993;43:697–700.
5. Martin WR, Wieler M, Gee M. Midbrain iron content in early Parkinson disease: A potential biomarker of disease status. Neurology 2008;70:1411–1417.
6. Ryvlin P, Broussolle E, Piollet H, et al. Magnetic resonance imaging evidence of decreased putamenal iron content in idiopathic Parkinson's disease. Arch Neurol 1995;52:583–588.
7. Griffiths PD, Dobson BR, Jones GR, et al. Iron in the basal ganglia in Parkinson's disease. Brain 1999; 122:667–673.
8. Martin WR, Roberts TE, Ye FQ, et al. Increased basal ganglia iron in striatonigral degeneration: In vivo estimation with magnetic resonance. Can J Neurol Sci 1998; 25:44–47.
9. Kosta P, Argyropoulou MI, Markoula S, et al. MRI evaluation of the basal ganglia size and iron content in patients with Parkinson's disease. J Neurol 2006; 253:26–32.
10. Eapen M, Zald DH, Gatenby JC, et al. Using high-resolution MR imaging at 7T to evaluate the anatomy of the midbrain dopaminergic system. Am J Neuroradiol 2011; 32:688–694.
11. Graham JM, Paley MNJ, Grünewald RA, et al. Brain iron deposition in Parkinson's disease imaged using the PRIME magnetic resonance sequence. Brain 2000; 123:2423–2431.

12. Menke RA, Scholz J, Miller KL, et al. MRI characteristics of the substantia nigra in Parkinson's disease: A combined quantitative T1 and DTI study. Neuroimage 2009;47:435–441.
13. Lewis MM, Smith AB, Styner M, et al. Asymmetrical lateral ventricular enlargement in Parkinson's disease. Eur J Neurol 2009;16:475–481.
14. Camicioli R, Sabino J, Gee M, et al. Ventricular dilatation and brain atrophy in patients with Parkinson's disease with incipient dementia. Mov Disord 2011; 26:1443–1450.
15. McKeown MJ, Uthama A, Abugharbieh R, et al. Shape (but not volume) changes in the thalami in Parkinson disease. BMC Neurol 2008;8:8.
16. Ramirez-Ruiz B, Marti MJ, Tolosa E, et al. Longitudinal evaluation of cerebral morphological changes in Parkinson's disease with and without dementia. J Neurol 2005;252:1345–1352.
17. Brenneis C, Egger K, Scherfler C, et al. Progression of brain atrophy in multiple system atrophy. A longitudinal VBM study. J Neurol 2007;254:191–196.
18. Piccini P, Brooks DJ. New developments of brain imaging for Parkinson's disease and related disorders. Mov Disord 2006;21:2035–2041.
19. Schad LR, Bluml S, Zuna I. MR tissue characterization of intracranial tumors by means of texture analysis. Magn Reson Imaging 1993;11:889–896.
20. Yu O, Mauss Y, Zollner G, et al. Distinct patterns of active and non-active plaques using texture analysis on brain NMR images in multiple sclerosis patients: Preliminary results. Magn Reson Imaging 1999; 17:1261–1267.
21. Haralick RM, Shanmugam K, Dinstein I. Textural features for image classification. IEEE Trans Syst, Man, Cybern 1973;3:610–621.
22. Sikiö M, Holli KK, Harrison LCV, et al. Parkinson's disease: Interhemispheric textural differences in MR images. Acad Radiol 2011;18:1217–1224.
23. Szczypinski PM, Strzelecki M, Materka A, et al. MaZda – A software package for image texture analysis. Comput Methods Programs Biomed 2009;94:66–76.
24. Kassner A, Thornhill RE. Texture analysis: A review of neurologic MR imaging applications. Am J Neuroradiol 2010;31:809–816.
25. Mathias JM, Tofts PS, Losseff NA. Texture analysis of spinal cord pathology in multiple sclerosis. Magn Reson Med 1999;42:929–935.
26. Obeso JA, Marin C, Rodriguez-Oroz C, et al. The basal ganglia in Parkinson's disease: Current concepts and unexplained observations. Ann Neurol 2008;64:S30–S46.
27. Ziegler DA, Wonderlick JS, Ashourian P, et al. Substantia nigra volume loss before basal forebrain degeneration in early Parkinson disease. JAMA Neurol 2013;70:241–247.
28. Dexter DT, Carayon A, Javoy-Agid F, et al. Alterations in the levels of iron, ferritin and other trace metals in Parkinson's disease and other neurodegenerative diseases affecting the basal ganglia. Brain 1991;114:1953–1975.
29. Atasoy HT, Nuyan O, Tunc T, et al. T2-weighted MRI in Parkinson's disease; substantia nigra pars compacta hypointensity correlates with the clinical scores. Neurol India 2004;52:332–337.
30. Chen H, Zhuang P, Miao SH, et al. Neuronal firing in the ventrolateral thalamus of patients with Parkinson's disease differs from that with essential tremor. Chin Med J 2010;123:695–701.
31. Seibyl JP, Marek KL, Quinlan D, et al. Decreased single-photon emission computed tomographic [123I]beta-CIT striatal uptake correlates with symptom severity in Parkinson's disease. Ann Neurol 1995;38:589–598.
32. Benamer HT, Patterson J, Wyper DJ, et al. Correlation of Parkinson's disease severity and duration with 123I-FP-CIT SPECT striatal uptake. Mov Disord 2000;15:692–698.
33. Hu MT, White SJ, Chaudhuri KR, et al. Correlating rates of cerebral atrophy in Parkinson's disease with measures of cognitive decline. J Neural Transm 2001;108:571–580.

Clin Physiol Funct Imaging (2014) **34**, pp370–376 doi: 10.1111/cpf.12107

Influence of exercise loading on magnetic resonance image texture of thigh soft tissues

Minna Sikiö[1,2], Lara C. V. Harrison[2,3], Riku Nikander[4,5,6], Pertti Ryymin[1], Prasun Dastidar[1,7], Hannu J. Eskola[1,2] and Harri Sievänen[8]

[1]Department of Radiology, Medical Imaging Center and Hospital Pharmacy, Tampere University Hospital, [2]Department of Electronics and Communications Engineering, Tampere University of Technology, [3]Department of Anaesthesia, Tampere University Hospital Tampere, [4]Department of Health Sciences, University of Jyväskylä, Tampere, [5]GeroCenter Foundation for Aging Research and Development, [6]Jyväskylä Central Hospital, Jyväskylä, [7]Tampere Medical School, University of Tampere, and [8]Bone Research Group, UKK Intstitute for Health Promotion Research, Tampere, Finland

Summary

Adaptation to exercise training can affect bone marrow adiposity; muscle–fat distribution; and muscle volume, strength and architecture. The objective of this study was to identify exercise-load-associated differences in magnetic resonance image textures of thigh soft tissues between various athlete groups and non-athletes. Ninety female athletes representing five differently loading sport types (high impact, odd impact, high magnitude, repetitive low impact and repetitive non-impact), and 20 non-athletic clinically healthy female controls underwent magnetic resonance imaging. Five thigh muscles, subcutaneous fat and femoral bone marrow were analysed with co-occurrence matrix-based quantitative texture analysis at two anatomical levels of the dominant leg. Compared with the controls thigh muscle textures differed especially in high-impact and odd-impact exercise-loading groups. However, all sports appeared to modulate muscle textures to some extent. Fat tissue was found different among the low-impact group, and bone marrow was different in the high-impact group when compared to the controls. Exercise loading was associated with textural variation in magnetic resonance images of thigh soft tissues. Texture analysis proved a potential method for detecting apparent structural differences in the muscle, fat and bone marrow.

Correspondence

Minna Sikiö, Department of Radiology, Medical Imaging Center and Hospital Pharmacy, Tampere University Hospital, Teiskontie 35, PO Box 2000, FIN-33521 Tampere, Finland
E-mail: minna.sikio@tut.fi
Minna Sikiö and Lara Harrison with equal contribution to this work.

Accepted for publication

Received 18 June 2013;
accepted 30 October 2013

Key words

bone marrow; fat; femoral; impact; muscle; quantitative analysis; sport

Introduction

Adaptation to exercise training can lead to changes in bone marrow adiposity; muscle–fat distribution; and muscle volume, strength and architecture (Blazevich et al., 2003; Baar et al., 2006). These changes depend on the exercise type, especially the forces and load patterns, the given exercise induces. In response to exercise training, cross-sectional area and the strength production of actively involved muscles increase because the number and cross-sectional area of the individual muscle fibres also increase until the muscle strength is adjusted to cope with the forces and loads the given muscles and bone are subjected to (Nakai et al., 2008). Conversely, less-frequent and intense exercise training is associated with smaller muscle (Bousquet-Santos et al., 2006; Haddad & Adams, 2006; Browning et al., 2007).

Conventionally, the assessment of muscle adaptation to exercise has been evaluated with muscle volume. However, volume measurement does not reveal structural variation in muscle tissue or changes in intramuscular fat content. These changes can be observed with a quantitative image texture analysis (TA). TA is capable of detecting differences among tissues that are not always apparent to the human eye. Especially, magnetic resonance (MR) images contain such information that cannot be evaluated visually. Furthermore, MR imaging (MRI) is considered as the most suitable imaging modality for evaluating muscle anatomy, morphology and physiology because of its superior soft tissue contrast and spatial resolution.

Image texture is formed by repetitive elements called primitives. The aim of TA is to detect these primitives and subsequently characterize the texture type with texture features. In axial MR images, muscles can be seen as texture which is comprised by muscle bundles or their groups representing the primitives. As many skeletal muscles have a longitudinally oriented structure, thick MR image slices can be performed without problems concerning the partial volume effect. Furthermore, axial slices permit a good delineation of the adjacent muscles.

Textures have been utilized in both *ex vivo* and *in vivo* MR studies of skeletal muscles. Nakai *et al.* (2008) showed that walking exercise thickens and tightens the muscular fibre tissues. Mahmoud-Ghoneim *et al.* (2006) found TA a reproducible and non-destructive method for rat muscle examination during atrophy and regeneration. In their *ex vivo* study, they also found that MRI TA can discriminate genetics-related modifications in bovine meat (Mahmoud-Ghoneim *et al.*, 2005). In addition, their investigation of fat structure revealed that MRI texture of subcutaneous adipose tissue differs between men and women (Mahmoud-Ghoneim *et al.*, 2001). TA has also been proved to provide useful information contributing the diagnosis of skeletal muscle disease by Herlidou *et al.* (1999). TA of bone structure has been shown to give additional information to routinely measured bone density. Langenberger *et al.* (2003) were able to distinguish osteoporotic and non-osteoporotic subjects by means of TA.

In our previous studies of athletes, high-impact and odd-impact exercise loading were associated with thicker cortex around the femoral neck (Nikander *et al.*, 2009) and different trabecular bone texture compared with non-athletes (Harrison *et al.*, 2011). Depending of the sports, fat tissue thickness and volume can clearly vary between athlete groups, but it is not known whether this is reflected to texture of subcutaneous fat tissue texture. Also, it was recently shown that bone marrow density is modulated by exercise loading (Rantalainen *et al.*, 2013), but whether this would modulate marrow texture is not yet known. To the best of our knowledge, there exist no studies on influence of exercise load on MR image TA of femoral bone marrow and thigh muscle and fat tissues. Therefore, the aim of this study is to reveal exercise-load-associated differences in MR image textures of thigh soft tissues between various athlete groups and non-athletes.

Methods

This study employs previously collected MR image data from a total of 110 female volunteers. Recently, we successfully applied TA to detect exercise-associated structural differences in trabecular bone (Harrison *et al.*, 2011), and here, we extend our investigation to thigh muscles and fat and femoral bone marrow. The study protocol was approved by the Tampere University Hospital District Ethics Committee, and all participants gave their written informed consent for the study.

The study group comprised 90 female athletes competing at the national or international level and 20 non-athletic clinically healthy female controls. The athletes were triple jumpers ($n = 9$), high jumpers ($n = 10$), soccer players ($n = 10$), squash players ($n = 8$), power lifters ($n = 17$), endurance runners ($n = 18$) and swimmers ($n = 18$). The athletes were recruited through national sports associations and local sport clubs, and the controls were mainly students of the local university of applied sciences.

According to our previous classification scheme (Nikander *et al.*, 2009), the sports were divided into the following five categories representing the exercise-load types: high impact (H-I), odd impact (O-I), high magnitude (H-M), repetitive, low impact (L-I), and repetitive, non-impact (N-I). The H-I group comprised the triple jumpers and high jumpers, the O-I group comprised the soccer and squash players, the H-M group comprised the power lifters, the L-I group comprised the endurance runners, and the N-I group comprised the swimmers.

Magnetic resonance image

Imaging was performed with a 1.5-T MRI system (Siemens Magnetom; Avanto; Siemens Healthcare Sector, Erlangen, Germany). The thigh region of the dominant side was imaged using a combination of two 6-channel body matrix coils and the spine matrix coil. Normalization filter was used to correct the coil sensitivity profile and in order to minimize inhomogeneities in the image intensity.

The imaging sequence used in this study was axial 3D T2*-weighted multi-echo data image combination (MEDIC) sequence. MEDIC is a heavily T2*-weighted spoiled gradient echo sequence with high signal-to-noise ratio. The sequence is based on multiple echoes, three in our case, that are combined into an image for less artefacts; the early echoes increase the SNR level, while later echoes boost the contrast. The acquisition parameters were repetition time 40 ms, echo time 17 ms, slice thickness 3·00 mm, pixel size 0·81 mm × 0·84 mm, matrix size 384 × 308, field of view 312 × 260 and flip angle 12°.

Tissues of interest

The analysed soft tissues comprised thigh muscles and subcutaneous fat and femoral bone marrow of the dominant leg. The muscles were major anterior compartment muscles (rectus femoris, vastus lateralis, and vastus intermedius) and medial compartment muscles (adductor longus and adductor magnus). These five thigh muscles are actively involved in different load-bearing exercises and movements. All analysed tissues could be clearly distinguished in the MEDIC images (Fig. 1).

Image selection

The tissues were analysed at two anatomical levels of thigh that were chosen according to anatomical landmarks related to the muscle attachments. The proximal level was the image slice just distal from trochanter minor, and the distal level was the image slice at the insertion of muscle gluteus maximus to femur (Fig. 1). At these levels, the tissues of interest were visually distinguishable from each other, and the muscles were imaged at their contractive cross-section, not at the site of insertions. The image selection was manually performed with Osiris (version 4.19; The Digital Imaging Unit of the Service for Medical Computing of the University Hospitals of Geneva, Switzerland).

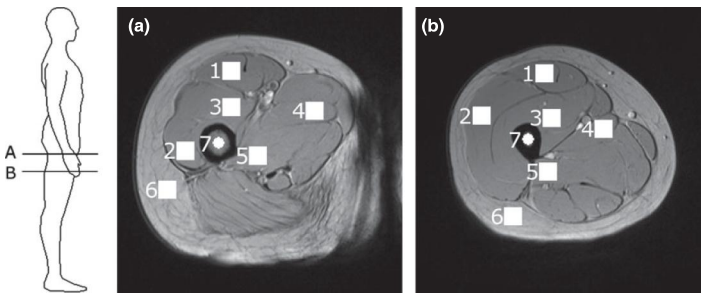

Figure 1 Image levels and regions of interests. Illustration of the proximal (a) and distal (b) image levels and their anatomical locations. Regions of interest are thigh muscles rectus femoris (1), vastus lateralis (2), vastus intermedius (3), adductor longus (4), adductor magnus (5), subcutaneous fat (6) and femoral bone marrow (7).

Texture analysis

Image textures were analysed with MaZda software (version 4.6; Institute of Electronics, Technical University of Lodz, Lodz, Poland) (Szczypinski et al., 2009; Strzelecki et al., 2013). Regions of interest (ROI) were predefined squares of 15 × 15 pixels, which were placed on the central area of muscle cross-section to avoid partial volume effect on ROIs caused by contamination with the connective tissue around the muscle and visible fascicles. In addition, a similar ROI box was placed on subcutaneous fat tissue surrounding the thigh muscles, and a spherical ROI of size 15 × 15 pixels was set on the bone marrow inside the femur. The ROI locations are depicted in Fig. 1.

Four following co-occurrence parameters were automatically calculated for each ROI: angular second moment, inverse difference moment, entropy and difference entropy. The first two describe the image homogeneity, whereas the last two parameters are measures of the image complexity. All parameters were calculated in horizontal (0°), vertical (90°) and two diagonal (45° and 135°) directions with a pixel distance of one pixel. The direction dependency of the parameters was removed by calculating the mean value of the four directions.

In order to minimize the influence of contrast and brightness variation, the image intensities were normalized in the range $[\mu \pm 3\sigma]$ (μ is the mean and σ the standard deviation of the image grey level). This method has shown to provide the best classification results in the TA of MR images compared with other possible methods (Collewet et al., 2004).

Statistical analysis

Statistical analyses were run on SPSS (version 20.0; SPSS Inc., Chicago, IL, USA). Due to the non-normal distribution of the texture parameters, nonparametric tests were used. Both the group analyses of muscles, fat and bone marrow were performed using the Mann–Whitney test. When comparing the five athlete groups to the control group, P-values lower than 0·01 were considered statistically significant.

The robustness of the TA method was assessed by comparing the co-occurrence matrix-based TA results between corresponding ROIs from two consecutive slices from both levels. For this analysis, groups were combined and the study population was analyzed as a whole. The statistics were performed with Mann-Whitney test and P-values under 0.05 were considered significant.

Results

In the robustness analysis, no significant differences in the texture parameters of any tissue were found (data not shown).

Muscles

The five thigh muscles were compared by means of co-occurrence matrix-based TA between the five different athlete groups and controls. The between-group differences based on Mann–Whitney tests are shown in Table 1. Figure 2 shows the distribution of texture parameter difference entropy in vastus lateralis muscle at the proximal level and rectus femoris muscle at the distal level.

When comparing the athlete groups to the controls at the proximal level, differences in muscle textures were mostly found in the H-I, O-I and N-I groups. All these groups showed significant textural difference in vastus lateralis muscle. The O-I group had different texture in adductor longus muscle compared with the control group. Single significant differences were also found in the H-I group in vastus intermedius, adductor longus and adductor magnus muscles; and in the L-I group in adductor magnus compared with the controls. At the distal level, different texture was especially found in rectus femoris muscle in the H-I, O-I, H-M and L-I. In addition, some sporadic differences were found between the H-I group and controls in vastus intermedius and adductor magnus and between the L-I group and controls in vastus intermedius.

Subcutaneous fat

Fat tissue texture results between the five athlete groups and control group are shown in Table 2, and the distribution of difference entropy is presented in Fig. 2. When compared to the controls. only the L-I group showed significant difference in fat texture with all the four parameters.

Table 1 Textural differences* in five selected thigh muscles between five different athlete groups and control group.

		Proximal level				Distal level			
Groups	**Muscle**	**Ang sc mom**	**Inv dif mom**	**Ent**	**Dif ent**	**Ang sc mom**	**Inv dif mom**	**Ent**	**Dif ent**
H-I versus REF	Rectus femoris	0·177	0·025	0·152	0·399	**0·002**	**0·001**	**0·002**	**0·004**
	Vastus intermedius	0·715	**0·009**	0·694	0·555	0·103	**0·009**	0·087	0·593
	Adductor longus	0·249	**0·005**	0·177	0·092	0·844	0·018	0·888	0·555
	Adductor magnus	0·033	**0·001**	0·018	0·072	0·574	**0·001**	0·500	0·026
	Vastus lateralis	**0·008**	**<0·001**	0·013	**0·001**	0·249	0·011	0·216	0·384
O-I versus REF	Rectus femoris	0·129	0·177	0·144	0·673	**0·001**	**0·002**	**0·001**	**0·003**
	Vastus intermedius	0·757	0·822	0·500	0·800	0·038	0·053	0·049	0·633
	Adductor longus	**0·008**	0·021	**0·003**	**0·004**	0·238	0·092	0·249	0·015
	Adductor magnus	0·026	0·779	0·021	0·196	0·072	0·012	0·053	0·043
	Vastus lateralis	**0·001**	0·025	**0·001**	**0·002**	0·933	0·555	0·866	0·354
H-M versus REF	Rectus femoris	0·300	0·273	0·266	0·235	**0·004**	**0·010**	**0·003**	0·016
	Vastus intermedius	0·446	0·503	0·503	0·879	0·017	0·015	0·015	0·055
	Adductor longus	0·604	0·563	0·411	0·542	0·113	0·072	0·088	0·113
	Adductor magnus	0·022	0·273	0·014	0·035	0·259	0·951	0·190	0·300
	Vastus lateralis	0·120	0·361	0·067	0·067	0·670	0·951	0·522	0·563
L-I versus REF	Rectus femoris	0·088	0·082	0·067	0·133	**0·001**	**0·002**	**0·001**	**0·006**
	Vastus intermedius	0·583	0·033	0·483	0·077	0·012	**<0·001**	0·011	0·019
	Adductor longus	0·152	0·021	0·094	**0·010**	0·855	0·542	0·879	0·286
	Adductor magnus	0·094	0·190	0·048	**0·004**	0·465	0·927	0·903	0·030
	Vastus lateralis	0·377	0·144	0·273	0·026	0·247	0·190	0·170	0·286
N-I versus REF	Rectus femoris	0·136	0·152	0·188	0·380	0·096	0·090	0·044	0·035
	Vastus intermedius	0·430	0·096	0·483	0·365	0·023	0·128	0·021	0·079
	Adductor longus	0·047	0·198	0·017	**0·004**	0·219	0·380	0·169	0·050
	Adductor magnus	0·114	0·231	0·096	0·090	0·977	0·413	0·861	0·430
	Vastus lateralis	**0·001**	0·047	**0·001**	**0·001**	0·380	0·748	0·365	0·380

Texture parameter abbreviations: ang sc mom, angular second moment; inv dif mom, inverse difference moment; ent, entropy; dif ent, difference entropy.
Exercise-loading group abbreviations: H-I, high impact; O-I, odd impact; H-M, high magnitude; L-I, low impact; N-I, non-impact.
*P-values were obtained with Mann–Whitney test. Statistically significant ($P<0·01$) results are given in boldface type.

Bone marrow

Bone marrow texture between the five athlete groups and control group shown in Table 3 revealed that the H-I group differed from the controls in marrow texture with two parameters at the proximal level. The distribution of difference entropy in bone marrow is shown in Fig. 2.

Discussion

In this study, exercise-loading-associated textural differences in MR images of five thigh muscles, subcutaneous fat tissue and bone marrow between athlete groups and non-athletes were examined by means of co-occurrence matrix-based TA. Textural differences were detected in all the studied soft tissues.

Compared with the non-athletic controls differences in muscle textures appeared especially in high-impact and odd-impact exercise-loading groups both at proximal and distal levels along the thigh. High-magnitude, low-impact and non-impact groups, in turn, showed less consistent differences compared with the controls. The fat tissue was found different among the low-impact group, and the bone marrow was different in the high-impact group when compared to the controls.

The textural differences detected in the muscles between the exercise-loading groups are in line with the fact that skeletal muscles adapt to long-term loading through changes in the muscle architecture (Caiozzo et al., 1981; Wilson et al., 1993; Abernethy & Jurimae, 1996). The high-impact-loading sports represent loading that produce maximal vertical forces at high rate, whereas odd-impact-loading sports include high acceleration and deceleration forces from unusual directions. In terms of muscle function, these load patterns require high activity and high rate of force production. Muscle adaptation to these forces typically leads to increase in cross-sectional area of muscle fibres (i.e. hypertrophy) and/or increase in the amount of muscle cells (i.e. hyperplasia). Moreover, the common factor in high- and odd-impact sports is the existence of short-term contacts to the ground, whereas in power-lifting or in other high-magnitude-loading sports the ground contacts comprise forces produced at relative low rate. Swimming, representing the non-impact loading sports, completely lacks these ground contacts during training. In an earlier study, Abe et al. (2000) showed significantly greater muscle thickness and fascicle length in vastus lateralis of 100-m sprinters than that of distance runners and controls. Although our study did not specifically involve sprinters, the loading of high-impact and odd-impact groups is close to that of short-distance runners and, using TA, we were

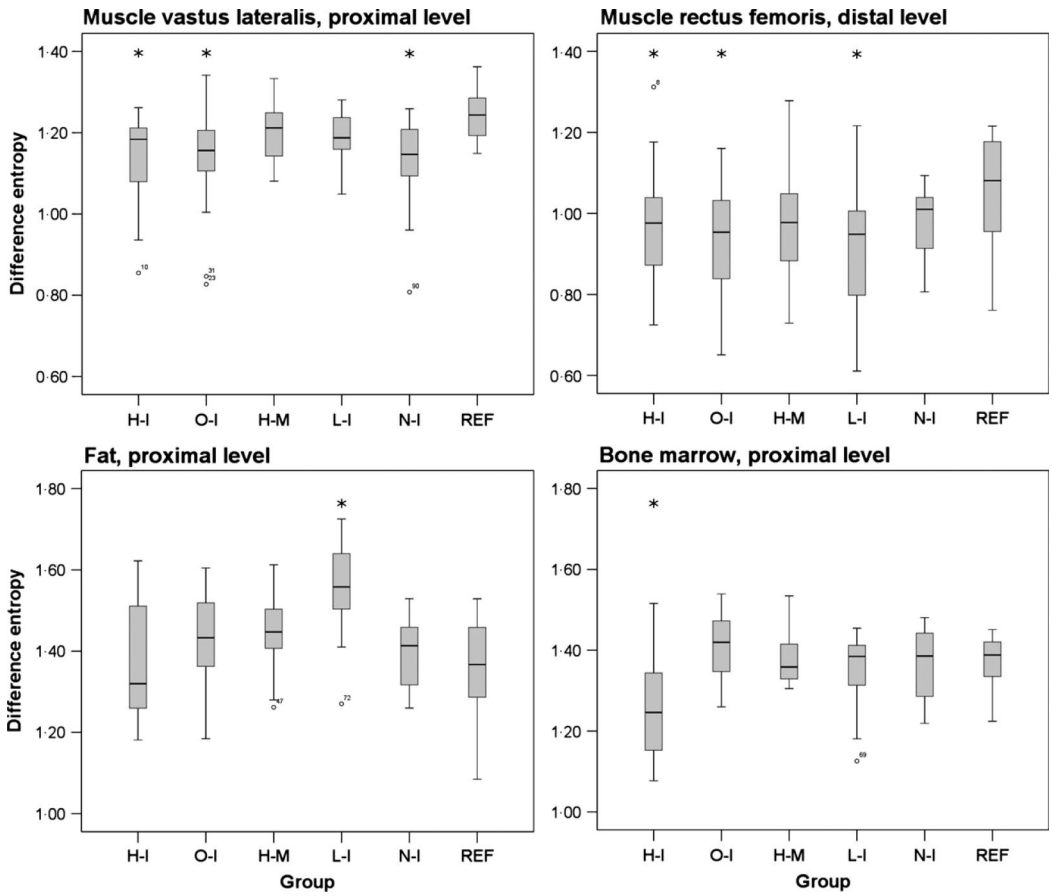

Figure 2 Box plots of difference entropy. Distributions of the co-occurrence matrix-based texture parameter difference entropy for vastus lateralis and rectus femoris muscles, subcutaneous fat and femoral bone marrow for the following athlete groups and non-athletic referents (REF): high impact (H-I), odd impact (O-I), high magnitude (H-M), low impact (L-I) and non-impact (N-I). The box-plot diagrams present the median values, 25th and 75th quartiles, and the whiskers show the 1·5 × interquartile range. The circles represent the outlier values (>1·5 × interquartile range). Groups marked with stars differ significantly from the control group.

Table 2 Textural differences* in fat tissue between five different athlete groups and control group.

	Proximal level				Distal level			
Groups	**Ang sc mom**	**Inv dif mom**	**Ent**	**Dif ent**	**Ang sc mom**	**Inv dif mom**	**Ent**	**Dif ent**
H-I versus REF	0·068	0·555	0·049	0·673	0·555	0·004	0·500	0·129
O-I versus REF	0·206	0·035	0·206	0·116	0·049	0·736	0·053	0·136
H-M versus REF	0·190	0·026	0·180	0·063	0·088	0·855	0·088	0·128
L-I versus REF	**<0·001**	**<0·001**	**<0·001**	**<0·001**	**<0·001**	**0·038**	**<0·001**	**<0·001**
N-I versus REF	0·293	0·108	0·306	0·483	0·136	0·102	0·114	0·447

Texture parameter abbreviations: ang sc mom, angular second moment; inv dif mom, inverse difference moment; ent, entropy; dif ent, difference entropy.

Exercise-loading group abbreviations: H-I, high impact; O-I, odd impact; H-M, high magnitude; L-I, low impact; N-I, non-impact.

*P-values were obtained with Mann–Whitney test. Statistically significant (P<0·01) results are given in boldface type.

Table 3 Textural differences* in bone marrow between five different athlete groups and control group.

	Proximal level				Distal level			
Groups	**Ang sc mom**	**Inv dif mom**	**Ent**	**Dif ent**	**Ang sc mom**	**Inv dif mom**	**Ent**	**Dif ent**
H-I versus REF	0·046	**0·006**	0·049	**0·004**	0·011	0·021	0·018	0·169
O-I versus REF	0·196	0·177	0·206	0·216	0·833	0·299	0·736	0·122
H-M versus REF	0·784	0·761	0·726	0·583	0·843	0·315	0·927	0·563
L-I versus REF	0·648	0·329	0·692	0·361	0·201	0·180	0·223	0·128
N-I versus REF	0·770	0·619	0·770	1·000	0·038	0·930	0·039	0·179

Texture parameter abbreviations: ang sc mom, angular second moment; inv dif mom, inverse difference moment; ent, entropy; dif ent, difference entropy.
Exercise-loading group abbreviations: H-I, high impact; O-I, odd impact; H-M, high magnitude; L-I, low impact; N-I, non-impact.
*P-values were obtained with Mann–Whitney test. Statistically significant ($P<0·01$) results are given in boldface type.

also able to detect differences in vastus lateralis when comparing these groups to the controls. Additional differences detected in the texture of adductor longus detected in the O-I group compared with the H-I group in adductor longus may be due to the powerful accelerations in lateral directions which is characteristic to ball games.

The pennation angle in leg muscles is shown greater in distance runners than sprinters and controls in a previous study (Abe et al., 2000). These changes may also modulate the muscle texture as our results showed significant differences between the L-I and control groups in four of the five studied thigh muscles. These textural differences may also be due to increased capillary and mitochondrial density originated from the muscle adaptation to endurance training. Contrary to expectations, few significant differences in muscle textures of the H-M group were detected when compared to the non-athletes. However, all the detected differences occurred in rectus femoris muscle, which is effectively stimulated in exercises that involve knee extension, such as squats in power-lifting. The adaptation to this loading may be detectable with TA.

Comparisons of the subcutaneous fat tissue among athletes and controls showed that the L-I group differed significantly from the non-athletes. These textural differences most likely refer to the size of the fat cells as they swell while storing body fat, but the amount of the cells remains quite unchanged. Endurance runners tend to have small body fat percentage, and fat cells are smaller than those of the other athletes and controls.

Bone marrow texture in the H-I group differed from that of the control group. These changes, detected by TA, may be attributable to increased vascularity caused by high-impact exercise loading. Similar results were obtained in a recent study of bone marrow density in tibia where the impact groups (H-I, O-I and L-I) showed higher bone marrow density suggesting lower marrow adiposity (Rantalainen et al., 2013). The reason we found the difference in bone marrow only in the H-I group might be the fact that the typical vertical impacts in O-I and L-I groups are not sufficiently high enough to result in detectable textural differences in the upper thigh region.

In our study, the femoral tissues were analysed with four co-occurrence matrix-derived parameters, of which angular second moment and inverse difference moment are measures of image homogeneity while entropy and difference entropy refer to the image complexity (Haralick et al., 1973; Haralick, 1979; Batchelor & Whelan, 2002). The co-occurrence method and the parameter setting were selected based on recent studies of human skeletal muscle, brain, spinal cord, and breast tissue and rat muscles (Herlidou et al., 1999; Mathias et al., 1999; Mahmoud-Ghoneim et al., 2006; Kassner et al., 2009; Holli et al., 2010a,b), and parameter properties. These parameters seemed suitable also for analysing muscle tissue, adipose tissue and bone marrow as the exercise-loading-associated differences were detected. Further, these parameters appeared robust as no parameter showed significant differences between the two adjacent slices in the large pooled data set.

Our TA analyses were performed in 2D. Even though 3D has been found preferable compared with 2D in discrimination of cerebral tissue, tumour, necrosis and oedema (Mahmoud-Ghoneim et al., 2003; Georgiadis et al., 2009), the advantages in muscle application are arguable because of the longitudinal structure of muscle fibres. In our study, the 2D approach was chosen because we were interested in the transverse texture of the striated muscle, and within this scope, the value of 3D analysis might have been trivial. However, muscles are 3D structures, and the ability of 3D TA to reveal additional information compared with 2D analysis should be evaluated in future studies.

In conclusion, exercise load was associated with textural variation in MR images of thigh soft tissues. High-impact (triple and high jump) and odd-impact (soccer and squash) loading sports were most consistently associated with textural differences in thigh muscles. However, all sports appeared to modulate muscle textures to some extent. In addition, low-impact loading sport (endurance running), involving large number of repetitive impacts, displayed a different fat tissue texture compared with non-athlete controls, and high-impact loading, involving very high vertical loads, was associated with different bone marrow texture.

Acknowledgments

MS was supported by grants from the Research Fund of the City of Tampere, the Pirkanmaa Regional Fund of the Finnish Cultural Science Foundation, the Finnish Foundation for Technology Promotion, the Paulo Foundation, and the Ella and Georg Ehrnrooth Foundation. RN is supported by the Fellow Researcher Grant (2011–2013) in Academy of Finland.

Conflict of interests

The authors have no conflict of interests.

References

Abe T, Kumagai K, Brechue WF. Fascicle length of leg muscles is greater in sprinters than distance runners. *Med Sci Sports Exerc* (2000); **32**: 1125–1129.

Abernethy PJ, Jurimae J. Cross-sectional and longitudinal uses of isoinertial, isometric, and isokinetic dynamometry. *Med Sci Sports Exerc* (1996); **28**: 1180–1187.

Baar K, Nader G, Bodine S. Resistance exercise, muscle loading/unloading and the control of muscle mass. *Essays Biochem* (2006); **42**: 61–74.

Batchelor BG, Whelan PF. Texture analysis. In: *Intelligent Vision Systems for Industry* [e-book] (2002), pp. 56–60. http://elm.eeng.dcu.ie/~whelanp/ivsi/IVSI.pdf.

Blazevich AJ, Gill ND, Bronks R, Newton RU. Training-specific muscle architecture adaptation after 5-wk training in athletes. *Med Sci Sports Exerc* (2003); **35**: 2013–2022.

Bousquet-Santos K, Vaisman M, Barreto ND, Cruz-Filho RA, Salvador BA, Frontera WR, Nobrega AC. Resistance training improves muscle function and body composition in patients with hyperthyroidism. *Arch Phys Med Rehabil* (2006); **87**: 1123–1130.

Browning RC, Modica JR, Kram R, Goswami A. The effects of adding mass to the legs on the energetics and biomechanics of walking. *Med Sci Sports Exerc* (2007); **39**: 515–525.

Caiozzo VJ, Perrine JJ, Edgerton VR. Training-induced alterations of the in vivo force-velocity relationship of human muscle. *J Appl Physio* (1981); **51**: 750–754.

Collewet G, Strzelecki M, Mariette F. Influence of MRI acquisition protocols and image intensity normalization methods on texture classification. *Magn Reson Imaging* (2004); **22**: 81–91.

Georgiadis P, Cavouras D, Kalatzis I, Glotsos D, Athanasiadis E, Kostopoulos S, Sifaki K, Malamas M, Nikiforidis G, Solomou E. Enhancing the discrimination accuracy between metastases, gliomas and meningiomas on brain MRI by volumetric textural features and ensemble pattern recognition methods. *Magn Reson Imaging* (2009); **27**: 120–130.

Haddad F, Adams GR. Aging-sensitive cellular and molecular mechanisms associated with skeletal muscle hypertrophy. *J Appl Physiol* (2006); **100**: 1188–1203.

Haralick RM. Statistical and structural approaches to texture. *Proc IEEE* (1979); **67**: 786–804.

Haralick RM, Shanmugam K, Dinstein I. Textural features for image classification. *IEEE Trans Syst Man Cybern* (1973); **3**: 610–621.

Harrison LC, Nikander R, Sikio M, Luukkaala T, Helminen MT, Ryymin P, Soimakallio S, Eskola HJ, Dastidar P, Sievanen H. MRI texture analysis of femoral neck: detection of exercise load-associated differences in trabecular bone. *J Magn Reson Imaging* (2011); **34**: 1359–1366.

Herlidou S, Rolland Y, Bansard JY, Le Rumeur E, de Certaines JD. Comparison of automated and visual texture analysis in MRI: characterization of normal and diseased skeletal muscle. *Magn Reson Imaging* (1999); **17**: 1393–1397.

Holli K, Laaperi AL, Harrison L, Luukkaala T, Toivonen T, Ryymin P, Dastidar P, Soimakallio S, Eskola H. Characterization of breast cancer types by texture analysis of magnetic resonance images. *Acad Radiol* (2010a); **17**: 135–141.

Holli KK, Harrison L, Dastidar P, Waljas M, Liimatainen S, Luukkaala T, Ohman J, Soimakallio S, Eskola H. Texture analysis of MR images of patients with mild traumatic brain injury. *BMC Med Imaging* (2010b); **10**: 8.

Kassner A, Liu F, Thornhill RE, Tomlinson G, Mikulis DJ. Prediction of hemorrhagic transformation in acute ischemic stroke using texture analysis of postcontrast T1-weighted MR images. *J Magn Reson Imaging* (2009); **30**: 933–941.

Langenberger H, Shimizu Y, Windischberger C, Grampp S, Berg A, Ferlitsch K, Moser E. Bone homogeneity factor: an advanced tool for the assessment of osteoporotic bone structure in high-resolution magnetic resonance images. *Invest Radiol* (2003); **38**: 467–472.

Mahmoud-Ghoneim D, de Certaines JD, Herlidou S, Rolland Y, Maniere A. Gender difference on magnetic resonance imaging texture analysis of human adipose tissue. *J Wom Imag* (2001); **3**: 105–107.

Mahmoud-Ghoneim D, Toussaint G, Constans JM, de Certaines JD. Three dimensional texture analysis in MRI: a preliminary evaluation in gliomas. *Magn Reson Imaging* (2003); **21**: 983–987.

Mahmoud-Ghoneim D, Bonny JM, Renou JP, de Certaines JD. Ex-vivo magnetic resonance image texture analysis can discriminate genotypic origin in bovine meat. *J Sci Food Agric* (2005); **85**: 629–632.

Mahmoud-Ghoneim D, Cherel Y, Lemaire L, de Certaines JD, Maniere A. Texture analysis of magnetic resonance images of rat muscles during atrophy and regeneration. *Magn Reson Imaging* (2006); **24**: 167–171.

Mathias JM, Tofts PS, Losseff NA. Texture analysis of spinal cord pathology in multiple sclerosis. *Magn Reson Med* (1999); **42**: 929–935.

Nakai R, Azuma T, Sudo M, Urayama S, Takizawa O, Tsutsumi S. MRI analysis of structural changes in skeletal muscles and surrounding tissues following long-term walking exercise with training equipment. *J Appl Physiol* (2008); **105**: 958–963.

Nikander R, Kannus P, Dastidar P, Hannula M, Harrison L, Cervinka T, Narra NG, Aktour R, Arola T, Eskola H, Soimakallio S, Heinonen A, Hyttinen J, Sievanen H. Targeted exercises against hip fragility. *Osteoporos Int* (2009); **20**: 1321–1328.

Rantalainen T, Nikander R, Heinonen A, Cervinka T, Sievanen H, Daly RM. Differential effects of exercise on tibial shaft marrow density in young female athletes. *J Clin Endocrinol Metab* (2013); **98**: 2037–2044.

Strzelecki M, Szczypinski P, Materka A, Klepaczko A. A software tool for automatic classification and segmentation of 2D/3D medical images. *Nucl Instrum Methods Phys Res A* (2013); **702**: 137–140.

Szczypinski PM, Strzelecki M, Materka A, Klepaczko A. MaZda – A software package for image texture analysis. *Comput Methods Programs Biomed* (2009); **94**: 66–76.

Wilson GJ, Newton RU, Murphy AJ, Humphries BJ. The optimal training load for the development of dynamic athletic performance. *Med Sci Sports Exerc* (1993); **25**: 1279–1286.

Clinical Investigative Study

MRI Texture Analysis and Diffusion Tensor Imaging in Chronic Right Hemisphere Ischemic Stroke

Minna Sikiö, MSc, Paula Kölhi, MSc, Pertti Ryymin, PhLic, Hannu J. Eskola, PhD, Prasun Dastidar, MD, PhD

From the Department of Radiology, Medical Imaging Center and Hospital Pharmacy, Tampere University Hospital, Tampere, Finland (MS, PK, PR, HJE, PD); Department of Electronics and Communications Engineering, Tampere University of Technology, Tampere, Finland (MS, PK, HJE); and Medical School, University of Tampere, Tampere, Finland (PD).

ABSTRACT

BACKGROUND AND PURPOSE

Diffusion tensor imaging (DTI) is shown to reveal changes caused by cerebral infarction. The aim of this study is to reveal those changes also in the conventional magnetic resonance (MR) images using a quantitative image analysis method, texture analysis (TA).

METHODS

Thirty patients who had suffered their first ever infarction located on the right hemisphere underwent DTI and conventional MRI studies in the chronic phase. DTI parameters fractional anisotropy and mean diffusivity, as well as four second-order texture parameters were calculated. Interhemispheric differences and correlations between DTI and TA parameters were evaluated.

RESULTS

Our DTI findings supported earlier studies as fractional anisotropy values were lowered and mean diffusivity values elevated in the lesion site, and ipsilateral cerebral peduncle, thalamus, and centrum semiovale compared to the unaffected side. Textural homogeneity parameters showed lower and complexity parameters higher values in the lesion site and ipsilateral centrum semiovale compared to the contralateral hemisphere. Correlation between the two methods was found in ipsilateral mesencephalon.

CONCLUSIONS

In addition to DTI method, TA could assist in revealing the changes caused by infarction, also outside the lesion site. Damaged areas were found more heterogeneous and random in texture compared to unaffected sites.

Keywords: Chronic infarction, magnetic resonance imaging, texture analysis, diffusion tensor imaging.

Acceptance: Received March 25, 2014, and in revised form July 30, 2014. Accepted for publication August 16, 2014.

Correspondence: Address correspondence to Minna Sikiö, Department of Radiology, Medical Imaging Center and Hospital Pharmacy, Tampere University Hospital, Teiskontie 35, P.O. Box 2000, FIN-33521, Tampere, Finland. E-mail: minna.sikio@tut.fi.

Funding sources: This study was financially supported by the Competitive State Research Financing of the Expert Responsibility area of Tampere University Hospital, grant 9R004. M.S. was supported by grants from the Research Fund of the City of Tampere, the Pirkanmaa Regional Fund of the Finnish Cultural Science Foundation, the Finnish Foundation for Technology Promotion, the Paulo Foundation, and the Ella and Georg Ehrnrooth Foundation. P.K. was supported by grants from the Research Fund of the City of Tampere and the Finnish Cultural Science Foundation.

Conflict of interest: We have declare that we have no conflict of interest.

J Neuroimaging 2015;25:614-619.
DOI: 10.1111/jon.12185

Background and Purpose

In the Western world, cerebral infarction, that is stroke, is a major cause of death and long-term disability. One-third of stroke patients die within a next year, one-third of patients remain permanently disabled, and one-third of patients make a reasonable recovery.[1–3]

Common physical defects after a right hemisphere ischemic stroke are left motor and sensory defects as well as various cognitive deficits, including left-sided neglect, anosognosia, visuoconstructive and visuospatial disorders, motor impersistence, dysprosody, disorders of body image and dressing, and visual memory deficits. To diagnose stroke, computed tomography (CT) imaging is widely used because CT scans are sensitive in detecting mass lesions and acute hemorrhage. However, infarction also causes tissue changes outside the visible infarction area. In hemispheric infarction, degenerative changes often take place in the corticospinal tracts deciphered as Wallerian degeneration (WD). WD is characterized by anterograde degeneration of axons due to injury of the proximal portion of the axon or its cell body.[4,5] WD can be detected with conventional magnetic resonance imaging (MRI) within 1 month after the infarction but diffusion tensor

imaging (DTI) may reveal it within the first 2 weeks after the infarction.[6]

DTI is an advanced MRI technique that is based on the water diffusion in a tissue. The apparent diffusion coefficient (ADC) describes the average diffusion of the media and varies depending on the tissue structure. ADC has been shown to decrease in acute ischemic stroke at lesion site. The decline is followed by pseudonormalization and, at the chronic stage, the values increase above normal levels.[7]

Conventional MR images contain, however, a large amount of such information that cannot be evaluated visually but could be detected with image analysis methods. Textures are image features that correspond to brightness values and locations of image pixels. Texture analysis (TA) is a quantitative image analysis method that has been shown to increase the level of diagnostic information extracted from several imaging modalities, such as MRI,[8] CT,[9] and ultrasound.[10] TA is a mathematical method that describes the grey level dependence between the image pixels and texture parameters are used to characterize the underlying structures of the observed tissues. Earlier studies have shown that it is possible to classify cerebral tissues with TA.[11,12] In acute ischemic stroke, TA has proved to detect significant differences between the infarcts that are vulnerable to hemorrhagic transformation and those that are not.[13]

Earlier, we studied chronic right-sided stroke patients with DTI and found that DTI is able to detect the changes caused by the infarction.[14] The aim of this novel study is to reveal those changes also in the conventional MR images using a quantitative image TA method. Interhemispheric differences of DTI and TA parameters are evaluated. We also evaluate the correlation between the DTI and TA parameters.

Methods

Study Population

In total, 1,458 stroke patients were examined and treated at Tampere University Hospital between July 2005 and April 2008. For the study, 30 patients (age range, 46-79; mean age, 65.5 ± 8.9 years; 24 men, 6 women) were selected. The selected patients had suffered their first ever infarction located on the right hemisphere and they had been capable of living independently before the infarction. Exclusion criteria were cerebral hemorrhage, traumatic brain injury, previous neurological or psychiatric disorder, substance abuse, lesions in the left hemisphere or previous lesions in the right hemisphere found in acute CT, remarkable brain atrophy in consideration of the patient's age, severe hearing or primary visual impairment, major decline in consciousness, left-handedness, native language other than Finnish, and age over 80 years. Seven of the patients had received thrombolytic therapy.

MRI

The patients underwent MRI studies in the chronic phase approximately one and a half year (mean 18.3 ± 5.5 months) after the infarction. MRI was performed in normal clinical practice with a 1.5-Tesla MRI whole-body scanner (Magnetom Avanto SQ, Siemens Medical Solutions, Erlangen, Germany) using a conventional 12-channel head matrix coil.

The conventional MRI protocol included sagittal T1-weighted (w) spin echo (SE) and 3-dimensional T2-w sampling perfection with application optimized contrast using different flip angle evolutions sequences and axial T2-w fluid-attenuated inversion recovery (FLAIR), T1-w SE, and T2-w gradient echo (T2*) sequences. The DTI was performed with single-shot diffusion-weighted echo-planar imaging (EPI) sequence where diffusion-sensitive gradients were applied along 12 gradient directions. Acquisitions were repeated 3 times and the average was used in the analyses. In this study, we used images from axial T2-w FLAIR, and diffusion-weighted EPI series. The typical acquisition parameters for the used sequences are presented in Table 1.

Image Analysis

The DTI data were analyzed with Siemens Syngo Neuro3D, version VE26A (Siemens, Erlangen, Germany). The mean diffusivity (MD) and fractional anisotropy (FA) values were calculated pixel-by-pixel from the diffusion-weighted images. The circular regions of interest (ROIs) were manually placed on axial slices in the cerebral peduncle, thalamus, knee of internal capsule, and centrum semiovale on both hemispheres. One ROI set was placed in the infarction area on the right and in corresponding area on the left hemisphere. The ROI sizes varied from 4 to 16 voxels depending on the target so that the corresponding areas in all images on both hemispheres had equal size ROIs. The ROIs were centered in the target areas avoiding border areas and neighboring tracts. Circular ROIs were selected as they were proved most repeatable in a recent DTI study.[15] The placement of the ROIs was based on brain anatomy regardless on the site of the lesion. Therefore, in centrum semiovale, a ROI of one patient partly overlapped with the infarction area. The ROI setting is specified in Figure 1.

The corresponding areas analyzed with DTI were also evaluated with TA (Fig 1). Patient images from the T2-w series were used because of the good separating capacity of various brain areas in this particular sequence. The ROIs were circular and ranged from 5 × 5 to 15 × 15 pixels.

TA was performed using the software package MaZda, version 4.6 (Technical University of Lodz, Institute of Electronics, Lodz, Poland).[16] Four second-order co-occurrence matrix-based parameters were used in the analyses: angular second moment, inverse difference moment, entropy, and difference entropy. The selected parameters describe the image homogeneity (angular second moment and inverse difference moment) and complexity or randomness (entropy and difference entropy). The features were calculated in horizontal (0°), vertical (90°), and two diagonal (45° and 135°) directions with a pixel distance of one pixel. The mean values of the four directions were used in the analyses.

The image intensities were normalized in the range ($\mu \pm 3\sigma$; μ refers to mean and σ to standard deviation of the grey level) to minimize the influence of contrast variation and brightness. This method was used because of its promising results in the TA of MRI images compared with other possible methods.[17]

Table 1. MR Image Sequences Used in the Study and the Acquisition Parameters

Sequence	TR (ms)	TE (ms)	TI (ms)	Slice/Gap (mm/mm)	Matrix Size (pixels)	FOV (mm)	Flip Angle (°)	*b*-Value (s/mm^2)
Axial T2-w FLAIR	8,500	100	2,500	5.0/1.5	256 × 256	230	150	–
Diffusion-w EPI	3,500	96	–	5.0/1.5	128 × 128	230	9	1000

EPI = echo-planar imaging; FLAIR = fluid attenuated inversion recovery; FOV = field of view; TE = echo time; TI = inversion time; TR = repetition time; w = weighted.

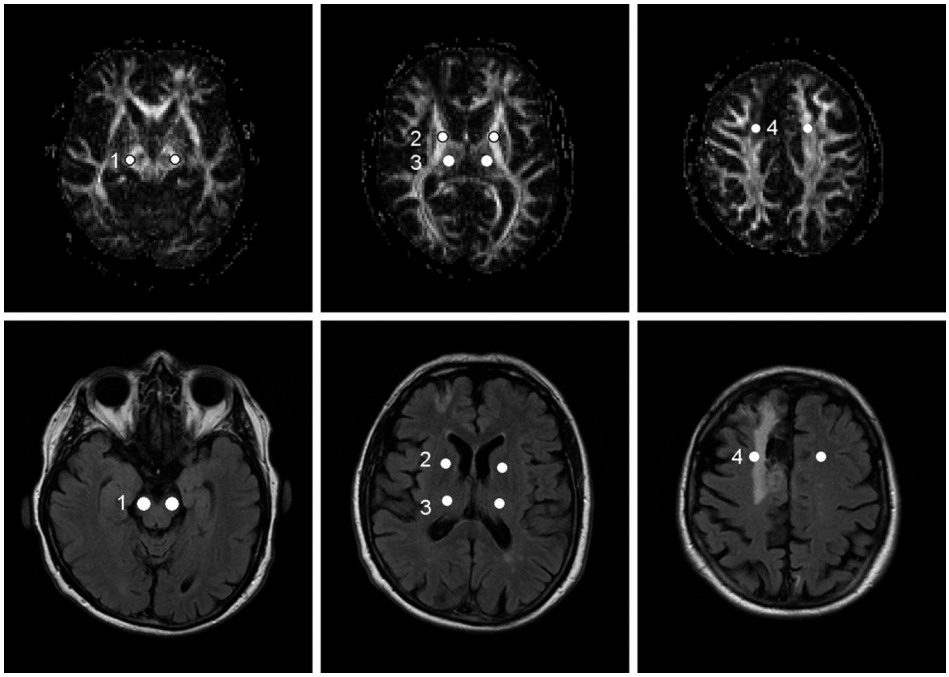

Fig 1. DTI (upper row) and MRI image levels and ROIs in cerebral peduncle (1), thalamus (2), internal capsule (3), and centrum semiovale (4).

Statistical Analysis

Differences between the infarct and unaffected hemisphere were studied with paired *t*-test and correlations were calculated with Pearson's R test. Statistical analyses were run using SPSS for Windows, version 20.0 (SPSS Inc., Chicago, IL, USA). All reported *P*-values were based on 2-tailed tests and *P*-values under .05 were considered statistically significant. Bonferroni correction was considered when concerning multiple comparisons.

Results

Interhemispheric Differences

Mean values and standard deviations for DTI parameters on infarct and unaffected sides are presented in Table 2. FA values were significantly lower in the infarction site compared to the reference area on the unaffected hemisphere. Lower ipsilateral FA values were also detected in cerebral peduncle. MD values were significantly higher in the infarct site, cerebral peduncle, and thalamus compared to the contralateral side.

Mean values and standard deviations for TA homogeneity parameters presented in Table 3 show that values of angular second moment were significantly lower in the infarct site. The other homogeneity parameter, inverse difference moment, showed no significant difference between the hemispheres.

Table 4 shows the mean values and standard deviations for TA complexity parameters. Both parameter values were elevated in infarct site compared to the reference area on left hemisphere. In addition, entropy was higher in ipsilateral centrum semiovale compared to the contralateral side.

Correlations

Correlation coefficients in Table 5 show that both DTI parameters, FA and MD, correlate with difference entropy calculated in mesencephalon of the infracted hemisphere. All other correlation coefficients were under .3.

Table 2. DTI Parameter Values and Differences* between the Hemispheres in Various Brain Areas

	FA			MD ($\times 10^{-3}$)		
	Infarct (Right) Side	Unaffected (Left) Side	*P*-Value	Infarct (Right) Side	Unaffected (Left) Side	*P*-Value
Infarct	.18 [.10]	.43 [.19]	**<.001**	1.83 [.57]	.81 [.14]	**<.001**
Cerebral peduncle	.75 [.08]	.79 [.06]	**.010**	.74 [.07]	.70 [.05]	**.007**
Internal capsule	.69 [.12]	.72 [.07]	.069	.72 [.07]	.70 [.05]	.035
Thalamus	.33 [.06]	.32 [.05]	.469	.87 [.19]	.77 [.06]	**.004**
Centrum semiovale	.56 [.09]	.60 [.09]	.035	.72 [.05]	.70 [.05]	.030

*P-values under .01 were considered significant and given in boldface.

Table 3. TA Homogeneity Parameter Values and Differences* between the Hemispheres in Various Brain Areas

	Angular Second Moment ($\times 10^3$)			Inverse Difference Moment ($\times 10^2$)		
	Infarct (Right) Side	Unaffected (Left) Side	*P*-Value	Infarct (Right) Side	Unaffected (Left) Side	*P*-Value
Infarct	15.53 [.83]	16.11 [.62]	**.003**	4.71 [1.64]	4.61 [1.46]	.794
Cerebral peduncle	2.16 [.11]	2.16 [.09]	.876	6.22 [1.26]	5.99 [.90]	.331
Internal capsule	3.60 [.16]	3.63 [.23]	.636	5.43 [1.11]	5.49 [1.20]	.768
Thalamus	3.77 [.19]	3.82 [.21]	.301	4.99 [.95]	4.98 [1.03]	.955
Centrum semiovale	3.83 [.22]	4.07 [.40]	.012	5.74 [1.07]	5.51 [1.25]	.503

*P-values under .01 were considered significant and given in boldface.

Table 4. TA Complexity Parameter Values and Differences* between the Hemispheres in Various Brain Areas

	Entropy			Difference Entropy		
	Infarct (Right) Side	Unaffected (Left) Side	*P*-Value	Infarct (Right) Side	Unaffected (Left) Side	*P*-Value
Infarct	1.82 [.01]	1.81 [.01]	**.001**	1.33 [.10]	.42 [.19]	**<.001**
Cerebral peduncle	2.69 [.02]	2.69 [.01]	.949	1.56 [.05]	1.58 [.05]	.197
Internal capsule	2.46 [.01]	2.46 [.02]	.556	1.56 [.04]	1.55 [.06]	.441
Thalamus	2.45 [.01]	2.44 [.02]	.277	1.53 [.04]	1.51 [.05]	.335
Centrum semiovale	2.44 [.02]	2.42 [.03]	**.010**	1.50 [.06]	1.46 [.07]	.063

*P-values under .01 were considered significant and given in boldface.

Table 5. Correlations* between DTI and TA Parameters in Ipsilateral Mesencephalon

	FA	MD
Angular second moment	.181	−.033
Inverse difference moment	−.401	.408
Entropy	−.177	.038
Difference entropy	***.535***	***−.531***

*Pearson correlations over .5 were considered significant and given in boldface.

Discussion

Our study concerned MR image analysis of chronic right hemisphere infarction patients. DTI analyses included evaluations of FA and MD values and conventional MR images were analyzed with TA by calculating homogeneity and complexity parameters. The aim of our study was to compare TA method to DTI analyses and evaluate the utility of TA in MR image analysis of stroke patients. DTI results of stroke patients have been published in previous studies but, to the best of our knowledge, no similar TA study has been reported.

Previous studies have shown that FA values are decreased and MD values are elevated in infarcted hemisphere compared to the contralateral side[7,14,18–21] and our DTI findings followed these logically. We found significant differences with both parameters in the lesion site and cerebral peduncle. In addition, MD differed in thalamus.

No reported findings of textural differences after infarction exist but a previous study showed that with TA it is possible to detect differences in infarcted brains of rats treated with different stroke therapy.[22] The use of TA was essential as the differences were not visible to the naked eye. Furthermore, it has been proven that physiological parameters, such as blood flow, may cause changes in texture parameters.[23]

We studied interhemispheric textural differences with four averaged second-order parameters: angular second moment, inverse difference moment, entropy, and difference entropy. The choice was based on earlier studies and assumption that infarction may change the tissue homogeneity. The features calculated in four different angles were averaged in order to eliminate the direction dependency because exact patient position in MRI could not be assured. Entropy parameters and angular second moment were proved to reveal differences between the hemispheres in mild traumatic brain injury patients.[24] In addition, averaged texture parameters have been shown to correlate with changes in ADC values.[22] We found angular

second moment values lower and both entropy parameter values higher in the lesion site compared to the reference area on the left hemisphere. Equal trend was found in centrum semiovale. These results indicate that the brain tissue texture on ipsilateral hemisphere is more heterogeneous and complex than on the contralateral side. This refers that damaged tissue might appear more coarse and random in texture compared to healthy tissue. Similar results were obtained in previous studies of mild brain injuries[24] and epilepsy.[25]

Altogether, both methods, DTI and TA, were capable detecting differences between infarcted and unaffected hemispheres also outside the infarction area. These increases and decreases in various parameters may refer to changes along the white matter tracts, that is presence of WD. However, the only correlation between the parameters was found in ipsilateral mesencephalon. The correlation of difference entropy with FA and MD was found significant while all other correlations coefficients were low. This indicates that DTI and TA parameters carry divergent information from the tissue properties.

It must be noted that our TA study concerned only four averaged co-occurrence matrix-based parameters. Hundreds of more textural features can be calculated to enhance the results. However, when developing the protocol of TA toward a simple and assistive clinical tool, some decisions have to be made beforehand to reduce the amount of data. Therefore, we selected four features and improved their robustness by averaging the different directions. Also, because of schedule problems our study contained no control group. Instead, we used the contralateral hemisphere as a point of comparison. ADC values have been shown to change also in the unaffected side at acute phase of stroke.[7] A study of pediatric strokes reported, however, no differences in the FA and MD values between the contralateral hemisphere and healthy control group at chronic stage.[26] In a TA study of mild traumatic brain injuries, interhemispheric textural differences among healthy controls were minimal.[24] Furthermore, our patient material consisted of only patients with first-ever right-sided infarction and the sample size was relatively small. Nevertheless, we believe the homogeneity of the patient group is also the strength of this study.

In conclusion, our study of right-sided stroke patients showed that DTI parameters revealed interhemispheric differences in the lesion site, cerebral peduncle, and thalamus, which was in line with earlier studies. Our novel TA results with homogeneity and entropy parameters supported the DTI findings while interhemispheric variation was found in the infarction site and centrum semiovale. Correlations of DTI and TA parameters showed that the two methods mainly reveal dissimilar information and could both assist in detecting tissue damages caused by stroke also outside the infarction area. Ipsilateral structures were found more heterogeneous and random in texture compared to the reference areas on the contralateral side.

The authors thank professor Jari Viik for statistical assistance.

References

1. Sudlow CLM, Warlow CP. Comparable studies of the incidence of stroke and its pathological types: results from an international collaboration. *Stroke* 1997;28:491-499.
2. Foerch C, Misselwitz B, Sitzer M, Berger K, et al. Difference in recognition of right and left hemispheric stroke. *Lancet* 2005;366:392-393.
3. Naess H, Waje-Andreassen U, Thomassen L, et al. High incidence of infarction in the left cerebral hemisphere among young adults. *J Stroke Cerebrovasc Dis* 2006;15:241-244.
4. Waller AV. Experiments on the section of the glossopharyngeal and hypoglossal nerves of the frog, and observations of the alterations produced thereby in the structure of their primitive fibres. *Philos Trans R Soc Lond* 1850;140:423-429.
5. Kuhn MJ, Mikulis DJ, Ayoub DM, et al. Wallerian degeneration after cerebral infarction: evaluation with sequential MR imaging. *Radiology* 1989;172:179-182.
6. Thomalla G, Glauche V, Koch MA, et al. Diffusion tensor imaging detects early Wallerian degeneration of the pyramidal tract after ischemic stroke. *Neuroimage* 2004;22:1767-1774.
7. Ahlhelm F, Schneider G, Backens M, et al. Time course of the apparent diffusion coefficient after cerebral infarction. *Eur Radiol* 2002;12:2322-2329.
8. Lerski RA, Straughan K, Schad LR, et al. MR image texture analysis–an approach to tissue characterization. *Magn Reson Imaging* 1993;11:873-887.
9. Ito M, Ohki M, Hayashi K, et al. Trabecular texture analysis of CT images in the relationship with spinal fracture. *Radiology* 1995;194:55-59.
10. Garra BS, Krasner BH, Horii SC, et al. Improving the distinction between benign and malignant breast lesions: the value of sonographic texture analysis. *Ultrason Imaging* 1993;15:267-285.
11. Kovalev VA, Kruggel F, Gertz H-J, et al. Three-dimensional texture analysis of MRI brain datasets. *IEEE Trans Med Imaging* 2001;20:424-433.
12. Herlidou-Meme S, Constans JM, Carsin B, et al. MRI texture analysis on texture test objects, normal brain and intracranial tumors. *Magn Reson Imaging* 2003;21:989-993.
13. Kassner A, Liu F, Thornhill RE, et al. Prediction of hemorrhagic transformation in acute ischemic stroke using texture analysis of postcontrast T1-weighted MR images. *J Magn Reson Imaging* 2009;30:933-941.
14. Jason E, Dastidar P, Kalliokoski A, et al. Diffusion tensor imaging of chronic right cerebral hemisphere infarctions. *J Neuroimaging* 2011;21(4):325-331.
15. Hakulinen U, Brander A, Ryymin P, et al. Repeatability and variation of region-of-interest methods using quantitative diffusion tensor MR imaging of the brain. *BMC Med Imaging* 2012;12:30.
16. Strzelecki M, Szczypinski P, Materka A, et al. A software tool for automatic classification and segmentation of 2D/3D medical images. *Nucl Instrum Meth A* 2013;702:137-140.
17. Collewet G, Strzelecki M, Mariette F. Influence of MRI acquisition protocols and image intensity normalization methods on texture classification. *Magn Reson Imaging* 2004;22:81-91.
18. Werring DJ, Toosy AT, Clark CA, et al. Diffusion tensor imaging can detect and quantify corticospinal tract degeneration after stroke. *J Neurol Neurosurg Psychiatr* 2000;69:269-272.
19. Chen Z, Ni P, Zhang J, et al. Evaluating ischemic stroke with diffusion tensor imaging. *Neurol Res* 2008;30:720-726.
20. Buffon F, Molko N, Herve D, et al. Longitudinal diffusion changes in cerebral hemispheres after MCA infarcts. *J Cereb Blood Flow Metab* 2005;25:641-650.

21. Herve D, Molko N, Pappata S, et al. Longitudinal thalamic diffusion changes after middle cerebral artery infarcts. *J Neurol Neurosurg Psychiatr* 2005;76:200-205.
22. Chen G, Strzelecki M, Pang Q, et al. Textures in magnetic resonance images of the ischemic rat brain treated with an anti-inflammatory agent. *Clin Imaging* 2010;34:7-13.
23. Mescam M, Bezy-Wendling J, Kretowski M, et al. Coupling texture analysis and physiological modeling for liver dynamic MRI interpretation. *Conf Proc IEEE Eng Med Biol Soc* 2007;2007:4223-4226.
24. Holli KK, Waljas M, Harrison L, et al. Mild traumatic brain injury: tissue texture analysis correlated to neuropsychological and DTI findings. *Acad Radiol* 2010;17:1096-1102.
25. Suoranta S, Holli-Helenius K, Koskenkorva P, et al. 3D texture analysis reveals imperceptible MRI textural alterations in the thalamus and putamen in progressive myolonic epilepsy type 1, EPM1. *PLoS One* 2013;8(7):e69905.
26. Khong PL, Zhou LJ, Ooi GC, et al. The evaluation of Wallerian degeneration in chronic paediatric middle cerebral artery infarction using diffusion tensor MR imaging. *Cerebrovasc Dis* 2004;18:240-247.

Tampereen teknillinen yliopisto
PL 527
33101 Tampere

Tampere University of Technology
P.O.B. 527
FI-33101 Tampere, Finland

ISBN 978-952-15-3816-2
ISSN 1459-2045